CHALMERS
UNIVERSITY OF TECHNOLOGY

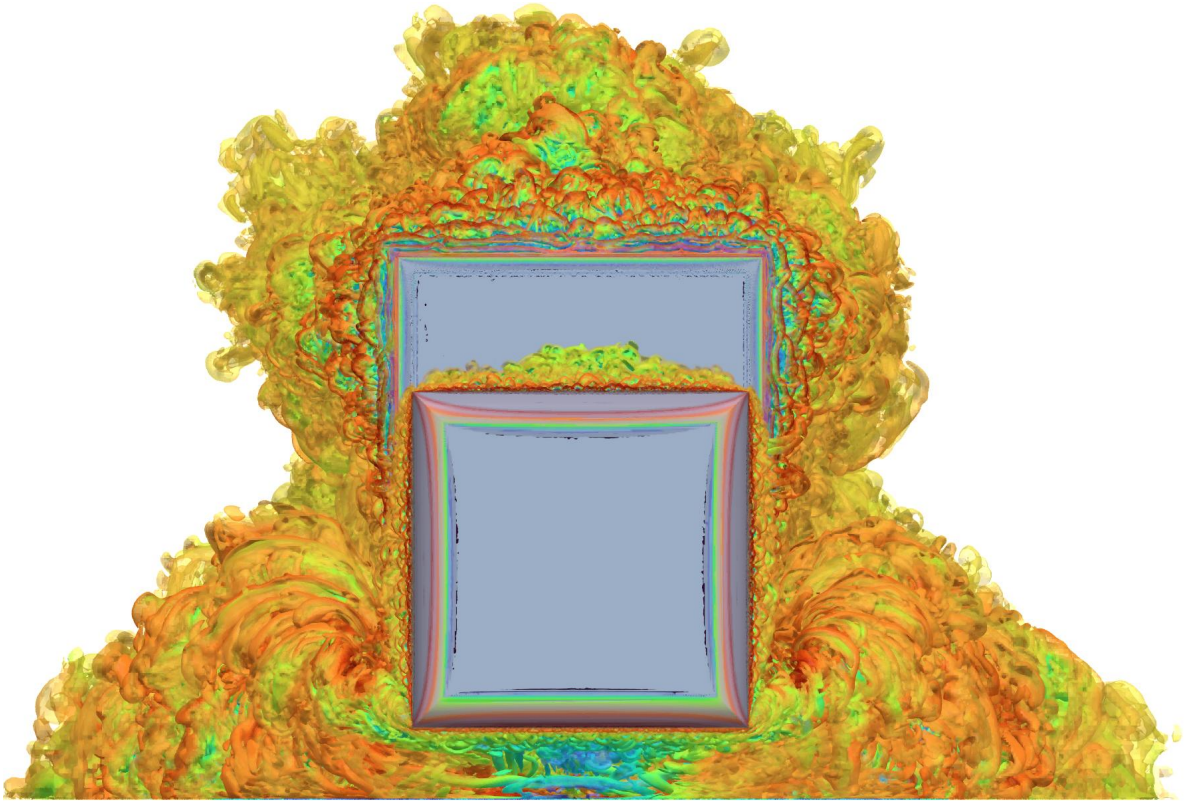

Turbulence and Near-Wall Modeling for Commercial Vehicle Aerodynamics

A Comparative Study of Scale Resolving Approaches

Master's thesis in Applied Mechanics

Alexander Karlsson & Berken Serbülent

DEPARTMENT OF MECHANICS AND MARITIME SCIENCES

CHALMERS UNIVERSITY OF TECHNOLOGY
Gothenburg, Sweden 2026
www.chalmers.se

Master's thesis in Applied Mechanics

Turbulence and Near-Wall Modeling for Commercial Vehicle Aerodynamics

A Comparative Study of Scale Resolving Approaches

Alexander Karlsson & Berken Serbülent

CHALMERS
UNIVERSITY OF TECHNOLOGY

Department of Mechanics and Maritime Sciences
Division of Vehicle Engineering and Autonomous Systems
Chalmers University of Technology
Gothenburg, Sweden 2026

Turbulence and Near-Wall Modeling for Commercial Vehicle Aerodynamics
Alexander Karlsson & Berken Serbülent

Supervisor: Anton Niklasson, Volvo Group
Examiner: Alexey Vdovin, Department of Mechanics and Maritime Sciences

Master's Thesis 2026
Department of Mechanics and Maritime Sciences
Division of Vehicle Engineering and Autonomous Systems
Chalmers University of Technology
SE-412 96 Gothenburg
Telephone +46 31 772 1000

Acknowledgements, dedications, and similar personal statements in this thesis reflect the authors' own views.

This thesis has made use of large language model (LLM) tools for text editing, paraphrasing, and language-style refinement. The physical ideas, methodology, analysis, and conclusions are the authors' own, with guidance and feedback from the supervisor.

Cover: Visualization of turbulent structures, $Q = 10^3\,\mathrm{s}^{-2}$, colored by velocity magnitude.

Typeset in LaTeX
Gothenburg, Sweden 2026

Turbulence and Near-Wall Modeling for Commercial Vehicle Aerodynamics
A Comparative Study of Scale Resolving Approaches
Alexander Karlsson & Berken Serbülent
Department of Mechanics and Maritime Sciences
Chalmers University of Technology

Abstract

This thesis presents a comparative study of turbulence and near-wall modeling for aerodynamic simulations of commercial vehicles. The work addresses a central challenge in industrial computational fluid dynamics, namely how to obtain reliable flow predictions without the prohibitive cost of high-fidelity scale-resolving methods. Two geometries were investigated: a simplified truck model and a detailed production-scale Volvo truck. The simplified case was used to evaluate wall-modeled LES, hybrid RANS–LES methods, Scale-Resolving Hybrid methods, and selected RANS formulations against a wall-resolved LES reference and experimental data. The production truck case was used to assess model behavior under full-scale wind-tunnel conditions. Additional simulations investigated model sensitivity to numerical choices such as time step, inner iterations, and prism-layer design.

Across both configurations, the turbulence model had a strong influence on predicted separation behavior, wake structure, and drag. For the simplified truck, DDES Elliptic Blending k-ε and wall-modeled LES showed the best overall agreement with the wall-resolved LES. For the full-scale truck, DDES Elliptic Blending k-ε gave the most accurate absolute drag predictions and the best agreement for yaw-weighted drag. However, DDES k-ω SST captured the relative drag differences between geometry variations more accurately. The sensitivity studies showed that the current numerical setup is generally robust. Timestep reduction and prism–layer variation showed only limited effects in aerodynamic drag. Furthermore, it was shown that 6 to 8 inner iterations generally resulted in convergence within each timestep. Overall, the results show that no single turbulence model is optimal for all purposes, and that model selection in industrial vehicle aerodynamics should be guided by the specific engineering objective.

Computational fluid dynamics, Turbulence modeling, Vehicle aerodynamics, Large-eddy simulation, Hybrid RANS-LES, Drag prediction, Near-wall treatment

Preface

This report presents the outcome of our master's thesis project carried out at Volvo Group in Göteborg, and examined by the Department of Mechanics and Maritime Sciences at Chalmers University of Technology. The work was performed in the Common Architecture and Shared Technology (CAST) and Platform Development department, within Vehicle Platform Analysis at Volvo Group, during the spring of 2026.

Acknowledgements

Our sincere thanks go to our supervisor, Anton Niklasson, for his guidance, insightful discussions, and continuous feedback throughout this project. His support, together with the patience of the Aero team in providing access to the Volvo cluster, was indispensable to this work. We are equally grateful to our examiner, Alexey Vdovin, for his valuable input and constructive feedback.

The colleagues in both platform analysis groups deserve special mention for their support, great company, and generous inclusion.

We would also like to thank everyone who has been part of our journey since the first day at Chalmers: friends made along the way, classmates and colleagues we have had the pleasure of sharing coffee breaks with during the thesis.

Above all, we are deeply grateful to our family and friends for their continuous patience, love, and support throughout our studies and during this final project.

Alexander Karlsson and Berken Serbülent, Gothenburg, June 2026

Nomenclature

Abbreviations

CFD	Computational Fluid Dynamics
CFL	Courant–Friedrichs–Lewy number
$\overline{\text{CFL}}$	Representative mean of CFL
DES	Detached Eddy Simulation
DDES	Delayed DES
DDES EB	DDES with Elliptic Blending k-ε closure
DDES k-ω	DDES with Menter k-ω SST closure
IDDES	Improved DDES with k-ω SST closure
HDV	Heavy-Duty Vehicle
LES	Large Eddy Simulation
RANS	Reynolds-Averaged Navier–Stokes
URANS	Unsteady RANS
SGS	Subgrid-Scale
SRH	Scale-Resolving Hybrid
SRS	Scale-Resolving Simulation
SST	Shear Stress Transport
STAR-CCM+	Siemens Simcenter STAR-CCM+ CFD solver
WALE	Wall-Adapting Local Eddy-viscosity (SGS model)
WM LES	Wall-Modeled LES
WR LES	Wall-Resolved LES
YWA	Yaw-Weighted Average

Definitions

1 drag count	$\Delta C_D = 0.001$

Subscripts and Superscripts

∞	Free-stream condition	
t	Turbulent quantity	
w	Wall quantity	
ref	Reference quantity	
sgs	Subgrid-scale quantity	
tot	Total quantity	

Variables

A	Frontal reference area	m^2
C_D	Drag coefficient	–
ΔC_D	Difference in drag coefficient	–
C_p	Pressure coefficient	–
$C_{p,\mathrm{tot}}$	Total pressure coefficient	–
C_f	Skin friction coefficient	–
F_D	Drag force	N
F_{Pressure}	Pressure drag force	N
F_{Shear}	Viscous shear drag force	N
k	Turbulent kinetic energy	$\mathrm{m}^2\,\mathrm{s}^{-2}$
L_{ref}	Reference length	m
p	Static pressure	Pa
p_T	Total pressure	Pa
Q	Q-criterion for vortex identification	s^{-2}
Re	Reynolds number	–
V_∞	Free-stream velocity	$\mathrm{m}\,\mathrm{s}^{-1}$
y^+	Non-dimensional wall distance	–
δ	Boundary-layer thickness	m
Δ	Grid filter width	m
Δt	Time step size	s
ε	Turbulent dissipation rate	$\mathrm{m}^2\,\mathrm{s}^{-3}$
μ_t	Turbulent dynamic eddy viscosity	$\mathrm{Pa}\,\mathrm{s}$
ν	Kinematic viscosity	$\mathrm{m}^2\,\mathrm{s}^{-1}$
τ_w	Wall shear stress	Pa
ω	Specific turbulent dissipation rate	s^{-1}

Contents

List of Figures

List of Tables

1
Introduction

This chapter establishes the industrial and environmental relevance of aerodynamic optimization for heavy-duty vehicles. It then discusses the role of numerical methods in addressing the associated simulation challenges. Building on this context, the purpose and research objectives of the study are presented, followed by a definition of its scope and limitations.

1.1 Background

Computational fluid dynamics (CFD) has become an indispensable tool in modern vehicle development, enabling the evaluation of aerodynamic performance early in the design process. Increasing demands for sustainable transport solutions and stricter emission regulations have further intensified the focus on CFD-based aerodynamic optimization. This is particularly relevant for electric vehicles, where aerodynamic efficiency plays a critical role in determining driving range.

1.1.1 Environmental and Economic Impact

Heavy-duty vehicles (HDVs) operate for long durations at highway speeds, where aerodynamic drag becomes the dominant source of resistance once velocities exceed approximately 80 km/h. HDVs are responsible for more than 25% of European greenhouse gas emissions and over 6% of global emissions [1]. In addition, fuel consumption accounts for approximately 30% of a truck's total life-cycle operating costs, with around 13.6% of energy losses attributed to aerodynamic drag [2]. Consequently, improving aerodynamic efficiency serves a dual purpose: it reduces environmental impact through lower emissions while simultaneously providing a competitive market advantage by lowering life-cycle costs, which is often the primary criterion when selecting commercial vehicles [3]. This makes aerodynamic optimization valuable both for sustainability goals and for manufacturers seeking to increase sales.

Accurate evaluation of aerodynamic performance for HDVs is therefore of high practical importance. However, improving accuracy remains challenging because of the complex flow separation and large-scale turbulent structures characteristic of the bluff-body aerodynamics associated with the vehicles. These flow complexities necessitate advanced numerical methods, which are discussed in the following subsection.

1.1.2 The Importance of Numerical Methods

A central challenge in numerical simulations of bluff-body aerodynamics is accurately predicting flow separation. Resolving the turbulence in near-wall regions with sufficient fidelity to capture separation is prohibitively expensive. As a result, practical simulations must leverage turbulence

modeling to balance computational costs against accuracy. Enhancing near-wall modeling credibility can significantly improve overall prediction accuracy, thereby supporting more effective aerodynamic development and ultimately contributing to reduced energy consumption and emissions.

Increasing demands on simulation accuracy have driven CFD in automotive aerodynamics from traditional Reynolds-Averaged Navier-Stokes (RANS) methods toward scale-resolving simulations (SRS). For bluff-body configurations such as the Ahmed body and realistic commercial vehicles, RANS models have shown limited ability to capture key flow features consistently [4]. Large-eddy simulation (LES) can achieve high accuracy when appropriate subgrid-scale models, such as WALE or dynamic Smagorinsky, are used, including correct prediction of laminar-to-turbulent transition. However, at industrially relevant Reynolds numbers, the computational cost of LES remains prohibitive.

Hybrid RANS-LES methods offer a practical compromise between accuracy and computational cost, and generally improve prediction of the overall flow field compared with pure RANS. However, their performance remains sensitive to mesh resolution, grid distribution, and shielding or transition behavior, which can lead to premature switching between RANS and LES regions or under-resolved turbulence. As a result, important flow structures may still be predicted inaccurately. [5]

1.2 Purpose

The aim of this master's thesis is to assess and compare the performance of hybrid RANS–LES and wall-modeled LES approaches for aerodynamic simulations of heavy-duty vehicles, with emphasis on the trade-off between accuracy and computational cost.

In order to accomplish this, the thesis aims to:

- Establish a wall-resolved LES simulation as a high-fidelity reference for evaluating lower-cost turbulence modeling approaches.
- Evaluate and compare the predictive accuracy and computational cost of DDES, IDDES, WM LES, and Scale-Resolving Hybrid (SRH) turbulence models against the LES reference and experimental data.
- Assess the sensitivity of drag prediction and near-wall flow behavior to prism-layer design choices, including layer count and wall-normal height.
- Assess the sensitivity of simulation accuracy and convergence to transient solver settings, specifically time-step size and the number of inner iterations per time step.
- Determine whether a single turbulence model and numerical setup can be recommended for industrial vehicle aerodynamic simulations.

1.3 Limitations

The thesis is confined to a workload of 30 ECTS, corresponding to approximately 1600 working hours distributed over two students. The scope of the work is therefore limited to a finite

set of simulation cases and parameter variations. The turbulence model evaluation is limited to the models available in STAR-CCM+. For WM LES and hybrid RANS-LES, only the implementations provided in STAR-CCM+ are considered. Alternative formulations reported in the literature, which may offer improved accuracy under certain conditions, are outside the scope of this study.

A key limitation of this study is the available computational resources. Because of its high computational cost and memory requirements, the LES simulation was performed on a mesh at the coarse end of the recommended range for wall-resolved LES, with a slightly larger time step than ideal. Further mesh refinement and time-step reduction were not feasible because of RAM and turnaround-time constraints, and full grid independence could therefore not be established. These constraints also made a complete grid-convergence study across all turbulence models, prism-layer strategies, and solver settings infeasible. Instead, mesh resolutions and near-wall treatments were chosen to reflect current industrial best practices and realistic simulation times. Consequently, the LES results should be regarded as a high-fidelity reference within computationally feasible limits, and any identified optimal setups should be regarded as industrially efficient solutions rather than universally optimal or grid-independent configurations.

Validation of the numerical results is limited to the available experimental and test data for the production truck provided by Volvo Trucks [6] and for the Allan body provided by J.W. Allan [7]. No new experimental measurements are conducted, and the availability and resolution of validation data restrict the range of flow quantities that can be assessed. Therefore, conclusions drawn from the comparison are case-specific to the studied geometries and operating conditions.

2

Theory

This chapter presents the theoretical background relevant for analyzing heavy vehicle aerodynamics using both classical fluid mechanics and computational methods. The discussion begins with the governing principles of fluid motion and the aerodynamic characteristics of truck-like bluff bodies. It then introduces the key concepts needed to interpret the flow field, including non-dimensional coefficients, boundary-layer behavior, flow separation, and vortical structures. The chapter concludes with an overview of CFD methodology and turbulence modeling approaches, which form the basis for the numerical analyses used in this work.

2.1 Fluid Mechanics

This section establishes the theoretical foundation for fluid behavior in external vehicle flows. It is divided into two main parts: the fundamental governing equations of fluid motion, and the specific aerodynamic principles relevant to heavy commercial vehicles, such as boundary layer behavior, flow separation, and vortex dynamics.

2.1.1 Governing Equations

The behavior of a fluid is governed by the conservation laws of mass, momentum, and energy. Under the assumptions of incompressibility, isothermal conditions, and constant viscosity, these reduce to the incompressible continuity equation (2.1) and the Navier–Stokes equation (2.2). For road vehicle aerodynamics the fluid is seen as incompressible due to the relatively low velocities around the body, which do not exceed $M << 0.27$.

$$\frac{\partial v_i}{\partial x_i} = 0 \tag{2.1}$$

$$\rho\frac{\partial v_i}{\partial t} + \rho\frac{\partial v_i v_j}{\partial x_j} = -\frac{\partial P}{\partial x_i} + \mu\frac{\partial^2 v_i}{\partial x_j \partial x_j} \tag{2.2}$$

2.1.2 Heavy Vehicle Aerodynamics

Road vehicles, especially trucks, can be generalized as bluff bodies located close to the ground. The aerodynamic characteristics of bluff bodies mean that trucks often exhibit early separation at leading edges and large wakes with poor pressure recovery. Truck drag is primarily pressure-dominated, with 85–90% of the drag caused by the wake [2]. This section introduces the

theoretical concepts needed to evaluate heavy vehicle aerodynamics and drag reduction strategies. Specifically, it covers non-dimensional coefficients, boundary layer behavior, flow separation, and vortex dynamics.

2.1.2.1 Heavy-Duty Truck Configurations and Aerodynamic Features

A classic truck can be divided into three main aerodynamic parts: chassis, cab, and trailer. Two main versions of trucks exist: the conventional configuration, where the engine is placed in front of the cab, which is predominantly used in North America and Australia, and the cab-over-engine configuration with a flat front, which is used in the rest of the world. Trucks can either be of tractor-trailer type or rigid body. The rigid body truck has the trailer mounted directly to the frame, while tractor-trailers have a tractor pulling a semi-trailer mounted on a turntable. [2]

Although considerable efforts have been devoted to aerodynamic development in modern trucks, they can generally still be characterized as bluff bodies. Consequently, particular focus is placed on the curvature of the front edges, as these features strongly influence the downstream flow development and the formation of the wake. Modern trucks are equipped with aerodynamic devices designed to reduce drag and improve overall flow behavior. The primary components include roof deflectors, side deflectors, and carefully shaped front-ends, as these regions govern how the mean flow is guided around the body.

The roof deflector is intended to smoothly direct the incoming flow over the leading edges of the trailer, thereby reducing flow separation at the sharp upper corners. The side deflectors are of particular importance under yawed inflow conditions, where they limit the amount of air entering the tractor-trailer gap and thereby reduce additional drag associated with cross-flow effects. Studies have shown that the optimized combination of roof deflectors and cab side extenders can yield total aerodynamic drag reductions of 10% to over 15%, depending heavily on the trailer gap size and yaw conditions [8]. An overview of these key aerodynamic features on a modern cab-over-engine design is illustrated in Figure 2.1.

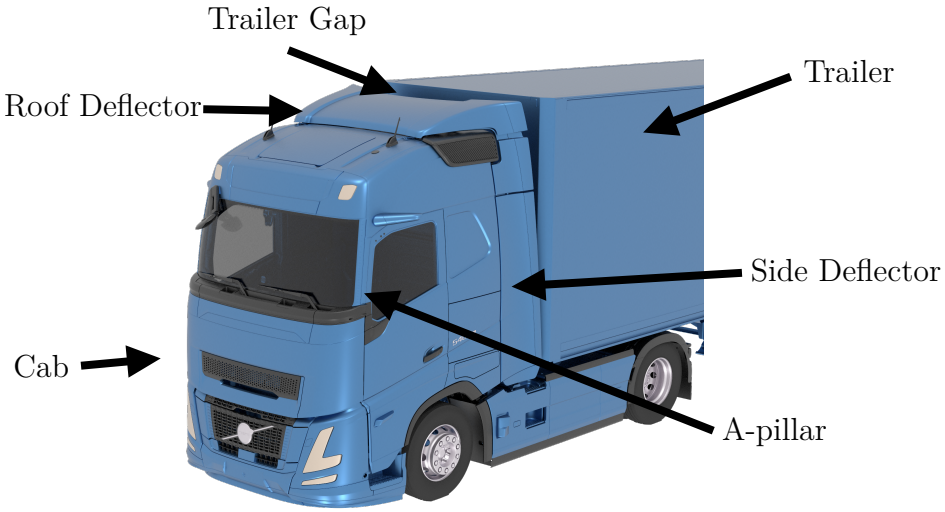

Figure 2.1: Overview of the Volvo FH Aero truck geometry. Key aerodynamic features are labeled, including the cab, trailer, tractor-trailer gap, A-pillars, and deflector systems.

2.1.2.2 Non-dimensional Coefficients

Non-dimensional coefficients are dimensionless quantities that characterize fluid-flow phenomena through comparisons between different forces. They provide a standardized way to compare flow behavior across different scales and operating conditions.

2.1.2.2.1 Reynolds Number

The Reynolds number is a dimensionless measure of the ratio of inertial to viscous forces in a fluid flow. Low Reynolds numbers typically indicate laminar flow, while at high numbers the flow tends to be turbulent. Heavy-duty trucks typically operate at moderately high Reynolds numbers, with characteristic values in the range of 10^6–10^7. The Reynolds number is defined as:

$$Re = \frac{\rho U_\infty L_{\text{ref}}}{\mu}, \tag{2.3}$$

where L_{ref} is a characteristic length scale, for truck aerodynamics commonly taken as the vehicle width or the square root of the frontal area. [9]

For bluff bodies such as trucks, a local Reynolds number is often more relevant than the global Reynolds number, as it governs flow separation and the development of smaller-scale turbulent fluctuations. Separation is often initiated at the A-pillar, and therefore the corner radius is an appropriate characteristic length scale for a local Reynolds number. This dimension better describes the local flow behavior around the front edges of the vehicle, where strong curvature effects influence boundary-layer development and separation. [2]

2.1.2.2.2 Aerodynamic Forces

Aerodynamic forces are forces exerted by the surrounding fluid on a submerged body. In general form, they can be expressed as

$$F_i = \frac{1}{2}\rho V_\infty^2 A C_i, \tag{2.4}$$

where i denotes the force direction, such as drag, lift, or side force. Here, ρ is the air density, V_∞ is the free-stream velocity, A is a reference area, typically the frontal projected area for road vehicles, and C_i is the corresponding non-dimensional force coefficient.

To improve aerodynamic efficiency, the primary objective is to reduce the drag force, which opposes the vehicle's direction of travel and is denoted by F_D. This force is commonly expressed in non-dimensional form through the drag coefficient C_D. The drag force can be decomposed into two parts, pressure drag and shear drag:

$$\mathbf{F}_D = \mathbf{F}_{\text{Pressure}} + \mathbf{F}_{\text{Shear}} \tag{2.5}$$

The pressure drag, $\mathbf{F}_{\text{Pressure}}$, is the net force component caused by pressure forces acting on the body's surface. It results from the pressure difference between the front and the rear and is defined as:

$$\mathbf{F}_{\text{Pressure}} = \iint_S (-p\,\mathbf{n} \cdot \mathbf{e}_x)\,\mathrm{d}A \tag{2.6}$$

Here, p is the surface static pressure, $\mathbf{n}$ is the outward unit normal, S is the body surface, and $\mathbf{e}_x$ is the free-stream direction. [10]

The shear drag force, $\mathbf{F}_{\text{Shear}}$, is the force component caused by tangential viscous forces along the body's surface, arising from the wall no-slip condition and velocity gradients in the boundary layer. It is defined as:

$$\mathbf{F}_{\text{Shear}} = \iint_S (\boldsymbol{\tau}_w \cdot \mathbf{e}_x)\,\mathrm{d}A \tag{2.7}$$

where $\boldsymbol{\tau}_w$ is the wall shear stress vector. [11]

For industrial applications, changes in drag coefficient are often expressed in drag counts, where one drag count corresponds to $\Delta C_D = 0.001$, allowing straightforward comparison of small changes caused by geometry modifications or variations in simulation settings. For unsteady simulations, statistical uncertainty in the time-averaged drag coefficient was estimated from the time history of the aerodynamic forces following the methodology of Mockett et al. [12], and a 95 % confidence interval for C_D was constructed on this basis.

When evaluating aerodynamic drag across multiple yaw angles, the overall performance is summarized using a yaw-weighted average (YWA) of the drag coefficient. The average is weighted using realistic wind condition, taking the following form in this study:

$$\text{YWA} = c_1\,C_{D,\,0^\circ} + c_2\,C_{D,\,-2.5^\circ} + c_3\,C_{D,\,-5^\circ} + c_4\,C_{D,\,-7.5^\circ} + c_5\,C_{D,\,-10^\circ}, \tag{2.8}$$

where the coefficients c_i are empirically chosen weighting factors that reflect the relative importance of each yaw angle. The exact values of c_i are omitted here due to confidentiality, but their structure is preserved in the expression above.

2.1.2.2.3 Total Pressure Coefficient

The total pressure coefficient is a non dimensional measure of how the local total pressure differs from the freestream total pressure, normalized by the freestream dynamic pressure. It is defined as:

$$\begin{aligned} C_{p,\text{tot}} &= \frac{p_T - p_\infty}{\frac{1}{2}\rho_\infty V_\infty^2} \\ p_T &= p + \frac{1}{2}\rho V^2 \end{aligned} \tag{2.9}$$

where p_∞, ρ_∞, and V_∞ denote freestream static pressure, density, and velocity, respectively. The local total pressure p_T combines static pressure p and dynamic pressure $\frac{1}{2}\rho V^2$.

Physically, $C_{p,\text{tot}}$ quantifies total pressure losses due to viscous dissipation, flow separation, or shocks. In ideal inviscid flow, total pressure is conserved and $C_{p,\text{tot}} = 1$ everywhere. Values below unity indicate irreversible total pressure losses, making $C_{p,\text{tot}}$ contours particularly valuable for identifying high-loss regions such as vehicle wakes and separated flow zones. [2]

2.1.2.3 Boundary Layers and Wall Units

The aerodynamic forces and total pressure losses discussed previously are fundamentally driven by viscous effects near the vehicle surface, which occur within the boundary layer. A boundary layer is a near-wall region where velocity gradients in the wall-normal direction are large and viscous forces dominate. Within the boundary layer, the flow initially develops in a laminar state and transitions to turbulence after a certain downstream distance. The transition location is commonly characterized using a Reynolds number criterion, but it is also influenced by surface roughness, pressure gradients induced by geometry, and the level of free-stream turbulence. For a flat plate, transition to a turbulent boundary layer typically occurs at a Reynolds number of approximately $Re \approx 10^5$. The boundary layer thickness, δ, is conventionally defined as the wall-normal distance at which the local velocity reaches $0.99 \cdot U_\infty$, marking the transition from the viscous-dominated region to the inviscid free stream. [13]

2.1.2.3.1 y^+

The position within a turbulent boundary layer can be described using the non-dimensional wall distance y^+. The wall-normal distance is expressed in viscous wall units, defined using the friction velocity and the kinematic viscosity as

$$\begin{aligned} y^+ &= \frac{y u_\tau}{\nu} = \frac{\rho u_\tau y}{\mu}, \\ u_\tau &= \sqrt{\frac{\tau_w}{\rho}}, \end{aligned} \tag{2.10}$$

where u_τ is the friction velocity, τ_w is the wall shear stress, and $\nu = \mu/\rho$ is the kinematic viscosity.

Understanding y^+ is crucial, as it describes the position within the boundary layer in viscous units rather than in physical distance. The turbulent boundary layer is commonly divided into the following regions:

- $y^+ \lesssim 5$: Viscous sublayer.
- $5 \lesssim y^+ \lesssim 30$: Buffer layer.
- $y^+ \gtrsim 30$: Logarithmic (log-law) region.

The viscous sublayer is dominated by viscous stresses and lies closest to the wall. Above this region follows the buffer layer, transitioning into the fully turbulent logarithmic region. In regions of flow separation or reattachment, the wall shear stress may approach zero, rendering the definition of wall units ill-conditioned and the interpretation of y^+ less meaningful.

2.1.2.4 Flow Separation

If an adverse pressure gradient is present the near-wall flow decelerates, eventually causing flow reversal within the boundary layer. As shown in Figure 2.2, flow separation occurs at the exact point where the wall shear stress vanishes (zero velocity gradient at the wall). Downstream of this point, the reversed flow detaches from the surface, forming a recirculation zone.

The separated region can be quantitatively identified as the volume enclosed by points where the total pressure coefficient $C_{p,tot}$ is negative. Accurately predicting flow separation is critical for aerodynamic development, as the dominant contribution to drag on heavy vehicles consists of pressure drag, which is largely generated by the wake and the associated separated flow behind the vehicle.

Flow separation tendencies depend strongly on the state of the boundary layer. Laminar boundary layers possess low near-wall momentum and are therefore highly sensitive to geometric disturbances and adverse pressure gradients, leading to early separation. Laminar separation is often associated with the formation of laminar separation bubbles, in which the flow detaches from the surface and transitions to turbulence within the separated shear layer, before potentially reattaching downstream. These bubbles can significantly modify pressure distribution and increase aerodynamic drag.

In contrast, turbulent boundary layers exhibit enhanced mixing and fuller velocity profiles, which increase the momentum close to the wall and enable the flow to remain attached under stronger adverse pressure gradients. When turbulent separation does occur, it is generally characterized by a larger region of reversed flow and a more stable mean separation location, resulting in substantial pressure losses and form drag. Consequently, turbulent boundary layers generally separate further downstream than laminar boundary layers under otherwise similar conditions. [5, 9]

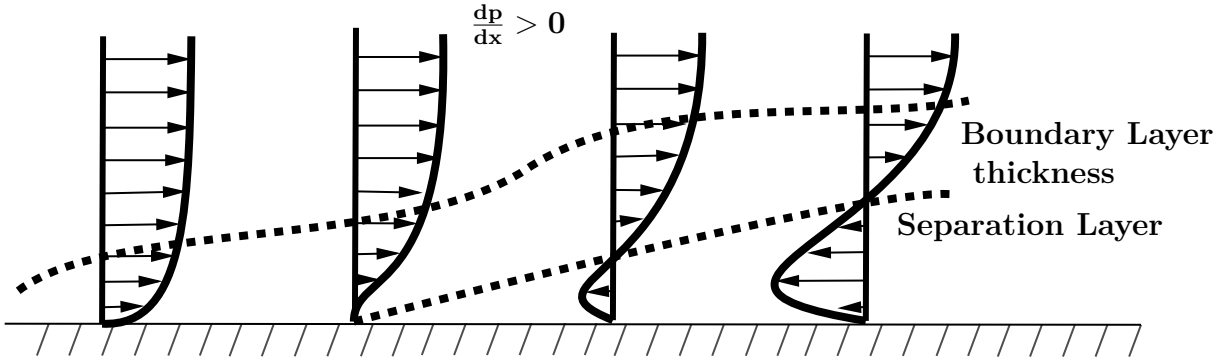

Figure 2.2: Change in boundary layer profile during separation.

2.1.2.5 Vortices

In vehicle aerodynamics, flow separation and sharp geometric edges frequently generate vortical structures and coherent vortex cores. These structures are important because they influence the pressure distribution around the body, the development of the wake, and the overall aerodynamic drag. [2]

In this thesis, vortical structures are identified using the Q-criterion, which compares local rotation and strain,

$$Q = \frac{1}{2}\left(\Omega_{ij}\Omega_{ij} - S_{ij}S_{ij}\right), \tag{2.11}$$

where S_{ij} and Ω_{ij} denote the strain-rate and rotation-rate tensors, respectively [14]. Positive values of Q indicate rotation-dominated regions and are used to visualize coherent vortex cores. [15, 16]

2.2 Computational Fluid Dynamics

While the principles of fluid mechanics describe complex aerodynamic flows, solving the governing equations analytically is impossible for most practical cases. Computational Fluid Dynamics (CFD) is a numerical approach used to solve fluid mechanics problems by numerically solving the governing conservation equations on a discrete computational mesh. A commonly used discretization technique is the Finite Volume Method (FVM). In FVM, the flow domain is divided into a finite number of control volumes, and the governing equations are integrated over each control volume. Gauss's divergence theorem is then applied to convert the volume integrals into surface integrals, which makes it possible to evaluate fluxes across the control-volume faces. [17]

For an incompressible flow, the integral form of the governing equations can be written as:

$$\oint_S v_i n_i \, dA = 0 \tag{2.12}$$

$$\frac{d}{dt}\int_V \rho v_i \, dV + \oint_S \rho v_i v_j n_j \, dA = -\oint_S p n_i \, dA + \oint_S \mu \frac{\partial v_i}{\partial x_j} n_j \, dA + \int_V \rho f_i \, dV \tag{2.13}$$

The continuity equation expresses mass conservation, while the momentum equation represents the balance between transient, convective, pressure, viscous, and body-force terms. By discretizing these integral conservation equations over the computational mesh, the governing equations are transformed into a system of algebraic equations that can be solved numerically.

In industrial applications, CFD typically involves three main steps: pre-processing, solution, and post-processing. The pre-processing stage is crucial, as it includes the generation of watertight geometry, definition of the computational domain, mesh generation, and specification of boundary conditions. During the solution stage, the discretized governing equations are solved iteratively until convergence is reached for steady-state cases, or until the prescribed simulation time is completed for unsteady cases. In the post-processing stage, relevant flow quantities are extracted and visualized to support physical interpretation and performance evaluation. Industrial CFD analyses are commonly carried out using commercial software such as STAR-CCM+, which is used in the present work.

2.3 Turbulence Modeling

Even with a robust numerical framework like FVM, solving the governing fluid equations directly is challenging because turbulent flows contain a wide range of length and time scales, ranging from the largest turbulent eddies down to the smallest dissipative scales. A simulation that resolves all scales of motion is known as a Direct Numerical Simulation (DNS). However, except for very simple problems at low Reynolds numbers, DNS is generally infeasible due to its extremely high computational cost. To reduce computational effort, some or all of the turbulent scales must be modeled. This necessity leads to the commonly used turbulence modeling

approaches in engineering: Large Eddy Simulation (LES), Reynolds-Averaged Navier-Stokes (RANS), and hybrid RANS-LES methods.

2.3.1 Cascade Process and Turbulent Ranges

To understand how these modeling approaches differ, it is first necessary to examine how turbulent kinetic energy is distributed across the range of turbulent scales. This distribution is described by the energy cascade, illustrated by the full energy spectrum in Figure 2.3. Energy is extracted from the mean flow in the energy-containing range (Region I), where the largest eddies are formed, typically on the order of meters. These eddies then break down through the inertial subrange (Region II), transferring energy to progressively smaller structures, until they reach the dissipative range (Region III), where the smallest eddies, typically on the order of micrometers, are damped by viscous effects and the kinetic energy is converted into heat.

An important intermediate scale in this context is the Taylor microscale, which lies between the inertial and dissipative ranges. At this scale, viscous effects begin to influence the turbulent motion, but the eddies have not yet reached the smallest scales where kinetic energy is fully dissipated. The Taylor microscale is therefore useful for estimating the mesh resolution required to resolve turbulence down to the dissipative scale.

Turbulence modeling approaches differ fundamentally based on which ranges of this turbulent spectrum that are modeled. RANS models the entire spectrum of turbulent fluctuations, making it computationally cheap. LES resolves the larger, energy-containing scales of motion while modeling only the smallest dissipative scales (Region III). Hybrid methods, such as Detached Eddy Simulation (DES), combine these approaches spatially by using RANS in the near-wall boundary layer and LES in separated flow regions. More detailed descriptions of the specific turbulence models used in this work are provided in the following sections.

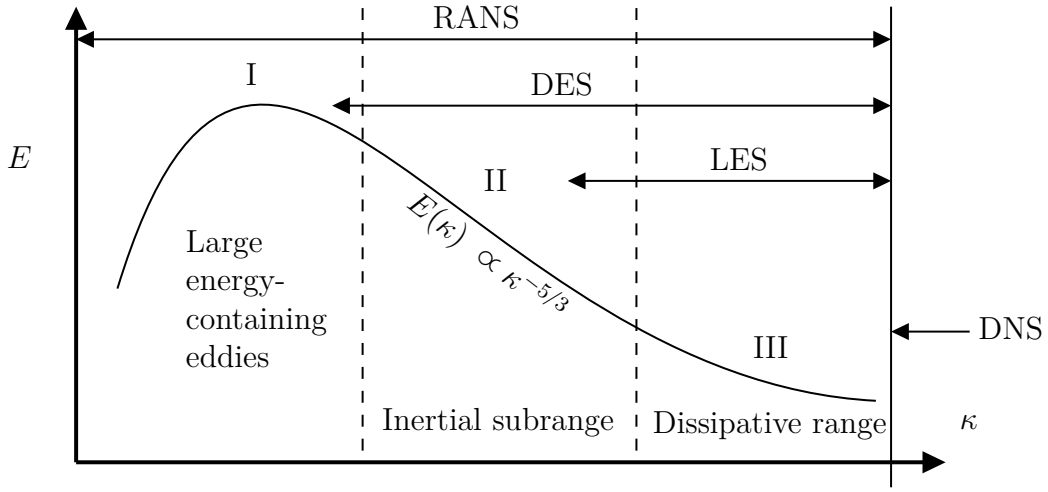

Figure 2.3: Turbulent kinetic energy spectrum illustrating the energy cascade across three primary regions: (I) the energy-containing range, (II) the inertial subrange, and (III) the viscous dissipation range. The spectral energy density E is plotted against the wavenumber κ. Horizontal arrows indicate the portion of the turbulence spectrum modeled by RANS, LES, and DNS approaches.

2.3.2 Reynolds-Averaged Navier-Stokes (RANS)

By modeling the entire turbulent energy spectrum, from the largest energy-containing eddies down to the dissipative range, the Reynolds-Averaged Navier-Stokes (RANS) framework is the computationally cheapest model used in this study. Instead of explicitly resolving transient turbulent structures, RANS utilizes a statistical averaging technique to account for the overall influence of turbulence on the mean flow.

This is achieved by decomposing the velocity field into mean and fluctuating parts,

$$v_i = \overline{v}_i + v_i', \tag{2.14}$$

where the overbar denotes time averaging and the prime denotes fluctuations. Time averaging is defined as:

$$\overline{v_i} = \frac{1}{2T}\int_{-T}^{T} v_i(\tau)\,\mathrm{d}\tau. \tag{2.15}$$

Time averaging the fluctuations results in $\overline{v_i'} = 0$. Substituting the decomposition into (2.1) and (2.2) and assuming a steady mean flow yields the steady RANS equations:

$$\frac{\partial \overline{v}_i}{\partial x_i} = 0, \tag{2.16}$$

$$\rho\frac{\partial \overline{v}_i\overline{v}_j}{\partial x_j} = -\frac{\partial \overline{p}}{\partial x_i} + \frac{\partial}{\partial x_j}\left(\mu\frac{\partial \overline{v}_i}{\partial x_j} - \rho\overline{v_i'v_j'}\right), \tag{2.17}$$

where $-\rho\overline{v_i'v_j'}$ represents the Reynolds stress tensor [14].

To close the RANS equations, the unknown Reynolds stresses are modeled using the Boussinesq hypothesis, which relates them to the mean strain rate tensor S_{ij} via a kinematic eddy viscosity ν_t:

$$-\overline{v_i'v_j'} = 2\nu_t S_{ij} - \frac{2}{3}k\delta_{ij}. \tag{2.18}$$

2.3.2.1 The k–ε Model

The standard k–ε model solves two additional transport equations to compute the turbulent kinetic energy k and its dissipation rate ε, defining the eddy viscosity as:

$$\nu_t = c_\mu\frac{k^2}{\varepsilon}, \qquad c_\mu = 0.09. \tag{2.19}$$

For steady flow, the modeled transport equations are given by:

$$\overline{v}_j\frac{\partial k}{\partial x_j} = \frac{\partial}{\partial x_j}\left[\left(\nu + \frac{\nu_t}{\sigma_k}\right)\frac{\partial k}{\partial x_j}\right] + P_k - \varepsilon, \tag{2.20}$$

$$\overline{v}_j\frac{\partial \varepsilon}{\partial x_j} = \frac{\partial}{\partial x_j}\left[\left(\nu + \frac{\nu_t}{\sigma_\varepsilon}\right)\frac{\partial \varepsilon}{\partial x_j}\right] + c_{\varepsilon 1}\frac{\varepsilon}{k}P_k - c_{\varepsilon 2}\frac{\varepsilon^2}{k}, \tag{2.21}$$

where the production of turbulent kinetic energy is $P_k = 2\nu_t S_{ij}S_{ij}$, and the mean strain rate tensor is defined as:

$$S_{ij} = \tfrac{1}{2}\left(\frac{\partial \overline{v}_i}{\partial x_j} + \frac{\partial \overline{v}_j}{\partial x_i}\right). \tag{2.22}$$

[14]

2.3.2.2 The Elliptic Blending Model

While the standard k–ε model is computationally robust, it assumes isotropic turbulence and struggles to accurately resolve near-wall flows and stagnation regions without relying on empirical damping functions. To address these limitations, the k–ε framework can be extended into a four-equation model using the Elliptic Blending (EB) approach.

The EB model supplements the k and ε transport equations with equations for the normalized wall-normal stress component,

$$\varphi = \frac{\overline{v^2}}{k}, \tag{2.23}$$

and an elliptic blending factor, α. This blending factor smoothly transitions the turbulence closure from the highly anisotropic viscous sublayer to the fully turbulent outer region. These quantities are then used to compute the turbulent eddy viscosity as:

$$\mu_t = \rho\, C_\mu\, \varphi\, k\, \min\left(T,\ \frac{C_T}{\sqrt{3\, C_\mu\, \varphi}\, S}\right). \tag{2.24}$$

In this study, the commercial solver Simcenter STAR-CCM+ is utilized, which provides two primary variants of this model [18]. The Standard Elliptic Blending (SEB) variant is based on the Billard–Laurence formulation. It includes modifications intended to improve robustness in complex flow geometries, offering better near-wall accuracy than the realizable k–ε model and improved numerical stability compared to the SST k–ω model.

The second variant, Lag Elliptic Blending (LEB), combines the standard EB formulation with a stress-strain lag concept. Linear eddy-viscosity models generally tend to overpredict turbulent kinetic energy production in non-equilibrium regions, such as flow separation around a truck, where principal stresses and strain rates become misaligned. The LEB formulation mitigates this by accounting for the angle between these directions, introducing additional terms to capture anisotropy, curvature, and rotational effects. [18]

2.3.2.3 The k–ω SST Model

The k–ω Shear Stress Transport (SST) turbulence model, introduced by Menter [19], was developed to overcome the near-wall deficiencies of the standard k–ε model. It combines the near-wall accuracy of the k–ω formulation with the robustness and free-stream independence of the k–ε model. This is achieved through the use of a blending function, F_1, which activates the k–ω equations in the near-wall region and gradually transitions to a transformed k–ε formulation in the outer wake region of the boundary layer and free shear flow. The governing transport equations for the turbulent kinetic energy k and the specific dissipation rate ω are obtained by multiplying the respective model equations by the blending function and combining them:

$$\begin{aligned}
\frac{\partial k}{\partial t} + \frac{\partial}{\partial x_j}\left(\bar{v}_j k\right) &= \frac{\partial}{\partial x_j}\left[\left(\nu + \frac{\nu_t}{\sigma_k}\right)\frac{\partial k}{\partial x_j}\right] + P_k - \beta^* k\omega, \\
\frac{\partial \omega}{\partial t} + \frac{\partial}{\partial x_j}\left(\bar{v}_j \omega\right) &= \frac{\partial}{\partial x_j}\left[\left(\nu + \frac{\nu_t}{\sigma_\omega}\right)\frac{\partial \omega}{\partial x_j}\right] + \alpha\frac{P_k}{\nu_t} - \beta\omega^2 \\
&\quad + 2(1-F_1)\sigma_{\omega 2}\frac{1}{\omega}\frac{\partial k}{\partial x_i}\frac{\partial \omega}{\partial x_i}.
\end{aligned} \tag{2.25}$$

In adverse pressure-gradient flows, the SST k-ω model has been shown to overpredict turbulent shear stresses. As noted by Menter [19], improved predictions can be achieved by limiting the eddy viscosity using a formulation inspired by the Johnson-King model. Accordingly, the turbulent eddy viscosity is defined as

$$\nu_t = \frac{a_1 k}{max(a_1\omega, \Omega F_2)} \tag{2.26}$$

The blending function F_2 is equal to unity within boundary-layer flows and tends to zero in free shear regions. As a result, the eddy viscosity is reduced by the Johnson-King formulation in large adverse pressure gradients while reverting to the standard k-ω model in the outer flow.

2.3.2.4 The URANS Model

The steady RANS equations derived above assume a statistically stationary mean flow. Relaxing this assumption and allowing the mean flow quantities to vary in time yields the Unsteady Reynolds-Averaged Navier–Stokes (URANS) formulation [14]. This extension is particularly relevant for bluff bodies such as heavy trucks, where large-scale unsteady structures, including periodic wake shedding and recirculating regions, cause the mean flow to vary at low frequencies.

The URANS equations are obtained by applying the usual Reynolds decomposition while retaining the unsteady term in the mean-flow equations. [14] Rather than the fixed time average in Equation (2.15), a sliding time-window average is introduced:

$$\overline{v}(t) = \frac{1}{2T}\int_{t-T}^{t+T} v(\tau)\,\mathrm{d}\tau, \qquad v = \overline{v} + v'', \tag{2.27}$$

where T is the averaging window chosen to be large relative to turbulent fluctuations but small relative to the resolved unsteady motion, and v'' denotes the turbulent fluctuation.

Intermittency-Based Transition Modeling

The k-ω SST and k-ε based models assume fully turbulent flow throughout the domain. In practice, however, the boundary layer along truck surfaces undergoes a laminar-to-turbulent transition that can influence the predicted separation location and drag. To account for this, a transition model is coupled with the k-ω SST framework and later extended to the hybrid RANS/LES approach described in section 2.3.4.1. The elliptic blending model, by contrast, incorporates a near-wall damping function that naturally reproduces the suppression of turbulence close to the wall, and does not require an additional transition model. [18]

Transition from laminar to turbulent flow is not instantaneous but occurs through the appearance of turbulent fluctuations. This behavior can be represented through the intermittency, γ, which denotes the fraction of time during which the flow is turbulent. A value of $\gamma = 0$ corresponds to fully laminar flow, while $\gamma = 1$ indicates fully turbulent flow. Intermittency-based transition models modulate turbulence production in order to gradually induce turbulent behavior within the transition region.

Traditional transition modeling approaches often rely on non-local boundary-layer quantities, such as the momentum thickness Reynolds number, which can be difficult to evaluate in complex geometries or flows without a well-defined free stream. The γ-Re_θ model addresses this by reformulating the transition criteria in terms of local flow variables, making it applicable to general CFD problems.

γ-Re_θ Transition Model

To overcome these limitations, Menter et al. [20] proposed the γ-Re_θ transition model formulated for use in general CFD codes. In this model, the intermittency variable γ is governed by a transport equation. Rather than directly computing the momentum thickness Reynolds number, the model relates it to a local vorticity Reynolds number. The transition onset momentum thickness Reynolds number is obtained from empirical correlations fitted to experimental data and transported through an additional transport equation, allowing the model to predict transition onset using only local flow variables.

2.3.3 Large Eddy Simulation

Unlike the RANS and URANS approaches, which model the entire turbulent energy spectrum through statistical averaging, Large Eddy Simulation (LES) employs a spatial filtering operation to explicitly resolve the large, energy-containing eddies while modeling only the smaller, more universal subgrid-scale (SGS) stresses. The spatially filtered variables are functions of both space and time, which means that LES can resolve only motions on the order of the grid spacing and larger, while smaller scales are represented through SGS modeling. The filtered governing equations for incompressible flow take the form:

$$\begin{aligned} \frac{\partial \bar{v}_i}{\partial t} + \frac{\partial}{\partial x_j}\left(\bar{v}_i \bar{v}_j\right) &= -\frac{1}{\rho}\frac{\partial \bar{p}}{\partial x_i} + \nu \frac{\partial^2 \bar{v}_i}{\partial x_j^2} - \frac{\partial \tau_{ij}}{\partial x_j}, \\ \frac{\partial \bar{v}_i}{\partial x_i} &= 0, \end{aligned} \tag{2.28}$$

where the SGS stress tensor, representing the unresolved small-scale contributions, is defined as:

$$\tau_{ij} = \overline{v_i v_j} - \bar{v}_i \bar{v}_j. \tag{2.29}$$

The SGS tensor is commonly modeled using the Boussinesq approximation as

$$\tau_{ij} - \frac{1}{3}\tau_{kk}\delta_{ij} = -2\nu_{sgs}\bar{s}_{ij}, \tag{2.30}$$

where

$$\bar{s}_{ij} = \frac{1}{2}\left(\frac{\partial \bar{v}_i}{\partial x_j} + \frac{\partial \bar{v}_j}{\partial x_i}\right). \tag{2.31}$$

To apply the Boussinesq approximation, a model for the subgrid-scale kinematic viscosity is needed. [14]

WALE Subgrid-Scale Model

The SGS stresses must be modeled to close the filtered equations. One of the LES subgrid-scale models available in STAR-CCM+ is the Wall-Adapting Local Eddy-viscosity (WALE) model [18], which computes the turbulent viscosity as:

$$\rho\nu_{sgs} = \mu_t = \rho\Delta^2 S_w, \tag{2.32}$$

where ρ is the density, Δ is the grid filter width, and S_w is the deformation parameter. The filter width is defined based on the cell volume V as:

$$\Delta = \begin{cases} C_w V^{1/3} & \text{(outer region)}, \\ \min(\kappa d,\, C_w V^{1/3}) & \text{(near-wall region)}, \end{cases} \tag{2.33}$$

where C_w is a model coefficient, κ is the von Kármán constant, and d is the wall distance.

Wall-Modeled LES

For high-Reynolds-number flows, fully resolving the near-wall turbulent scales becomes computationally prohibitive. The cost scales approximately as $Re^{0.5}$ when only the outer layer is resolved, but increases to about $Re^{2.4}$ when the inner layer is fully resolved [21]. In wall-modeled LES (WM LES), the near-wall stresses are therefore not directly resolved but are instead replaced by a wall model that assumes the near-wall flow behaves as a turbulent boundary layer. The specific wall-treatment approaches used in this study are discussed in Section 2.3.5 in the context of the hybrid RANS-LES framework.

2.3.4 Hybrid RANS-LES

Pure RANS models are computationally efficient but struggle to capture the large-scale unsteady structures characteristic of bluff-body aerodynamics. Hybrid RANS-LES approaches address this by applying RANS treatment in attached boundary layers, where it is most reliable, while resolving turbulent fluctuations in separated and free-shear regions where LES is more appropriate.

2.3.4.1 Detached Eddy Simulations (DES)

The Detached Eddy Simulation (DES) turbulence model is a hybrid model that combines RANS and LES approaches using a single, non-zonal formulation. DES models aim to model

boundary layer flow using RANS and resolve turbulent fluctuations using LES in separated regions. [22]

Following [18],the dissipation term in the k-equation is modified to enable the LES–RANS transition for **k-ω DES**:

$$\beta^* k\omega \;\rightarrow\; \beta^* k\omega F_{\mathrm{DES}}, \qquad F_{\mathrm{DES}} = \max\!\left(\frac{L_t}{C_{\mathrm{DES}}\Delta}, 1\right), \tag{2.34}$$

where the turbulent length scale and grid length are defined as

$$L_t = \frac{\sqrt{k}}{\beta^*\omega}, \qquad \Delta = \max\{\Delta x_1, \Delta x_2, \Delta x_3\}. \tag{2.35}$$

[18]

2.3.4.2 Delayed DES (DDES)

Delayed Detached Eddy Simulation (DDES) is a refinement of the original DES formulation, developed to address a known shortcoming that can arise when the computational grid is highly refined in the wall-parallel directions within the boundary layer. In such cases, the DES blending function may prematurely switch from RANS to LES mode inside the attached boundary layer, where the LES subgrid-scale model is not suited to sustain the near-wall turbulence. This leads to a nonphysical reduction in modeled Reynolds stresses and can cause spurious flow separation, a phenomenon known as grid-induced separation.

DDES resolves this by introducing a shielding function F_{S}, which acts to protect the boundary layer from premature LES activation. In this study, DDES is used in conjunction with the k–ω SST model, where F_{S} typically takes the form of the F_1 or F_2 blending functions already present in that model [23], with $F_{\mathrm{S}} \to 1$ inside the attached boundary layer and $F_{\mathrm{S}} \to 0$ in the free stream and separated regions.

The modified blending function is defined as:

$$F_{\mathrm{DDES}} = \max\left\{\frac{L_t}{C_{\mathrm{DES}}\Delta}(1 - F_{\mathrm{S}}),\, 1\right\}, \tag{2.36}$$

where L_t is the turbulent length scale, C_{DES} is a model constant, and Δ is the local grid filter width. The shielding function ensures that RANS remains active throughout the attached boundary layer, with LES only activated in regions of genuine flow separation.

The **Elliptic Blending DDES (DDES EB)** formulation is based on the k-ε RANS model. In this approach, the dissipation term in the transport equation for the turbulent kinetic energy is modified by replacing ε with $\tilde{\varepsilon}$:

$$\begin{aligned}
\tilde{\varepsilon} &= \frac{k^{3/2}}{\tilde{d}} \\
\tilde{d} &= \frac{k^{3/2}}{\varepsilon} - f_d \max\left(0, \frac{k^{3/2}}{\varepsilon} - \psi C_{DES}\Delta\right) \\
\psi &= \frac{C_{\varepsilon 1}}{C_{\varepsilon 2} C_\mu \varphi}
\end{aligned} \tag{2.37}$$

Here, $C_{\varepsilon 1}$, $C_{\varepsilon 2}$, and C_{μ} are coefficients from the Elliptic Blending model formulation. The function f_d is a transition function that takes the value 1 in LES regions and 0 elsewhere. Furthermore, C_{DES} is a model coefficient and Δ is the grid filter width. [18]

Improved DDES (IDDES)

The IDDES model is a hybrid RANS–LES approach that extends DDES with an improved wall-modeled LES capability. It is formulated as a single framework that can operate either in a WM LES-like mode or in a DDES-like mode depending on the flow conditions. When sufficient resolved turbulence is present, the model behaves as WM LES, resolving most of the turbulence outside the near-wall region. When such turbulence is absent, it behaves as DDES, providing RANS treatment in attached boundary layers and LES-like behavior mainly in separated regions. [24]

In the IDDES formulation, the specific dissipation rate ω of the baseline k-ω model is replaced by

$$\tilde{\omega} = \frac{\sqrt{k}}{l_{\text{HYBRID}}\, f_{\beta^*}\, \beta^*} \quad , \tag{2.38}$$

where l_{HYBRID} is a hybrid length scale that determines the local RANS or LES character of the model. It is defined as

$$l_{\text{HYBRID}} = \tilde{f}_d\,(1 + f_e)\, l_{\text{RANS}} + \left(1 - \tilde{f}_d\right) C_{\text{DES}} \Delta_{\text{IDDES}}. \tag{2.39}$$

Here, $\tilde{f}_d$ blends between the near-wall RANS branch and the outer LES branch, while f_e helps maintain sufficient modeled stress in the transition region. A key feature of IDDES is that Δ_{IDDES} depends on both grid spacing and wall distance, which improves the wall-modeled LES behavior and reduces log-layer mismatch. [24]

2.3.4.3 Scale Resolving Hybrid (SRH)

Unlike DDES and IDDES, which use explicit blending functions to define RANS and LES regions, the Scale-Resolved Hybrid (SRH) model provides a continuous transition between RANS-like and LES-like behavior based on the local mesh and time-step resolution. On coarse meshes and large time steps, it behaves as RANS, while on sufficiently fine meshes and small time steps it resolves the larger turbulent structures.

The SRH model is based on spatial and temporal filtering of the Navier-Stokes equations, where the flow variable is decomposed as

$$\phi = \bar{\bar{\phi}} + \phi', \tag{2.40}$$

with $\bar{\bar{\phi}}$ denoting the resolved component and ϕ' the unresolved sub-filter contribution. The resulting sub-filter stress tensor is modeled using the Boussinesq hypothesis,

$$\tau_{ij,\text{sfs}} = -2\nu_{\text{sfs}} \bar{\bar{S}}_{ij} + \frac{2}{3} k_{\text{sfs}} \delta_{ij}, \tag{2.41}$$

where ν_{sfs} is the sub-filter viscosity, $\bar{\bar{S}}_{ij}$ the resolved strain-rate tensor, and k_{sfs} the sub-filter turbulent kinetic energy. [18]

Duffal et al. [25] proposed a hybrid temporal LES (HT LES) formulation based on an eddy-viscosity closure with shielding of near-wall resolved turbulence. In STAR-CCM+, this formulation is implemented as SRH with k-ω and k-ε closures. The transition between modeled and resolved turbulence is controlled by a hybridization function using a shielding function f_s, defined as

$$f_s = 1 - \tanh\left[\left(r_{dc}\frac{\nu^{3/4}}{\varepsilon^{1/4}d_2}\right)^8\right] \tag{2.42}$$

which depends on the ratio of a Kolmogorov-based length scale to the wall distance, ensuring appropriate near-wall damping and a smooth transition between RANS and LES behavior.

2.3.5 Wall Modeling

Wall modeling is the process of representing the flow near the wall without resolving the boundary layer. STAR-CCM+ has two approaches both using wall functions, the Low-y^+ and All-y^+ approach.

Low-y^+ Approach

In the Low-y^+ formulation, the wall shear stress is computed assuming the near-wall cell lies within the viscous sub-layer. The friction velocity is given by

$$u_\tau = \frac{\mu\,|\overline{\boldsymbol{v}}_{\text{tangential}}|}{\rho d}, \tag{2.43}$$

where μ is the dynamic viscosity, $\overline{\boldsymbol{v}}_{\text{tangential}}$ is the LES-filtered velocity component tangential to the wall, ρ is the fluid density, and d is the distance from the wall to the centroid of the near-wall cell. [18]

All-y^+ Approach

The All-y^+ formulation is applicable over the entire near-wall region, from the viscous sub-layer through the logarithmic layer. In this approach, the friction velocity is obtained implicitly as

$$\begin{aligned} u_\tau &= u^*, \\ u^* &= \frac{u}{u^+}, \\ u^+ &= \frac{1}{\kappa}\left(1+\kappa y^+\right) + C\left(1 - \mathrm{e}^{-y^+/y_m^+} - \frac{y^+}{y_m^+}\mathrm{e}^{-by^+}\right), \end{aligned} \tag{2.44}$$

where u^+ is defined with a blended wall function given by Reichardt's law [26]. Here, κ denotes the von Kármán constant, and C, y_m^+, and b are empirical constants defining the smooth transition between the viscous and logarithmic regions. [18]

2.4 Wind Tunnel and Experimental Testing

The turbulence models and numerical methods described above require experimental data for validation before their results can be considered reliable. Wind tunnels provide a controlled and reproducible environment for this purpose, free from the variability of on-road conditions,

making them well suited for systematic correlation with CFD simulations. As computational methods have matured in both accuracy and turn-around time, the role of wind tunnel testing has shifted accordingly, with its function now being more as a tool for the validation and correlation of numerical predictions rather than standalone aerodynamic development [27].

A wind tunnel produces a controlled stream of air with low freestream turbulence, allowing aerodynamic forces and flow behavior to be measured under repeatable conditions. In its simplest form, it consists of an inlet with a turbulence screen, a test section where the model is placed, and an outlet diffuser. Wind tunnels are broadly classified as either open-loop (Eiffel type) or closed-loop (Göttingen type), depending on whether the outlet reconnects to the inlet. Figure 2.4 shows the main test section of the NRC wind tunnel in Canada, with the inlet contraction cone, test section, and outlet diffuser visible.

Wind tunnels for automotive purposes often include a force balance mounted on a turntable for aerodynamic force measurements, a belt-driven wheel rotation system, and a moving ground system to simulate road conditions. For trucks, however, size constraints typically require tests to be conducted with stationary wheels and a fixed ground, which introduces known discrepancies relative to on-road conditions. The test section itself can take several forms, with open and closed configurations being the most common, though slotted, streamlined, and adaptive variants have also been developed to reduce blockage and wall interference effects.

Wind tunnels are subject to several sources of error, including blockage, ground simulation, and wheel behavior, which can cause aerodynamic forces to be overpredicted relative to open-road conditions and CFD simulations [2].

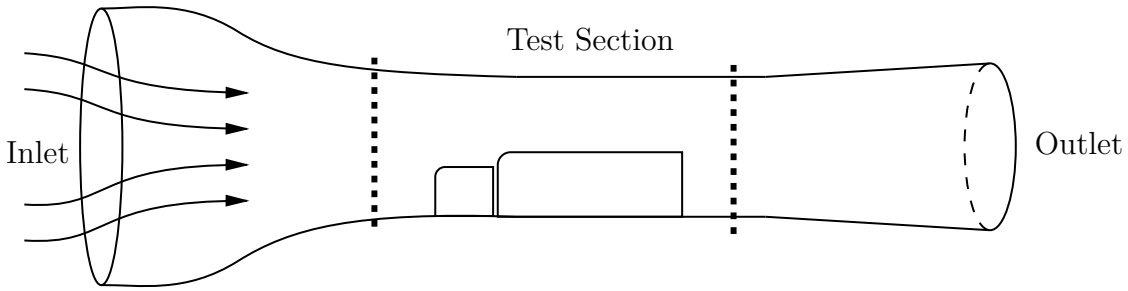

Figure 2.4: Schematic representation of the main section of the NRC wind tunnel in Canada.

2.4.1 Blockage

Blockage is the physical phenomenon of the flow being constricted and affected due to the presence of the test object in the tunnel. Blockage arises when the presence of the test object in the tunnel constricts the surrounding flow, artificially accelerating it relative to open-road conditions. A blockage ratio below 10% is generally recommended to limit interference effects [2], and corrections are applied when this threshold is exceeded.

Blockage ratio is defined as:

$$\varphi = \frac{A_x}{A_N} \tag{2.45}$$

where A_x is defined as the frontal projected area of the vehicle and A_N is the cross sectional area of the test section. [2, 28]

2.4.2 Experimental Measurement Techniques

The most common way of measuring the wind tunnel test velocity is through pitot-static probes using the dynamic pressure, q_∞, defined as:

$$q_\infty = p_{\text{tot}} - p_{\text{stat}} = \frac{1}{2}\rho_\infty u_\infty^2, \tag{2.46}$$

from which the freestream velocity is obtained as:

$$u_\infty = \sqrt{\frac{2q_\infty}{\rho_\infty}}. \tag{2.47}$$

Aerodynamic forces and moments are measured using a balance rigidly connected to the vehicle model and isolated from the wind tunnel structure. The balance can be mounted either externally or internally, in the latter case placed inside the test object itself.

Surface pressures can be measured using pressure taps connected to scanners, while flow-field pressures and velocities are mapped using pitot-static probes or multi-hole pressure probes, enabling three-dimensional reconstruction of the surrounding flow. [2]

3

Turbulence Modeling for Bluff-Body and Vehicle Aerodynamics

This chapter reviews the accuracy and computational cost of turbulence modeling approaches for external automotive aerodynamics, progressing from high-fidelity LES references through wall-modeled and hybrid RANS–LES methods, and concludes by identifying the research gap that motivates the modeling and comparison strategy used in the present study.

3.1 High-Fidelity and Wall-Modeled LES

Extensive research has been conducted on turbulence modeling in aerodynamic flows. For high-fidelity simulations and reference solutions, large-eddy simulations (LES), described in section 2.3.3, are often employed. However, LES remains prohibitively expensive for industrially relevant Reynolds numbers. A commonly used benchmark configuration is the Ahmed body, introduced by Ahmed *et al.* [29] and visualized in Figure 3.1. It is a simplified car geometry that has been the subject of numerous experimental and numerical investigations.

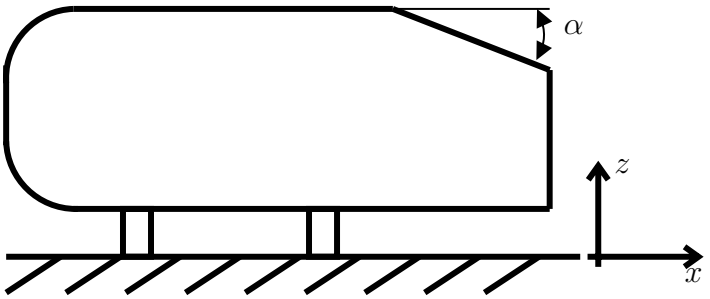

Figure 3.1: Schematic illustration of the Ahmed body. α denotes the rear slant angle.

Krajnović and Davidson [30] performed LES of the Ahmed body with a 25° rear slant and compared their results with experimental data by Lienhart *et al.* [31]. Their simulations were conducted at a reduced Reynolds number of $Re = 0.2 \times 10^6$, showing good agreement with experiments using a mesh of approximately 16.5 million cells. Subsequently, Menter *et al.* [32] reported similar findings at low Reynolds numbers and extended the study to $Re = 0.768 \times 10^6$. For this case, LES required meshes ranging from 230×10^6 to 320×10^6 cells to achieve satisfactory agreement with experimental data, illustrating the drastic increase in computational cost with increasing Reynolds number.

The scaling of grid requirements with Reynolds number has been analyzed by Krajnović [33]. Based on maintaining near-wall resolutions of $\Delta x^+ \simeq 20$–145 in the streamwise direction and $\Delta z^+ \simeq 15$–40 in the spanwise direction, as recommended by Piomelli and Chasnov [34], the total number of near-wall cells increases approximately as $\mathcal{O}(Re^{1.8})$ when refining only streamwise and spanwise. As discussed in section 2.1.2.2.1, characteristic Reynolds numbers for automotive aerodynamics are typically in the range 10^6–10^7, rendering wall-resolved LES computationally infeasible for practical applications.

To significantly reduce the computational cost of LES, the application of wall-modeled LES (WM LES), see section 2.3.3, has been investigated for the Ahmed body configuration. Kolmogorov *et al.* [35] studied the mesh requirements for LES with wall functions (WF LES) and concluded that at least 10 cells are required across the boundary layer in the wall-normal direction, with a cell aspect ratio not exceeding 2 (i.e., rectangular cells with streamwise and spanwise side lengths at most twice the wall-normal height).

Applying WF LES to the flow around the Ahmed body with a 25° rear slant at $Re = 2.8 \times 10^6$, Kolmogorov *et al.* [36] showed that while the main flow features were captured, more sensitive phenomena such as flow separation and reattachment were not accurately predicted, even when the recommended WM LES mesh requirements were satisfied using approximately 100 million cells. Similarly, Menter *et al.* [32] reported that simulations with around 100 million cells led to an underprediction of turbulent kinetic energy in the separation region and poor prediction of the separation location upstream of the rear slant. This deficiency was attributed to boundary-layer thinning caused by flow acceleration near the slanted surface, which demands locally refined wall-normal resolution.

3.2 Hybrid RANS–LES Methods on Automotive Geometries

Hybrid RANS–LES approaches have also been applied to the Ahmed body. In a study by Guilmineau *et al.* [37], RANS, DES, and IDDES based on the k-ω SST model were evaluated for rear slant angles of 25° and 35° on meshes containing approximately 23 million cells. For the 35° case, all models captured the principal flow structures with reasonable accuracy, although DES and IDDES yielded the best overall agreement. The 25° case was more demanding, and only IDDES was able to predict the separation bubble on the slanted surface, albeit with an overestimated size. In comparison, RANS predicted excessive separation and an unrealistically large wake.

Further studies on DDES applied to the Ahmed body showed that, on sufficiently resolved grids, hybrid methods offer advantages over RANS models [38]. In a subsequent study, improved performance of IDDES relative to RANS was also reported, although hybrid models were still found to struggle with accurately capturing separation and reattachment [4].

Hybrid models were also applied to the realistic generic car geometry DrivAer, introduced by Heft *et al.* [39] and shown in Figure 3.2, where they again outperformed RANS in the prediction of aerodynamic coefficients [4]. The differences between SA-IDDES, SA-DDES, and SST-IDDES were relatively small on coarse meshes, while noticeable improvements were observed for SST-IDDES with mesh refinement. In contrast, RANS models failed to accurately predict the drag coefficient C_d and surface pressure distribution C_p. Although DES-based

methods provided improved global predictions, they were still unable to fully capture the correct flow topology.

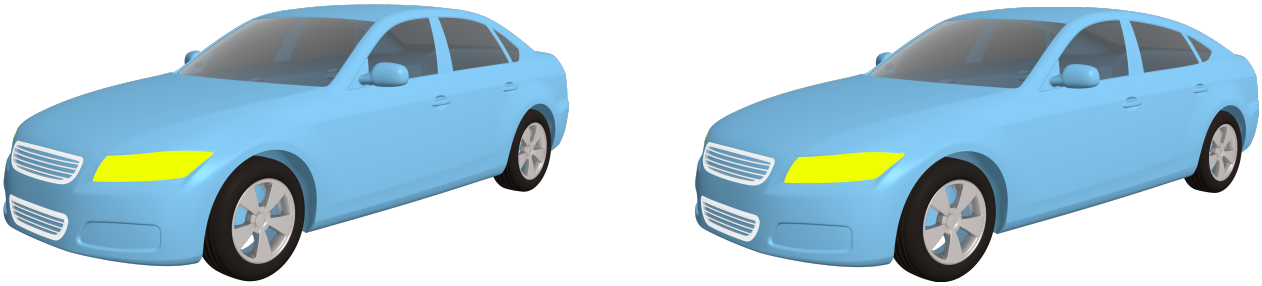

(a) Notchback configuration. **(b)** Fastback configuration.

Figure 3.2: DrivAer model in two configurations. Geometry courtesy of the Chair of Aerodynamics and Fluid Mechanics, Technical University of Munich [39].

Further investigations by Ekman [5] of DES and DDES on the Ahmed body showed that both DES and DDES suffer from insufficient shielding compared to the Stress-Blended Eddy Simulation (SBES) model proposed by Menter [40]. A similar comparison on the DrivAer geometry demonstrated superior performance of SBES, whereas DDES overpredicted separation at the rear window and IDDES underpredicted separation. According to Ekman [5], the relatively poorer performance of DDES and IDDES is attributed to their slower transition from RANS to LES mode compared with SBES. However, the SBES model is not available in STAR-CCM+.

3.3 Alternative and Simplified Test Geometries

Since the aerodynamics of trucks differ from those of cars, turbulence-model accuracy for simplified truck geometries is of particular interest. One such geometry is the Allan body introduced by J.W. Allan [7] and described in Chapter 4, which was originally studied through wind-tunnel experiments. Large-eddy simulations (LES) of this model were performed by Östh and Krajnović [41], revealing flow separation, attached boundary-layer regions, and complex cab–trailer interactions. Further investigations by Josefsson [42] reported comparable drag coefficient predictions (C_D) using IDDES when compared with the LES results of Östh and Krajnović. Ekman [5] further showed that both DDES and SBES provide good pressure correlations with experimental data in the gap between cab and trailer.

To address the poor separation predictions of RANS-based models, transition models can be employed to improve the modeling of boundary-layer transition. Hodara *et al.* [43] investigated a hybrid RANS-LES approach coupled with the γ–Re_θ transition model and reported improved agreement with experimental data for flow over a cylinder. Similarly, Mays *et al.* [44] assessed several turbulence modeling approaches, including RANS, URANS, and hybrid RANS-LES methods for flow over a cylinder. They found that the k–ω SST model in RANS predicted premature separation, a deficiency that persisted in the SST-DDES formulation, while the γ–Re_θ transition model provided only marginal improvement. In contrast, the scale-resolving hybrid (SRH) model, see section 2.3.4.3, demonstrated better performance than URANS both with and without transition modeling. When combined with the γ–Re_θ transition model, SRH achieved agreement comparable to WALE-based LES, indicating its improved capability

to capture separation and transition-sensitive flow features.

Chen *et al.* [45] compared RANS, IDDES, and SRH models, with and without transition modeling, against LES for a 1:15 scale train at a yaw angle of 30°. The LES results were validated against experimental data from a 1:10 scale model at a higher Reynolds number, showing good agreement. Enabling the transition model within IDDES reduced deviations from the LES reference to below one percent. The SRH model also showed good agreement when combined with transition modeling, although its accuracy was slightly worse than the IDDES on fine meshes. However, the SRH model retained better predictive performance for coarser meshes.

3.4 Temporal Resolution and Time-Stepping Effects

When selecting a time step for transient simulations, the mesh resolution and local flow velocity place an important constraint on the choice. The Courant–Friedrichs–Lewy (CFL) condition is a numerical stability criterion that sets an upper bound on the time step when solving certain partial differential equations [46]. In CFD, the CFL number measures how far a fluid parcel travels relative to the cell size during one time step. Having a large CFL number can lead to numerical instability and increased temporal discretization error in the simulation. The general recommendation for hybrid RANS–LES simulations is to choose the time step such that the CFL condition $\mathrm{CFL} < 1$ is satisfied throughout the simulation domain. For high velocity flows combined with fine computational meshes, this condition can lead to prohibitively small time steps and consequently very high computational cost.

Ekman *et al.* [47] investigated the influence of temporal resolution for scale-resolving simulations of the DrivAer notchback model, shown in Figure 3.2a, using a hybrid RANS–LES approach. In their study, the finest temporal resolution corresponded to a CFL number below 1, while the coarsest case reached CFL numbers of approximately 100. The results showed that increasing the time step substantially had limited effect on the predicted aerodynamic forces and main flow features. In particular, simulations performed with time steps corresponding to approximately $\mathrm{CFL} \approx 20$ produced aerodynamic forces and flow structures that remained close to the well-resolved reference case. At the same time, the computational cost was reduced by more than 90%, demonstrating that a significant reduction in simulation time can be achieved without severely compromising accuracy. Minor differences were mainly observed in local quantities such as pressure and skin friction distributions, while global quantities such as the drag coefficient were only weakly affected. Increasing the time step such that $\mathrm{CFL} \approx 50$ or greater affected local quantities such as separation points but resulted in similar general flow features.

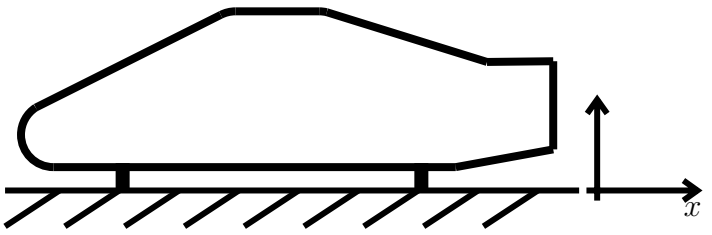

Figure 3.3: Schematic illustration of the SAE notchback.

Aultman *et al.* [48] performed a similar investigation using URANS and Delayed Detached Eddy Simulation (DDES) on the SAE notchback model shown in Figure 3.3 and the DrivAer fastback model shown in Figure 3.2b. In their work, the smallest time step corresponded to a temporally well-resolved case with an average CFL number close to 1. The time step was then increased by factors of 10, 20, 50, and 100. Their results showed that time-averaged aerodynamic quantities, including drag buildup and mean flow field characteristics, remained in close agreement with the reference solution for time steps up to approximately 50 times larger than the baseline case. While some deterioration of resolved unsteady structures occurred for the largest time steps, the predicted mean flow field still showed much closer agreement with the temporally resolved simulations than steady RANS solutions.

These results suggest that the classical guideline of maintaining CFL < 1 throughout the entire computational domain can be overly restrictive when the primary objective is the prediction of time-averaged aerodynamic quantities. Allowing moderately larger time steps can therefore provide a substantial reduction in computational cost while still maintaining acceptable accuracy in the predicted forces and dominant flow structures.

3.5 Summary and Research Gap

Taken together, the reviewed studies indicate that while hybrid RANS–LES approaches generally outperform steady and unsteady RANS for separated automotive flows, their predictive accuracy remains dependent on the specific formulation, grid resolution, and flow configuration. LES provides reliable reference solutions when conducted on a sufficient mesh but is computationally prohibitive at industrial Reynolds numbers, whereas wall-modeled LES and hybrid methods exhibit mixed performance, particularly for separation and reattachment. Moreover, differences in geometries, Reynolds numbers, grid strategies, and validation data across studies make direct, quantitative comparisons between turbulence models difficult. As a result, it remains unclear which hybrid approach offers the best compromise between accuracy, robustness, and computational cost for truck-like geometries under consistent conditions.

Despite the extensive body of work on simplified car geometries such as the Ahmed body and more realistic configurations such as DrivAer, comparatively fewer systematic studies exist for simplified truck configurations, and direct, model-consistent comparisons across multiple hybrid RANS–LES approaches remain limited. The present work aims to address this gap by performing a systematic comparison of several turbulence modeling strategies on the Allan body geometry. The investigated approaches will include multiple RANS models, DDES, IDDES, SRH, and hybrid methods combined with the γ–Re_θ transition model, as well as wall-resolved LES serving as a reference solution. Each approach will be assessed according to its ability to predict separation, reattachment, wake structure, surface pressure distributions, and drag under consistent numerical and modeling conditions. The most promising modeling strategies will then be applied to a full-scale truck configuration and validated against available wind-tunnel measurements, enabling an evaluation of both model fidelity and practical applicability for industrially relevant external aerodynamic flows.

4

Simplified Truck Model

This chapter presents the methodology and results for a simplified truck geometry used as a baseline case for assessing turbulence models. The objective is to evaluate the relative performance of several turbulence models under controlled wind tunnel conditions before extending the analysis to the fully detailed production truck in the next chapter. To ensure a fair comparison and consistency with Volvo Group's production workflow, the simulations follow standard external-aerodynamics CFD procedures in Siemens Simcenter STAR-CCM+. Since the purpose is to identify turbulence models suitable for production-truck simulations, the setup is based on Volvo truck best practices. All transient simulations were initialized from a precursor steady-state simulation of 2500 iterations, and a Large Eddy Simulation was performed on a high-resolution mesh to provide a baseline reference for the other models. The uncertainty in the simulated drag coefficient is reported using the 95% confidence interval introduced in section 2.1.2.2.2.

4.1 Simplified Truck Geometry

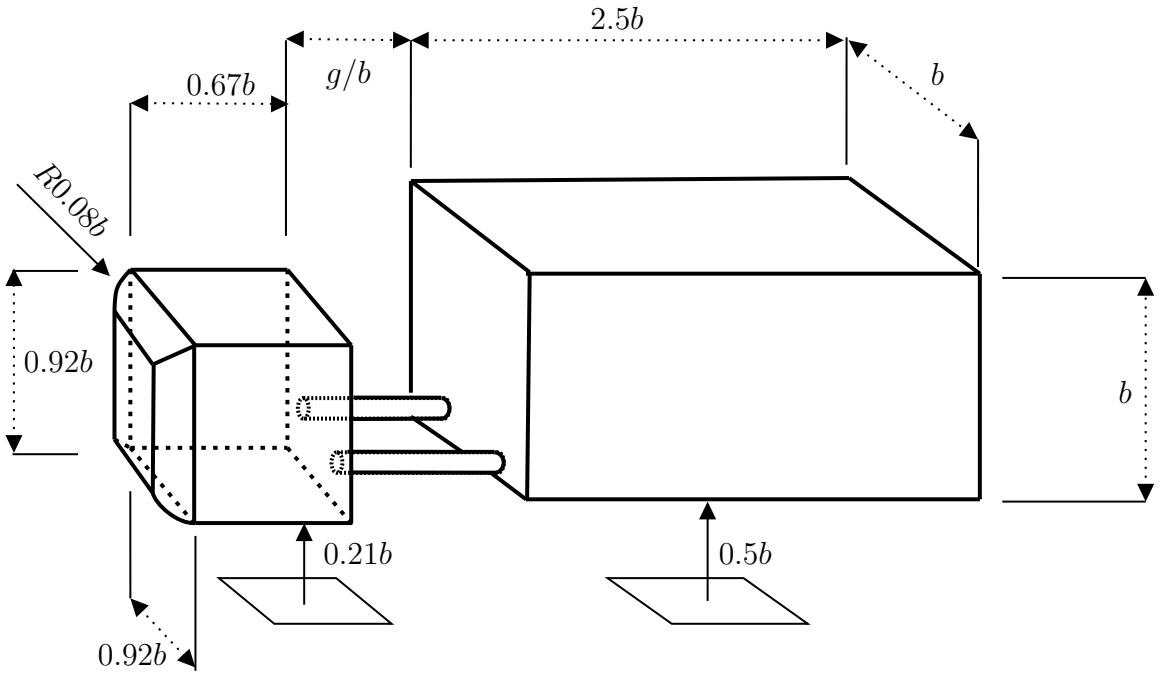

Figure 4.1: Two-box truck model developed by Allan [7], consisting of two rectangular boxes connected by two tubes of diameter $0.09b$ with a spacing of $0.713b$, and rounded corners of radius $0.08b$. All dimensions are given relative to the width of the rear box, b.

The simplified truck geometry used in this study was originally developed by J.W. Allan [7] to enable systematic investigations of generic tractor–trailer aerodynamics, with emphasis on the effects of bluff-body shape, ground clearance, and inter-unit spacing on drag and surface-pressure distributions. The model consists of two parametric square-based bodies representing the tractor and trailer, with either sharp or rounded front corners and an adjustable trailer gap. All dimensions are defined relative to the rear-box width b, as illustrated in Figure 4.1.

The present study uses $b = 0.305$ m, a trailer gap of $g = 0.5b$, and a rounded front-corner radius of $r = 0.08b$, chosen to better represent the aerodynamic behavior of a modern truck. The original experiments were performed in the 2.1 m $\times$ 1.7 m wind tunnel at the University of Southampton with a moving ground belt at 24.4 m/s, corresponding to $Re = 0.51 \times 10^6$. This geometry has since formed the basis for several numerical studies of turbulence modeling for truck aerodynamics [41, 42, 49].

4.1.1 Simulation Domain and Boundary Conditions

The computational domain was setup to match the domain used in LES simulations by Östh [41], which in turn was based on the original wind-tunnel geometry reported by Allan [7]. The domain size was defined relative to the characteristic body length b, resulting in overall dimensions of $32.7b \times 6.9b \times 5.6b$ in the streamwise (x), spanwise (y), and vertical (z) directions, respectively. The inlet plane was located $8b$ upstream of the model's leading edge.

The inlet was specified as a uniform velocity boundary condition at 24.4 m/s, and the outlet as a pressure outlet. The ground was modeled as a moving wall with a matching velocity to replicate the experimental moving-belt configuration, while the side walls and tunnel roof were treated as stationary no-slip walls. Since the configuration is based on a scaled wind-tunnel model, only partial dynamic similarity with a full-scale truck is achieved. The domain is illustrated in Figure 4.2.

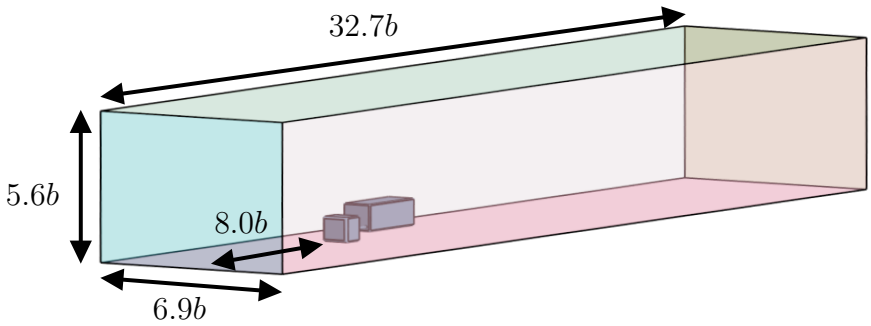

Figure 4.2: The computational domain used for the simplified models, $b = 0.305$ m.

4.2 Turbulence Models

Thirteen different simulation cases based on LES, DDES, SRH, and RANS models are presented. The RANS models were run as steady simulations, while the DDES, SRH, and LES cases were run transiently. With the exception of modifications to the Durbin scale limiter in both RANS models and the k-ω SST models, all turbulence models were run using standard settings. The DDES k-ω SST model is included because it represents the current

standard turbulence model used for aerodynamic simulations at Volvo. It therefore provides a relevant reference for comparison, particularly in terms of computational cost. Table 4.1 lists the tested turbulence models. The LES-mesh refers to a high-resolution mesh developed for the WR LES simulation. The differences between the standard mesh and the LES-mesh are discussed in the following section.

Model Type	**Description**
LES	WALE WR LES (WR LES mesh)
LES	WALE WM LES
DDES	DDES EB k-ε
DDES	DDES k-ω SST
DDES	IDDES k-ω SST
DDES	DDES k-ω SST with γ-Re_θ transition
DDES	IDDES k-ω SST with γ-Re_θ transition
SRH	SRH EB k-ε
SRH	SRH Lag EB k-ε
SRH	SRH k-ω SST
SRH	SRH k-ω SST with γ-Re_θ transition
RANS	RANS k-ε
RANS	RANS k-ω SST

Table 4.1: Turbulence models used in the study. The shaded row indicates the Volvo standard model used as the industrial reference.

4.3 Standard Computational Mesh

The simulations use two different meshes: a high-resolution mesh for the WR LES case and a standard computational mesh for the remaining RANS, WM LES, and hybrid models. The standard computational mesh was generated to approximate the resolution strategy used in Volvo Group's standard full-scale truck simulations. This was done by scaling the mesh size according to the geometric size difference between the simplified model and the full-scale truck, with the aim of obtaining a comparable overall cell count and a similar relative spatial distribution of refinement. Local refinement regions were introduced around the cab and trailer to resolve separation and wake structures corresponding to the refinement regions used for the full-scale truck.

The mesh consists of a trimmed hexahedral core with prism layers along all solid walls. The first-cell height was chosen so that the simulations follow a low-wall y^+ strategy, with the majority of first-cell values maintaining $y^+ \leq 1$. Local values up to $y^+ \simeq 2.5$ were observed primarily at the front corners of the cab and trailer, where the flow accelerates and is expected to remain attached, resulting in a locally thinner boundary layer. Four primary refinement levels with characteristic cell sizes of 1, 2, 4, and 8 mm were used. Additional refinement

boxes were applied along the tunnel walls, roof, and ground. The resulting size distribution is shown in Figure 4.3, where the refinement boxes are colored by cell size.

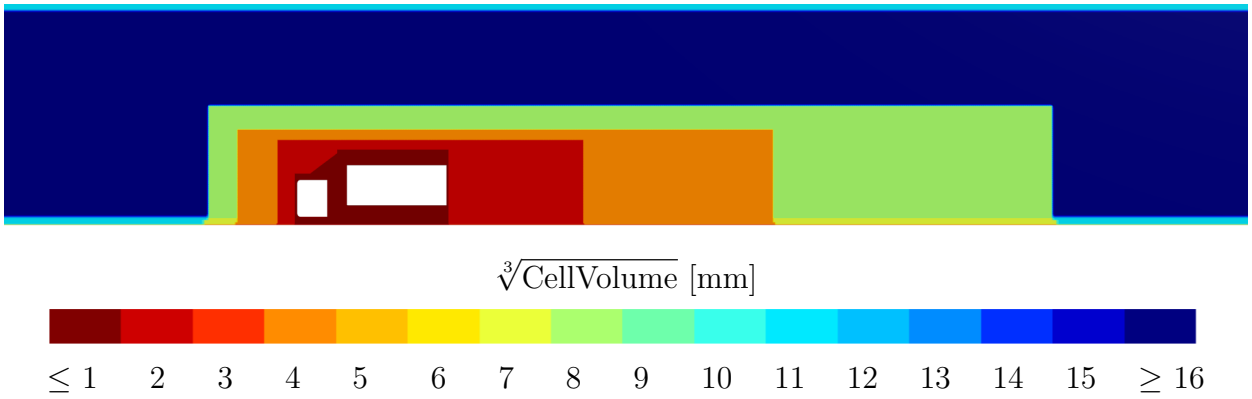

Figure 4.3: Cell size distribution of the computational mesh. Displayed calculating the cube root of the cell volume. The dark red, orange and green regions display the main refinement zones.

4.3.1 Computational Mesh for LES

A dedicated high-resolution mesh was generated for the WR LES simulation. In contrast to the standard mesh used for RANS, DES, and WM LES, this mesh was refined to better satisfy near-wall LES resolution requirements. A comparison between the two meshes is given in Table 4.2. Although the standard mesh provides sufficient wall-normal spacing for high-fidelity simulations, its streamwise and spanwise resolution are not adequate for a fully WR LES. Consequently, simulations using the WALE model on the standard mesh are here regarded the WM LES, whereas the refined mesh is used for WR LES. The WR LES setup was constrained by the available computational resources. It was executed on 5760 CPU cores for 137 hours, corresponding to an overall computational cost of approximately 790 kCPUh. Mesh size and runtime were selected to balance resolution requirements with feasible memory usage and turnaround time.

Table 4.2: Comparison between the standard and WR LES computational meshes.

Mesh Property	**Standard Mesh**	**WR LES Mesh**
Total cell count	0.46×10^9	1.1×10^9
Near-wall resolution (y^+)	≤ 2.5	≤ 1.5
Streamwise resolution (Δx^+)	< 160	< 40
Spanwise resolution (Δz^+)	< 160	< 40

The near-wall refinement of the WR LES mesh was defined using estimates of friction velocity and wall shear stress from an initial RANS simulation. The target wall-unit resolutions were

$$y^+ \leq 1.5, \qquad \Delta x^+ < 40, \qquad \Delta z^+ < 40, \tag{4.1}$$

where Δx^+ and Δz^+ denote the streamwise and spanwise grid spacings in wall units. The effect of this refinement is illustrated in Figure 4.4, which compares the standard and WR LES meshes at the trailer front corner.

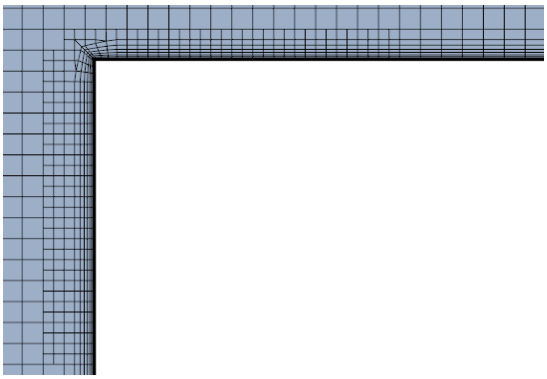

(a) Standard computational mesh at the trailer front corner. Lower near-wall Resolution.

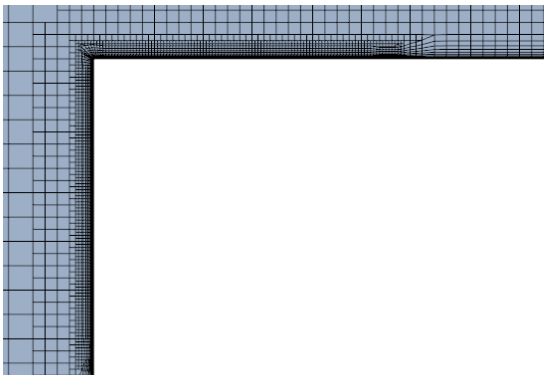

(b) Mesh for WR LES simulation at the trailer front corner. Higher near-wall resolution.

Figure 4.4: Cut plane of the computational meshes at $y = 0$ m, illustrating the difference in cell size and near-wall refinement between the standard and WR LES meshes. The corners are refined more strongly than the remaining surfaces due to the expected strong local flow gradients in these regions.

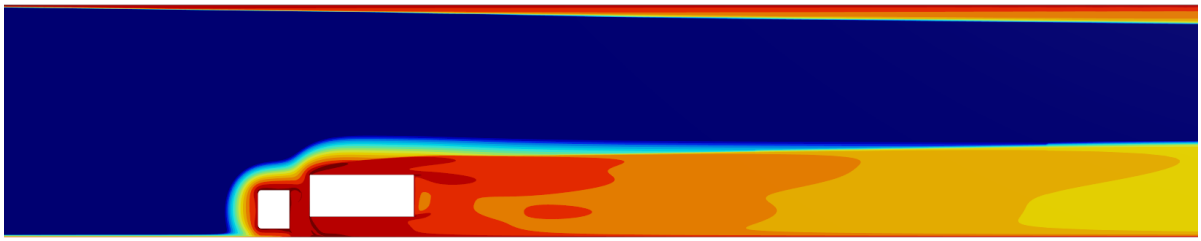

(a) Taylor microscale estimated from the initial RANS simulation.

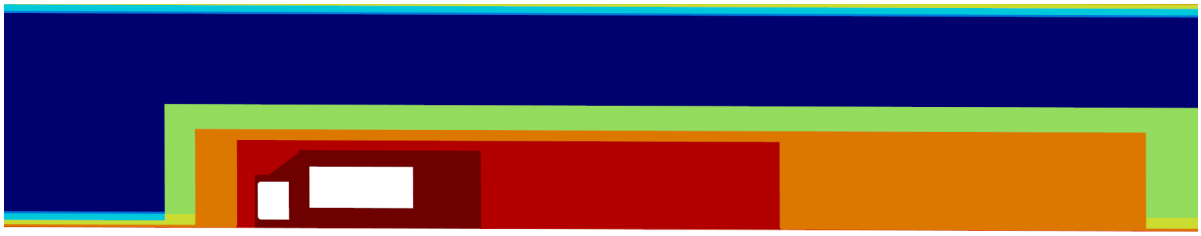

(b) Cell size distribution for the WR LES mesh, where the local cell size is calculated as $\sqrt[3]{\text{Cell Volume}}$.

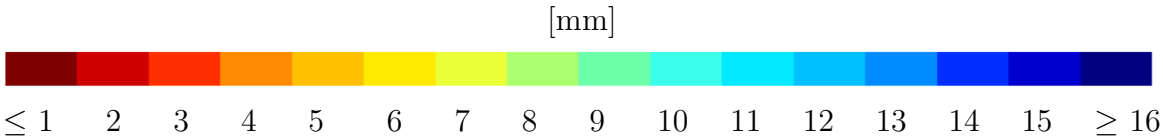

Figure 4.5: Comparison between the estimated Taylor microscale and the WR LES cell size distribution.

In addition to the near-wall refinement, volumetric refinements were applied to obtain a grid spacing on the order of the Taylor microscale. The Taylor microscale was estimated from the initial RANS solution following the recommendations in the STAR-CCM+ user manual [18]. The volumetric refinement and the estimated Taylor microscale are shown in Figure 4.5,

where the domain is colored by cell size and Taylor microscale, respectively. As discussed in Section 2.3.1, the Taylor microscale is an intermediate turbulence length scale between the inertial and dissipative subranges. Using it as a basis for volume refinement provides a mesh that is sufficiently fine to resolve the larger turbulence structures relevant to LES, while avoiding unnecessarily refinements that would move the resolution toward DNS-like requirements.

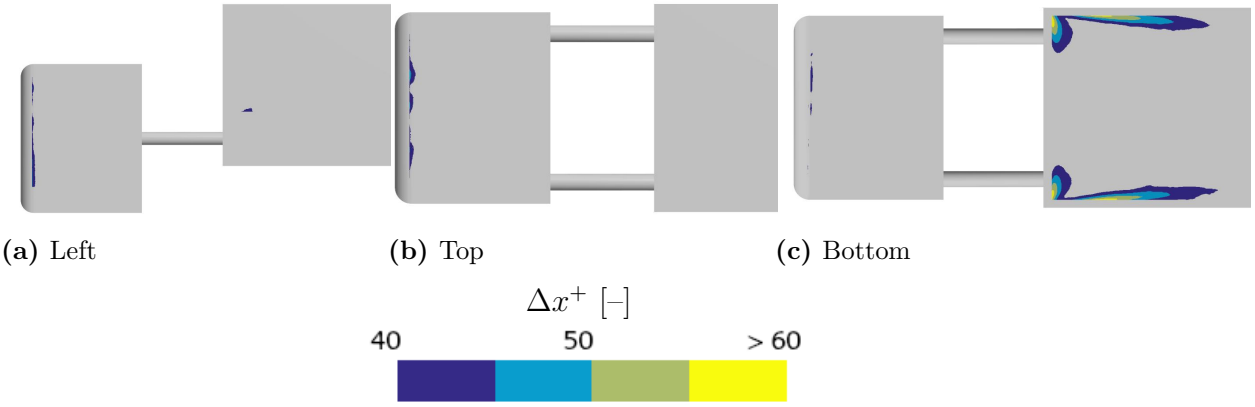

(a) Left **(b)** Top **(c)** Bottom

Figure 4.6: Local regions where the WR LES streamwise grid-spacing criterion is exceeded.

The final WR LES mesh consisted of approximately 1.1×10^9 cells. When the mesh was subsequently assessed using the WR LES solution, the time-averaged Δx^+ was found to exceed 40 locally in a few limited regions, as shown in Figure 4.6. These local exceedances occur because the wall shear stress, and therefore the friction velocity used to define wall units, differs somewhat from that predicted by the preliminary RANS simulation. Overall, however, the mesh provides adequate streamwise resolution and remains close to the recommended upper limit for spanwise spacing reported by Piomelli and Chasnov [34].

The boundary layers along the wind-tunnel walls were not resolved in the streamwise and spanwise directions. Instead, the default near-wall treatment provided by STAR-CCM+ was used, such that the wall behavior was handled through the WALE LES formulation rather than by explicitly resolving the wall boundary layers. This approach was considered sufficient, as the near-wall flow along the tunnel walls was assumed to be simple enough for the applied wall treatment to capture its main influence on the vehicle flow while limiting the computational cost.

4.4 Time Step Selection and Evaluation

Table 4.3: Cell share by CFL range for WM LES and WR LES meshes.

CFL range	WM LES (%)	WR LES (%)
$0 \leq \mathrm{CFL} < 1$	21.49	54.52
$1 \leq \mathrm{CFL} < 5$	77.26	38.96
$5 \leq \mathrm{CFL} < 20$	1.20	6.08
$\mathrm{CFL} \geq 20$	0.04	0.43

The hybrid RANS–LES and WM LES simulations were performed using a time step of $\Delta t = 1 \cdot 10^{-4}$ for a total simulated time of 6 s. Field-averaged quantities were computed over the final 4 s, after allowing 2 s for flow initialization. This time step led to a maximum CFL number of approximately 20, exceeded only in a few cells, as also shown in Table 4.3. This is within the range considered acceptable in the studies referenced in Section 3.4. A representative mean CFL number was defined as

$$\overline{\mathrm{CFL}} = \frac{\overline{|\mathbf{v}|}\Delta t}{V_{\mathrm{cell}}^{1/3}},$$

where $\overline{|\mathbf{v}|}$ is the time-averaged velocity magnitude and V_{cell} is the cell volume. Figures 4.7a and 4.7c show the mean $\overline{\mathrm{CFL}}$ distribution for the WM LES case. The violation of $\overline{\mathrm{CFL}} < 1$ is mainly concentrated near the truck model, particularly in the inner mesh refinement zones. Instances where $\overline{\mathrm{CFL}} > 5$ are generally found at the leading edges of the cab and trailer.

For the LES simulation, the time step was reduced by a factor of 2.5 to $\Delta t_{\mathrm{LES}} = 4 \cdot 10^{-5}$. The total simulation time was 5.4 s, of which the final 4.4 s were used for averaging after allowing 1 s for flow initialization. While this increased the proportion of cells with $\mathrm{CFL} < 1$, it also increased the share of cells with $\mathrm{CFL} \geq 5$, as summarized in Table 4.3. This is attributed to the significantly larger number of small cells in the near-wall regions. In Figures 4.7b and 4.7d, which show the mean $\overline{\mathrm{CFL}}$ distribution for the LES simulation, the majority of cells remain below $\overline{\mathrm{CFL}} < 5$. The regions exceeding $\overline{\mathrm{CFL}} \geq 5$ are shown in close-up in Figure 4.8 and are generally located at the leading corners of the cab and trailer. A smaller time step would reduce these values, but this was considered computationally infeasible.

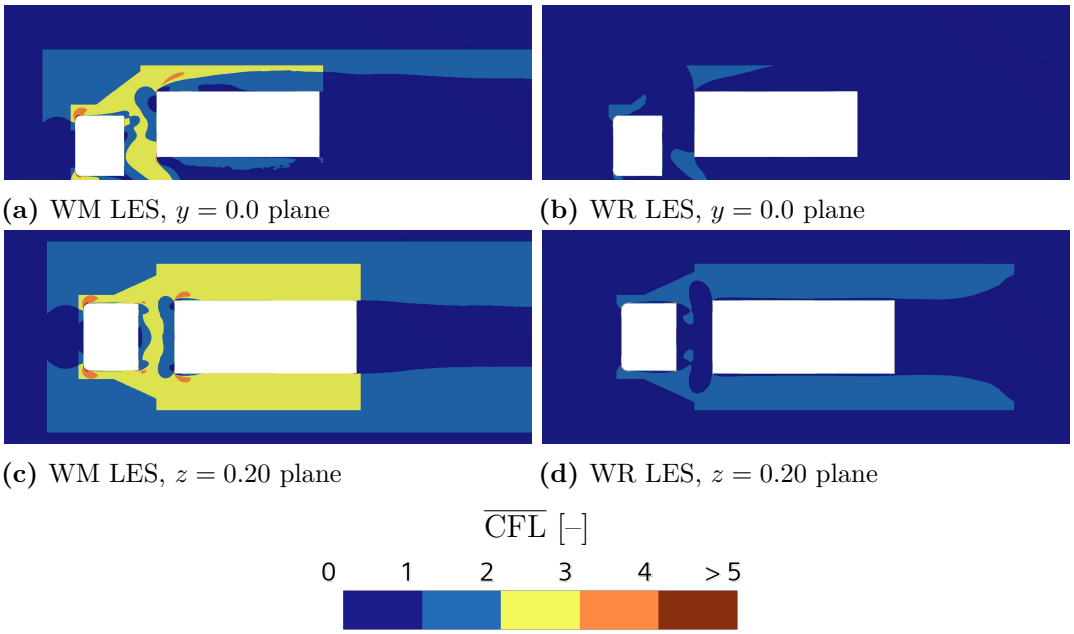

(a) WM LES, $y = 0.0$ plane **(b)** WR LES, $y = 0.0$ plane

(c) WM LES, $z = 0.20$ plane **(d)** WR LES, $z = 0.20$ plane

Figure 4.7: $\overline{\text{CFL}}$ in the symmetry plane $y = 0.0m$ (top two rows) and the top-view plane $z = 0.20$ m (bottom two rows).

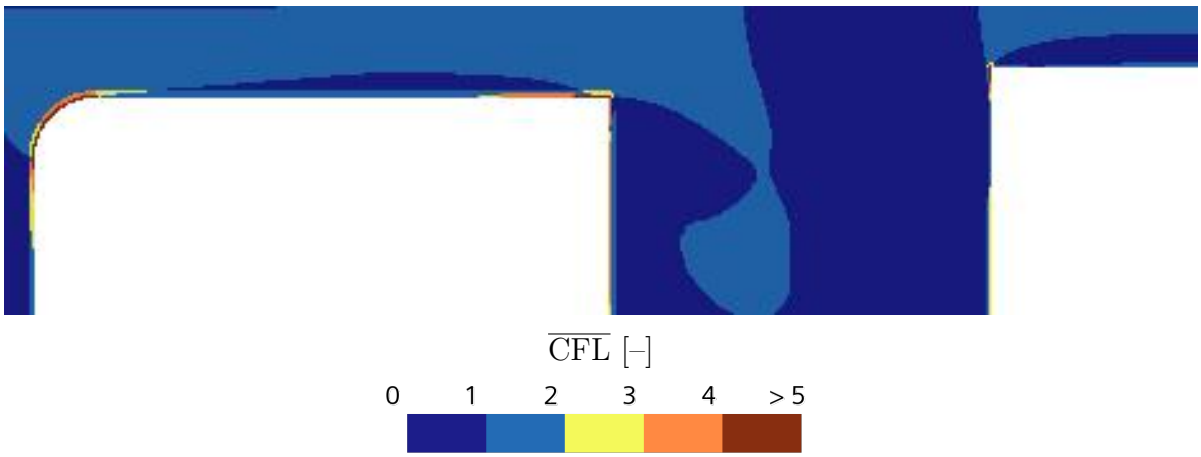

Figure 4.8: Close-up of the $\overline{\text{CFL}}$ number for the LES simulation at $z = 0.20$ m.

4.5 Results and Discussion

This section presents results from the turbulence-model simulations. Predicted drag coefficients are compared with experimental data and WR LES results. Differences in the resulting flow fields and key flow structures are then examined. The simplified-truck case is a scaled study at wind-tunnel Reynolds number. Therefore, the results represent model-scale rather than full-scale aerodynamics. Two coordinate systems are used in this section, η based on the cab centerline and a Cartesian system, as shown in Figure 4.9.

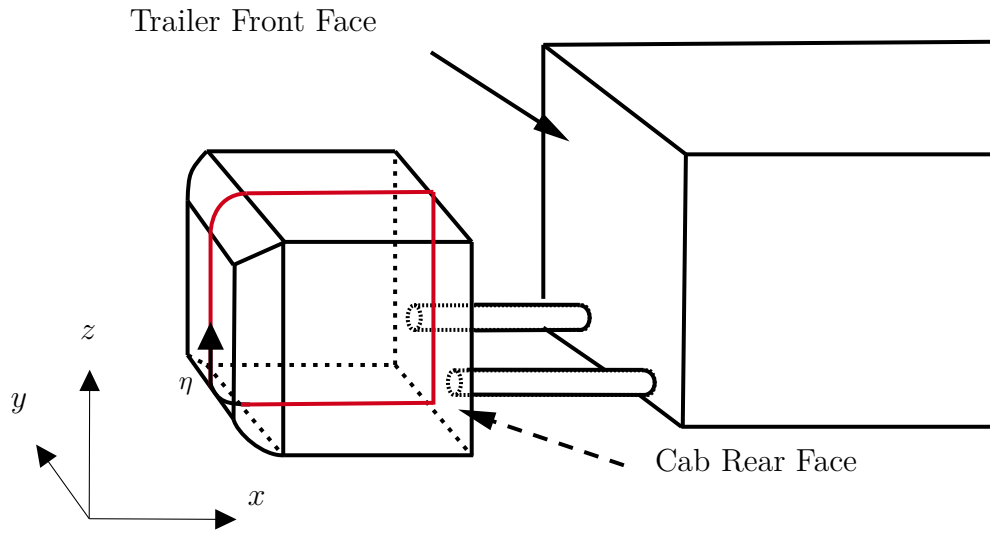

Figure 4.9: Placement of the main surfaces evaluated in the analysis. The coordinate η, shown as a red line, tracks the pressure coefficient clockwise from the bottom of the cab front face along the model centerline. The origin is at the cab-bottom plane, 0.244 m upstream of the model, with x in the streamwise direction and $y = 0$ at the symmetry plane.

4.5.1 Drag Prediction and Computational Cost

Table 4.4: Drag coefficient, error relative to benchmark data, and computational cost. Computational costs are normalized by the DDES k-ω case. γ-Re$_\theta$ denotes inclusion of the γ-Re$_\theta$ transition model. †Simulation did not complete; cost approximated.

Model	C_D	Δ vs WR LES	Δ vs Exp	Rel. Cost
Exp. [7]	1.22 ± 0.015	–	–	–
WR LES	1.213 ± 0.0042	–	0.007	2.62
LES				
WALE WM LES	1.174	0.039	0.046	0.65
DDES				
DDES k-ω	1.105	0.108	0.115	1.00
DDES k-ω LES Mesh	1.105	0.108	0.115	1.92
IDDES k-ω	1.128	0.085	0.092	0.86
DDES EB k-ε	1.184	0.029	0.036	1.38
DDES k-ω + γ-Re$_\theta$	1.098	0.115	0.122	1.12†
IDDES k-ω + γ-Re$_\theta$	1.090	0.123	0.130	1.72
SRH				
SRH EB k-ε	1.096	0.117	0.124	1.25
SRH Lag EB k-ε	1.096	0.117	0.124	1.27
SRH k-ω	1.080	0.133	0.140	0.75
SRH k-ω + γ-Re$_\theta$	1.105	0.108	0.115	0.72
RANS				
k-ε	1.209	0.004	0.011	0.04
k-ε LES Mesh	1.208	0.005	0.012	0.07
k-ω	1.183	0.030	0.037	0.04

The drag coefficients and relative computational costs, normalized by the DDES k-ω SST case, are listed in Table 4.4. The results are compared with the wind-tunnel measurements reported by Allan [7] and with the WR LES solution. A key distinction between the simulations is the predicted separation mode over the cab. The LES and RANS cases generally predict attached flow over the cab, whereas most SRH and DES-type cases predict separation from the cab leading edges. This difference in separation behavior has a clear impact on the drag prediction, with the separated-cab mode generally producing lower drag.

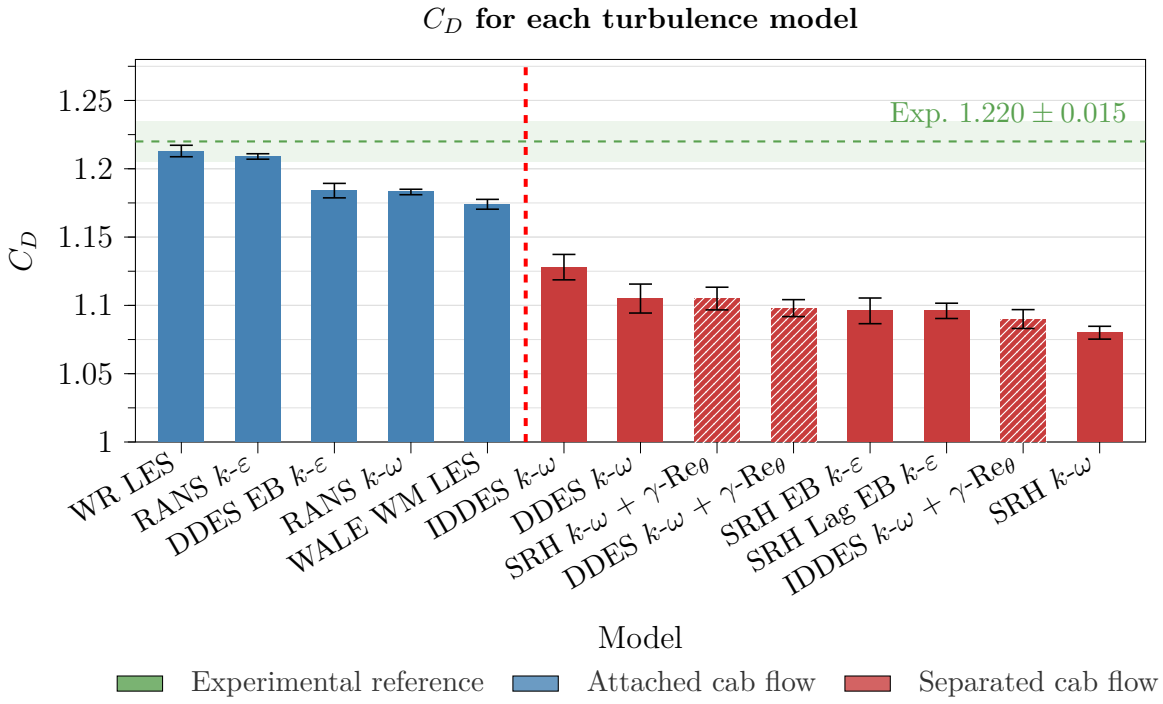

Figure 4.10: Drag coefficient C_D for each turbulence model, ranked in descending order. Blue bars indicate attached cab flow; red bars indicate detached cab flow (separated by the dashed vertical line). Striped bars denote activation of the γ-Re$_\theta$ transition model. Error bars show the 95% confidence interval. The green dashed line and shaded band mark the experimental reference 1.220 ± 0.015. The C_D axis is truncated at 1.00.

The ranking is summarized in Figure 4.10, which highlights the clear drag separation between models predicting attached and detached cab flow. Models predicting attached flow cluster in the upper drag range ($C_D > 1.17$), while those predicting detached flow fall below $C_D = 1.13$, with no overlap between the two groups even when accounting for the 95% confidence intervals. Among all simulations, the WR LES gives the closest agreement with experiment, yielding $C_D = 1.213 \pm 0.0042$, which lies within the experimental uncertainty band of 1.22 ± 0.015. It therefore provides a suitable high-fidelity reference, although at the highest computational cost, 2.62 times that of the baseline DDES case. The WALE WM LES offers the best compromise between accuracy and cost, predicting $C_D = 1.174$ at a relative cost of 0.65. Among the steady RANS cases, the k-ε model shows the best agreement with both LES and experiment, while exhibiting little grid sensitivity, as reflected by the similar drag coefficient obtained on the LES mesh. The k-ω RANS case predicts somewhat lower drag but still remains closer to the attached-cab LES behavior than most hybrid approaches.

Among the hybrid methods, DDES EB k-ε is the only case that reproduces the same separation

mode as the LES simulations, leading to the best drag prediction within this group, $C_D = 1.184$. The DDES k-ω SST and IDDES k-ω cases instead predict more extensive cab leading-edge separation and consequently lower drag, with further deterioration for the transition-model variants. A similar trend is observed for the SRH-based models, which generally produce the lowest drag values and the largest deviations from experiment. The inclusion of the γ-Re_θ transition model does not consistently improve the results, although it increases the drag prediction somewhat for SRH k-ω. Overall, the results indicate that accurate drag prediction for this case depends strongly on reproducing the LES-like attached-flow separation mode over the cab, while additional model complexity does not necessarily improve either accuracy or cost efficiency.

4.5.2 Wall-Resolved LES

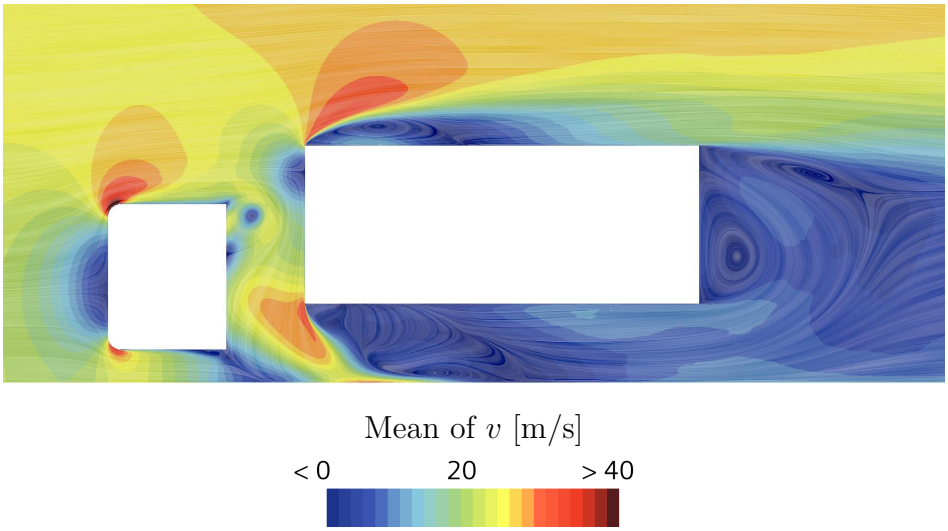

Figure 4.11: Average velocity magnitude in the plane $y = 0.0$ m.

As noted in the previous section, the WR LES simulation predicts the most accurate C_D compared with the wind-tunnel reference. Its velocity field in the plane $y = 0.0$ is shown in Figure 4.11. The flow over the cab is characterized by minor detachment at the front radius. After separating, the flow reattaches on top of the cab and then separates again at the rear. In the gap between the cab and trailer, the flow forms several vortices: a horseshoe vortex at the top of the cab, marked by the red ellipse in Figure 4.12a, and two additional vortices extending downward into the large under-trailer wake, marked by the red ellipse in Figure 4.12b. The under-trailer wake extends far to the sides of the trailer, as visible from the top view in Figure 4.12a, and reaches all the way to the base wake at the trailer rear. In addition, large-scale separation occurs at the leading edges of the trailer top and sides. In the velocity field shown in Figure 4.11, recirculation patterns can be observed both in the separation region at the trailer front edges and in the large base wake.

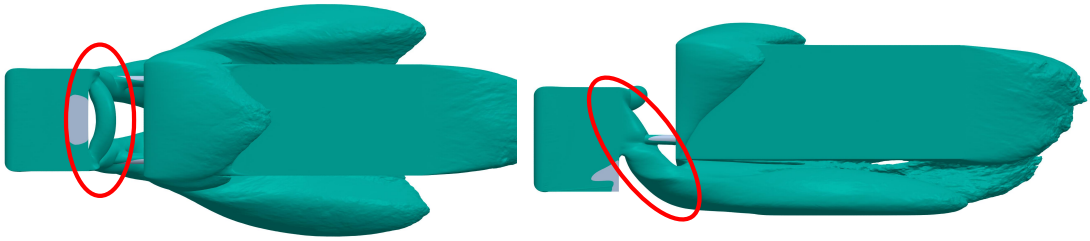

(a) Top view: Horseshoe vortex marked

(b) Side view: Cab-trailer wake vortices marked

Figure 4.12: Iso surfaces of separation where $C_{p,tot} = 0$.

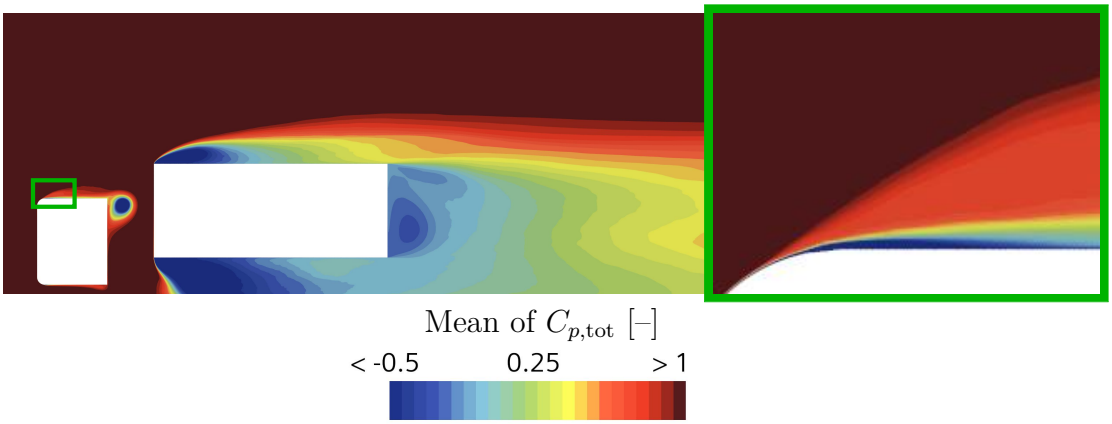

Figure 4.13: Total pressure coefficient $C_{p,\text{tot}}$ in the $y = 0.0$ plane, zoom at cab leading edge.

The total pressure coefficient, $C_{p,\text{tot}}$, in the plane $y = 0.0$, shown in Figure 4.13, highlights regions of total pressure loss associated with separation and wake structures. A close-up of the cab leading edge also shows the minor cab separation followed by rapid reattachment, as noted above. This slight separation is visible when looking at the skin friction coefficient, in Figure 4.14, where the coefficient becomes zero in a small band after the cab leading radii. The predicted separation and reattachment on the cab are consistent with the pattern reported by Allan [7].

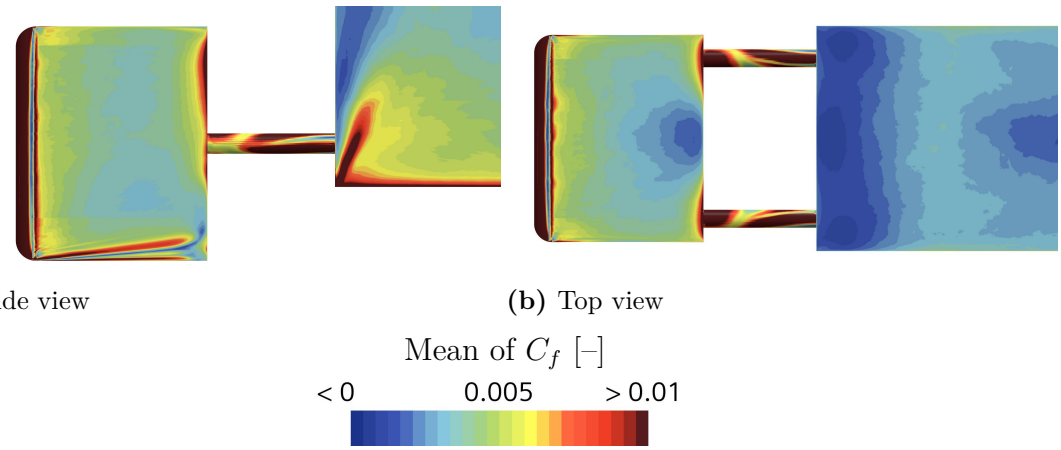

(a) Side view

(b) Top view

Figure 4.14: Mean of skin friction coefficient seen from the left and top sides.

Allan [7] also reports pressure measurements on the cab rear face and the trailer front face. These data fields are compared with the corresponding WR LES results in Figures 4.16b and 4.15b. On the trailer front face, the LES agrees well with the experiment in Figure 4.15c, reproducing the high-pressure region near the top and capturing a similar location of the high-to-low pressure gradient across the remainder of the surface. On the cab rear face, the agreement with experiment in Figure 4.16c is weaker. The LES predicts higher pressure in the high-pressure regions and shows two extended low-pressure bands originating near the mid-left and mid-right portions of the face which extend toward the top, resulting in stronger overall pressure gradients than indicated by the measurements. This discrepancy should be interpreted in light of the experimental setup, since the pressure-probe coverage is limited and does not extend fully to the outer edges of the face [7].

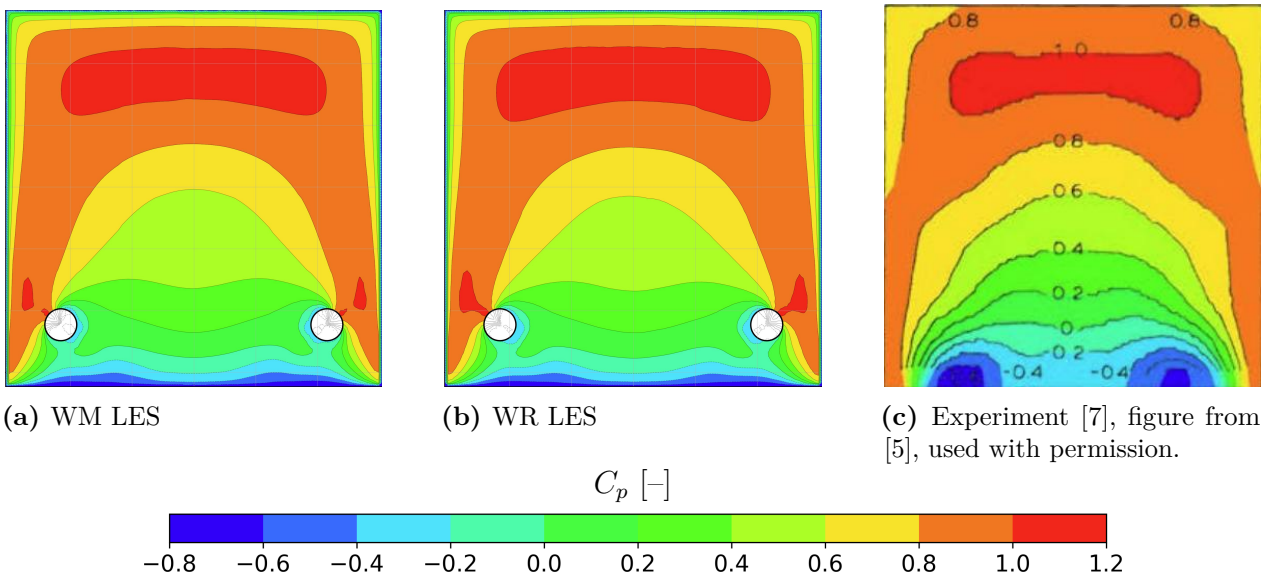

(a) WM LES **(b)** WR LES **(c)** Experiment [7], figure from [5], used with permission.

Figure 4.15: Pressure coefficient, C_p, measured on the trailer front face. The white region marks the connector between the trailer and the cab, where no surface data are available.

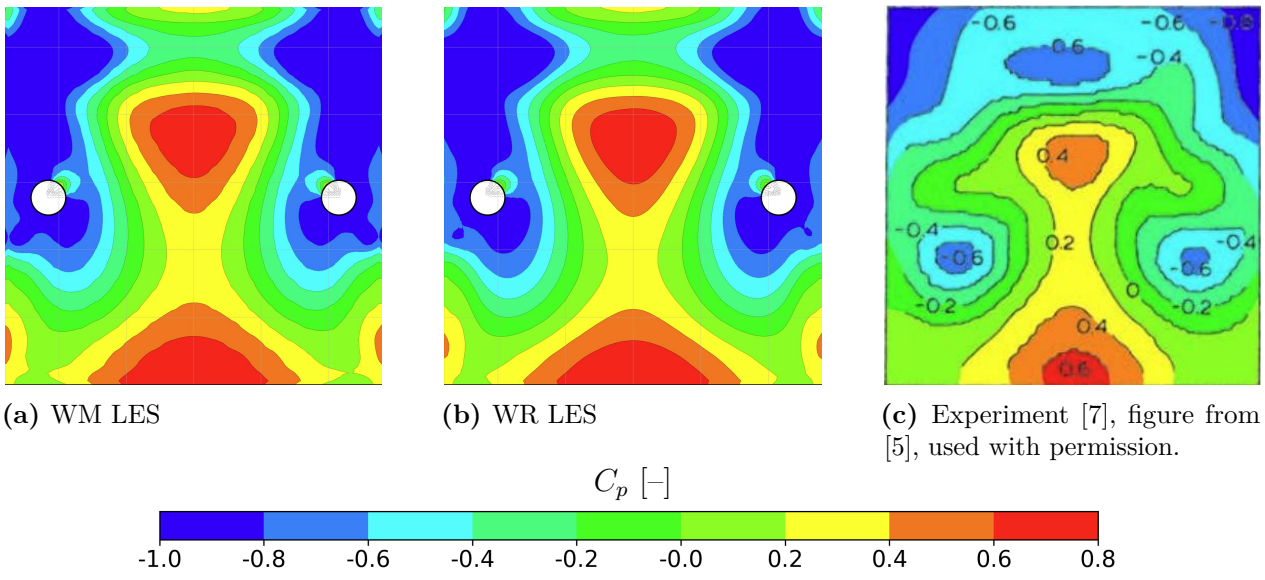

(a) WM LES **(b)** WR LES **(c)** Experiment [7], figure from [5], used with permission.

Figure 4.16: Pressure coefficient, C_p, measured on the cab rear face. The white region marks the connector between the trailer and the cab, where no surface data is available.

4.5.3 Wall-Modeled LES

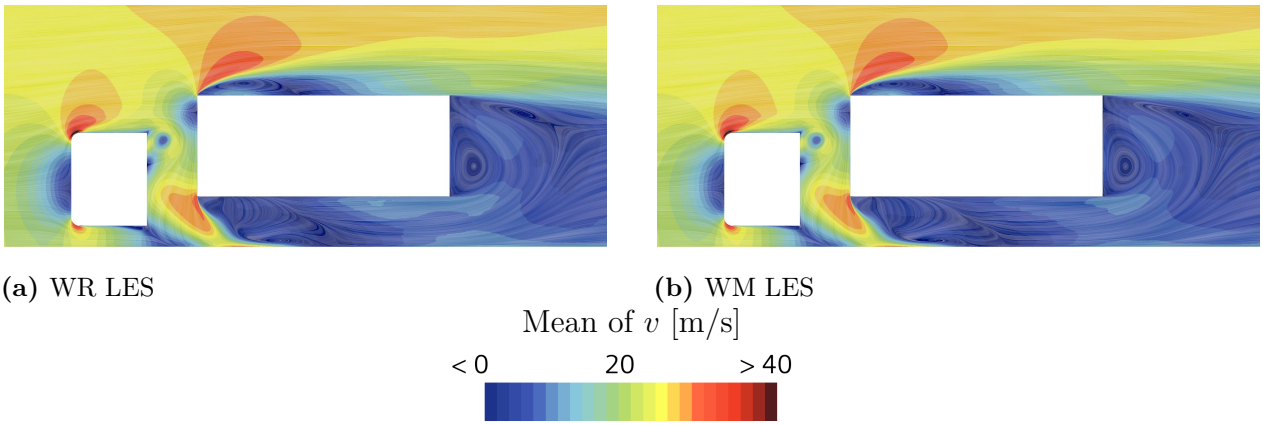

(a) WR LES **(b)** WM LES

Figure 4.17: Averaged velocity magnitude in the plane $y = 0.0$ m.

Overall, the WM LES simulation reproduces the main mean-flow features observed in the WR LES simulation. The primary separation topology is captured around both the cab and trailer. The flow structures and recirculations in the cab-trailer gap and trailer wake show broadly similar positions and extents. These similarities are apparent when comparing the velocity fields of the WM LES and WR LES in Figures 4.17a and 4.17b. Despite the use of the standard mesh described in Section 4.3, the WM LES therefore provides a comparable prediction of the dominant flow features.

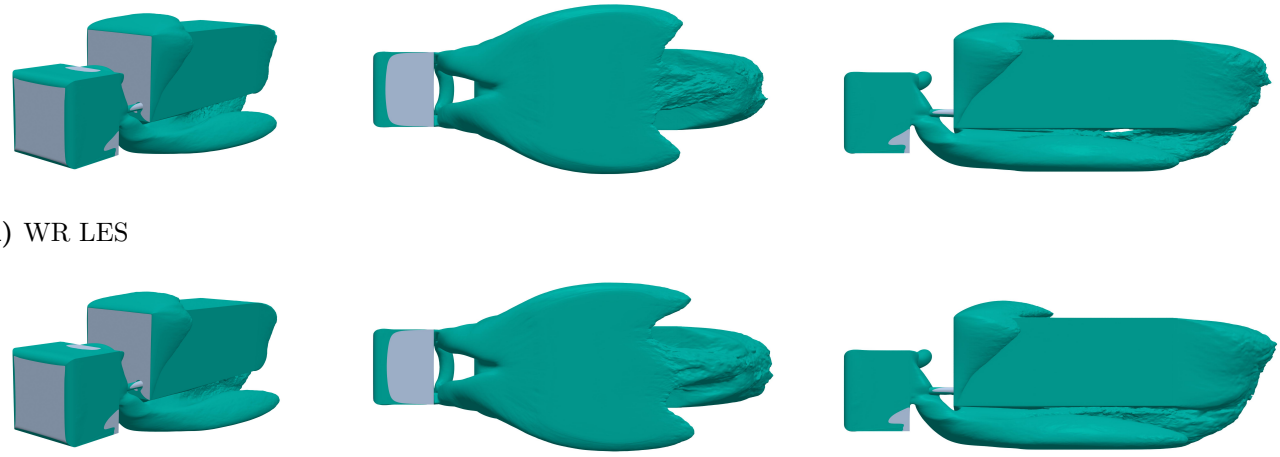

(a) WR LES

(b) WM LES

Figure 4.18: Iso-surfaces of separation, defined by $C_{p,\text{tot}} = 0$, for the WR LES (top row) and WM LES (bottom row). Left column: isometric view; center column: bottom view; right column: left-side view.

The main differences between the WM LES and WR LES appear in the separation topology, particularly beneath and behind the trailer. Compared with the WR LES in Figure 4.18a, the WM LES in Figure 4.18b predicts a narrower under-trailer wake with sharper trailing features, while the rear wake extends slightly farther downstream. Additional differences are also observed at the cab leading edge, where the WM LES predicts a somewhat larger separated region. This is illustrated in the zoomed-in $C_{p,\mathrm{tot}}$ plots at the cab leading edge for the WM LES in Figure 4.19b and the WR LES in Figure 4.19a. The difference in cab separation is also present in the skin-friction distribution in Figure 4.20, which for WR LES in Figure 4.14 is more diffuse and does not show as sharp a reduction toward zero at the cab front radii. A likely explanation for this diffusion is the reduced near-wall resolution in the WM LES, where wall functions replace the resolved near-wall turbulence.

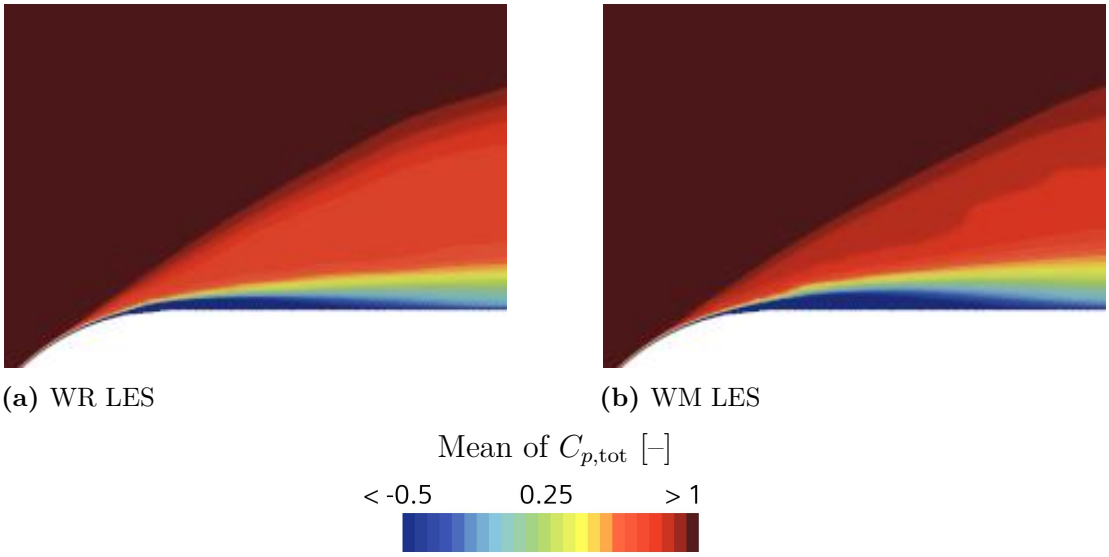

(a) WR LES **(b)** WM LES

Figure 4.19: Total pressure coefficient $C_{p,tot}$ plots at the top of the cab front face radius for the WR LES (left) and WM LES (right) at $y = 0.0$ m.

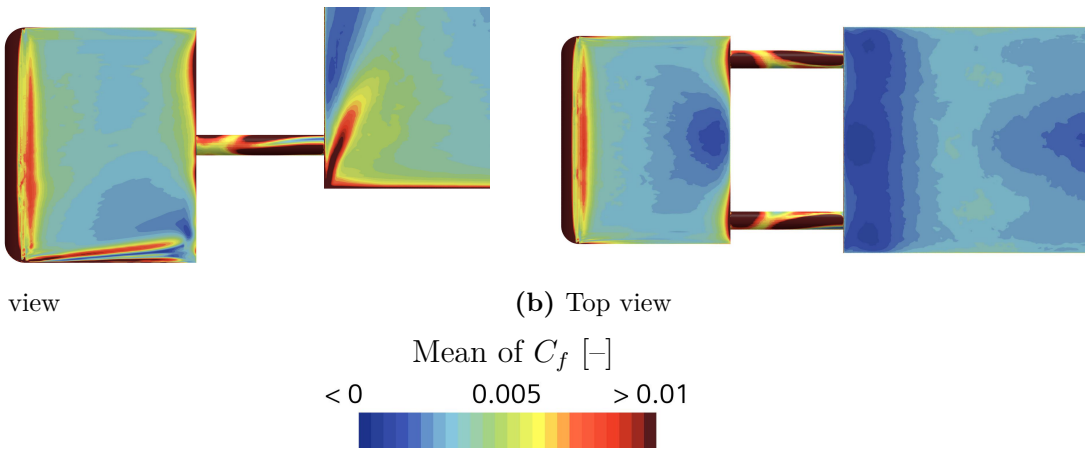

(a) Side view **(b)** Top view

Figure 4.20: Mean of skin friction coefficient seen from the left and top sides for the WM LES.

The differences in resolved turbulence are also evident in the Q-criterion iso-surfaces at $Q = 1 \cdot 10^6\,\mathrm{s}^{-2}$. The WR LES in Figure 4.21a exhibits a significantly denser field of vortical structures at this threshold, including many smaller-scale features that are largely filtered out

in the WM LES in Figure 4.21b. This indicates that the WR LES resolves a broader range of turbulent scales, particularly in the near-wall regions, whereas the WM LES primarily captures the larger structures consistent with its coarser grid and wall modeling. Consequently, the WR LES is expected to provide a more detailed representation of the near-wall dynamics, while the WM LES offers a reduced resolution that is a more computationally efficient description of the turbulent structures.

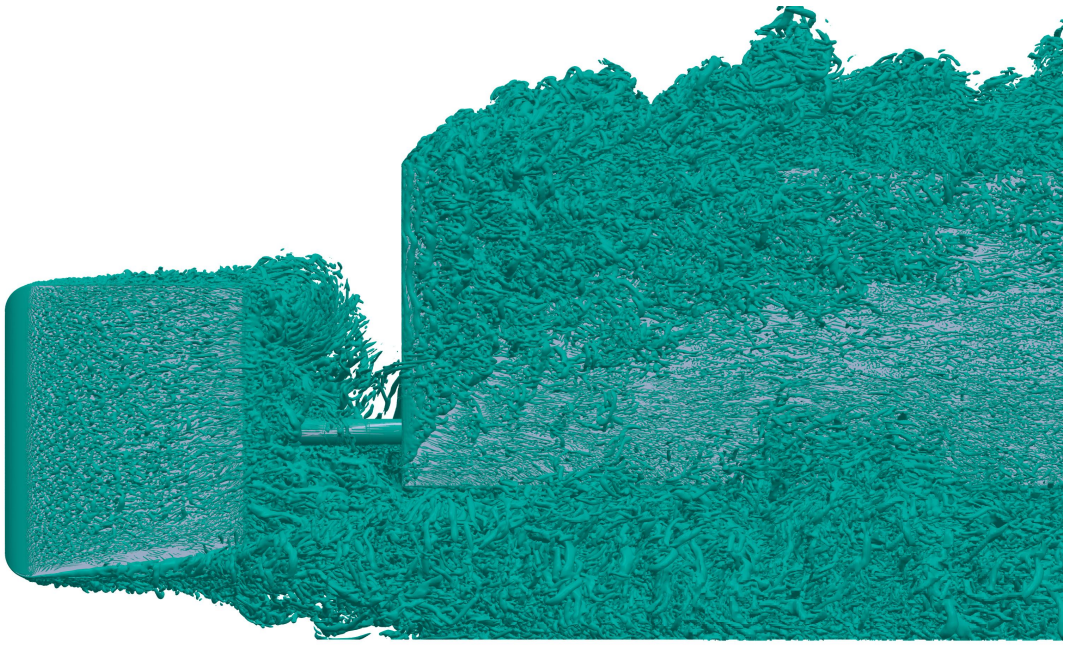

(a) WR LES

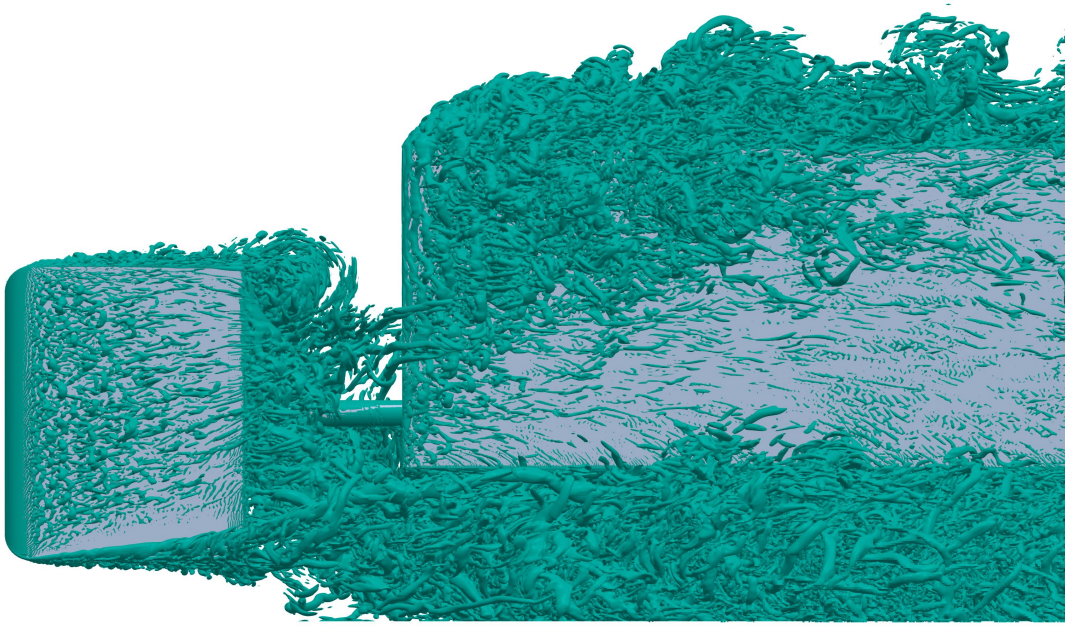

(b) WM LES

Figure 4.21: Instantaneous iso-surfaces of turbulent structures ($Q = 1 \cdot 10^6 \quad s^{-2}$) for the WR LES (top) and WM LES (bottom).

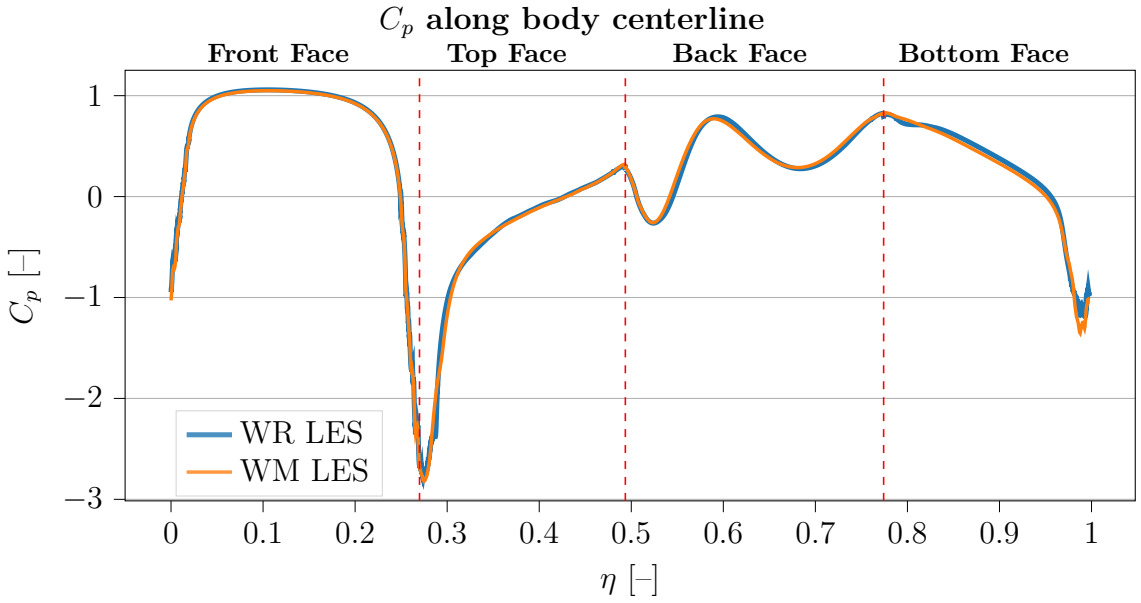

Figure 4.22: Pressure plot along the centerline of the cab. The centerline starts at the bottom of the front face and wraps clockwise around the cab. The plot is partitioned into corresponding pressures on each face.

The pressure along the symmetry centerline of the cab in the $y = 0.0$ plane, using the η coordinate introduced in Figure 4.9, is shown in Figure 4.22. The line starts at the bottom of the front face and wraps clockwise around the whole cab. The pressure distribution for the WM LES closely matches the pressure distribution of the WR LES simulation. The main differences are seen on the top and bottom face where the WM LES curve is more de-featured pointing to similar diffusion of gradients, due to grid resolution, as seen in the skin friction plots.

The WM LES underpredicts the drag relative to the WR LES result, yielding $C_D = 1.174$ compared with 1.213, which corresponds to a reduction of approximately 3.2%. Overall, the WM LES provides a computationally inexpensive prediction while capturing the mean separation behavior reasonably well. However, the increased resolution of the WR LES improves agreement with the experimental drag and allows a larger fraction of the turbulence to be resolved.

4.5.4 DDES and IDDES Models

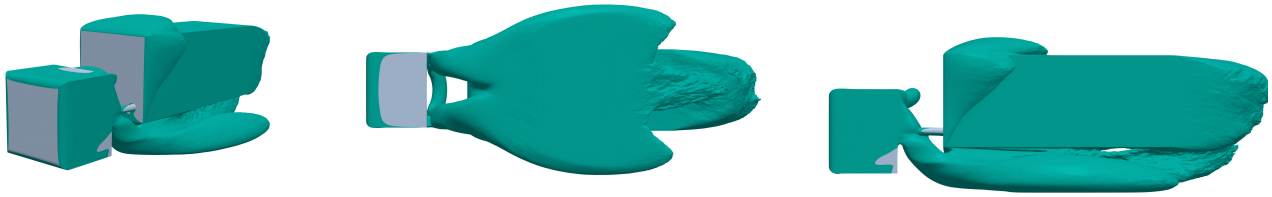

(a) WR LES

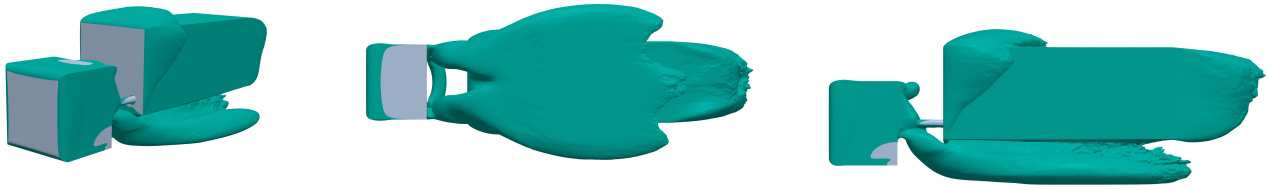

(b) DDES EB k-ε

(c) DDES k-ω SST

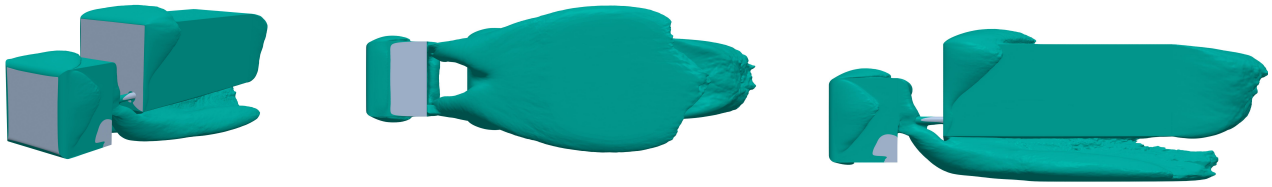

(d) IDDES k-ω SST

Figure 4.23: Iso-surfaces of separation where $C_{p,\text{tot}} = 0$. Left column: isometric view; center column: bottom view; right column: left-side view.

Relative to the WR LES reference, the DDES EB $k-\varepsilon$ model shows the closest qualitative agreement, whereas the DDES and IDDES k-ω models predict a different separation mode. As previously stated in Section 4.5.2, in the WR LES case shown in Figure 4.23a, the flow remains largely attached over the cab, while the dominant separation structures occur in the cab–trailer gap, at the trailer leading edges, in the underbody region, and in the rear wake. The DDES EB k-ε model in Figure 4.23b reproduces this topology relatively well, showing similarly attached flow over the cab and capturing the horseshoe vortex in the cab–trailer gap. In addition, the vortex pair originating from the cab rear and extending into the underbody wake is also present, although the vortices are smaller, which is likely linked to the reduced under-trailer separation. The separation patterns over the trailer and in the rear wake remain broadly similar, although slightly larger separation is also observed along the trailer sides.

Overall, this more confined underbody flow is consistent with the underprediction of C_D by the DDES EB model.

By contrast, the DDES and IDDES k-ω SST solutions in Figures 4.23c and 4.23d predict substantially larger separation over the roof and sides of the cab. Rather than forming the distinct horseshoe vortex observed behind the cab in the WR LES case, these models exhibit more pronounced separation at the cab rear. Although vortical structures still extend into the underbody region, they are less pronounced than in the WR LES. At the same time, both models predict reduced separation over the trailer top and side surfaces, as well as a smaller underbody wake. Relative to the WR LES solution, separation is therefore shifted from the trailer and underbody regions toward the cab. This indicates that the near-wall behavior of the hybrid formulations strongly influences the global separation pattern.

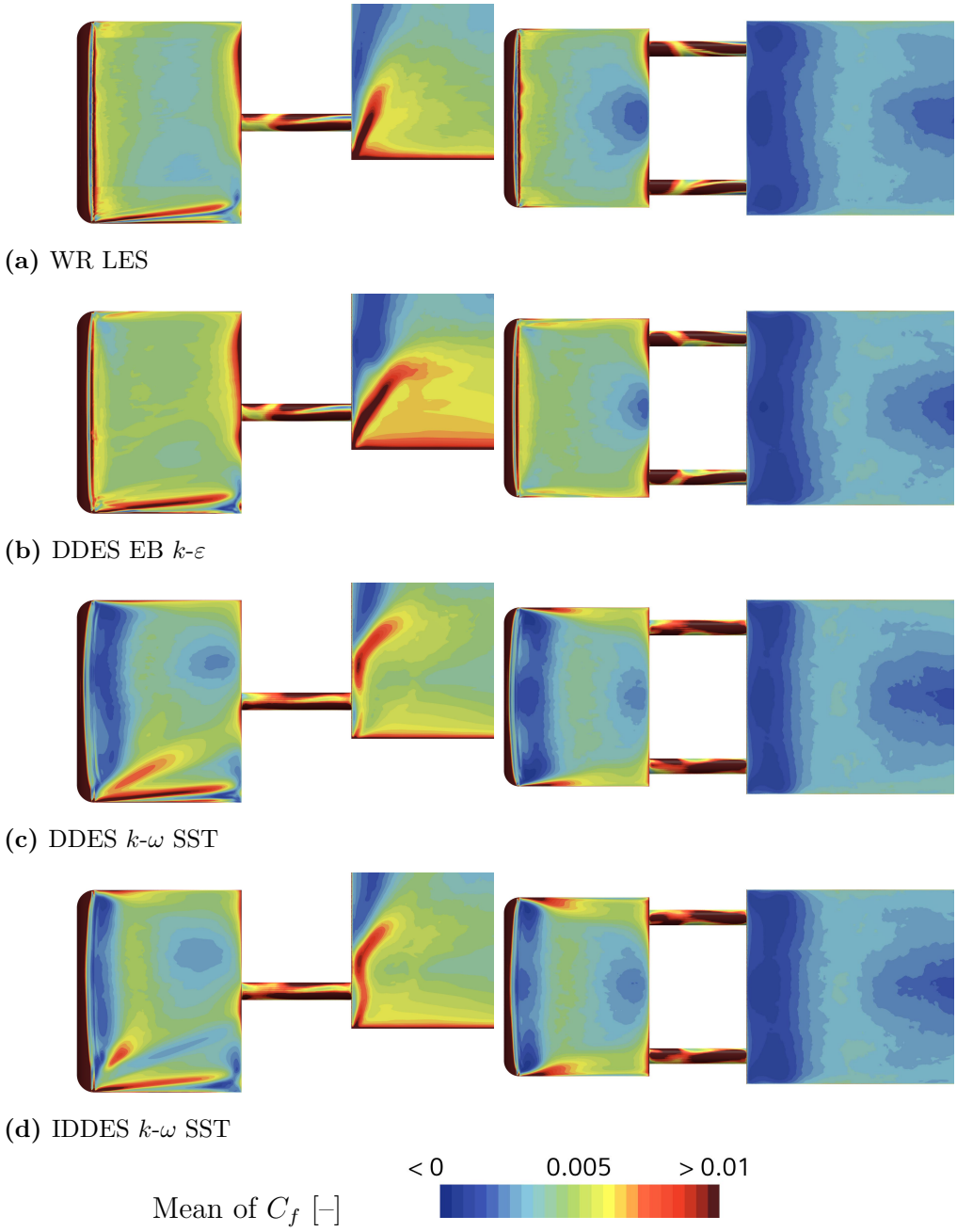

(a) WR LES

(b) DDES EB k-ε

(c) DDES k-ω SST

(d) IDDES k-ω SST

Figure 4.24: Mean skin-friction coefficient viewed from the left and top sides.

For the DDES and IDDES k-ω models, separation is consistently initiated at the cab leading radius, as indicated by a rapid reduction in the skin-friction coefficient C_f in Figures 4.24c and 4.24d. Compared with DDES, IDDES predicts smaller separation regions, identified by smaller low-C_f zones after the initial separation. The weaker separation at the cab is followed by increased separation downstream at the trailer, suggesting that IDDES partly redistributes separation from the cab to the trailer. The skin-friction distribution for DDES EB in Figure 4.24b is broadly similar in topology to that of the WR LES in Figure 4.24a. At the cab leading radius, both models indicate separations at similar locations. On the trailer however, especially in the side view, DDES EB exhibits a somewhat larger low-C_f region, consistent with the larger separation seen in Figure 4.23b.

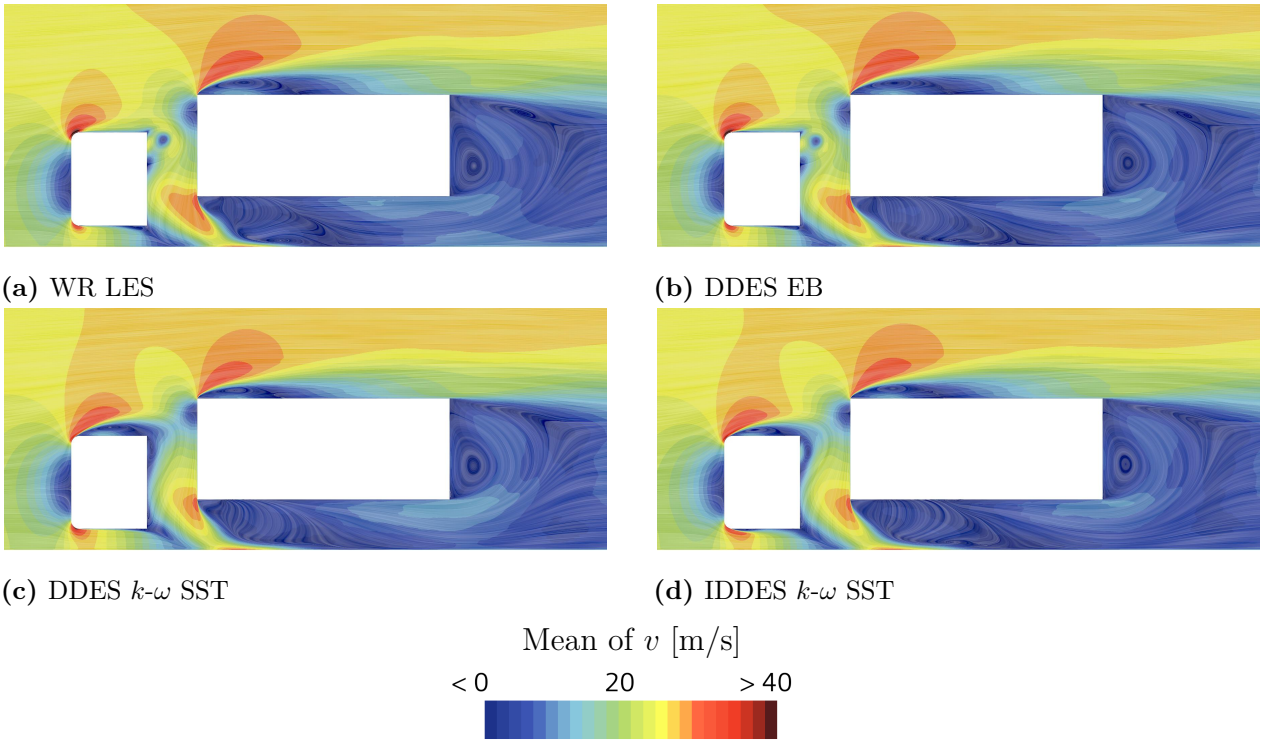

(a) WR LES

(b) DDES EB

(c) DDES k-ω SST

(d) IDDES k-ω SST

Figure 4.25: Average velocity magnitude displayed with line integral convolution in the plane $y = 0.0$ m.

The velocity field plots confirm the same two separation modes identified from the separation and skin-friction results, as shown in Figure 4.25. WR LES and DDES EB, shown in Figures 4.25a and 4.25b, retain largely attached flow over the cab and develop distinct vortex structures downstream of the cab roof. Main differences are confined to the under-trailer region, where the separation patterns vary. By comparison, the DDES and IDDES k-ω SST cases, shown in Figures 4.25c and 4.25d, separate over the top and rear of the cab, producing a broader low-velocity region and suppressing the distinct free-standing vortex core seen in the other models. The velocity fields around the trailer further highlight the comparatively smaller separation for these cases.

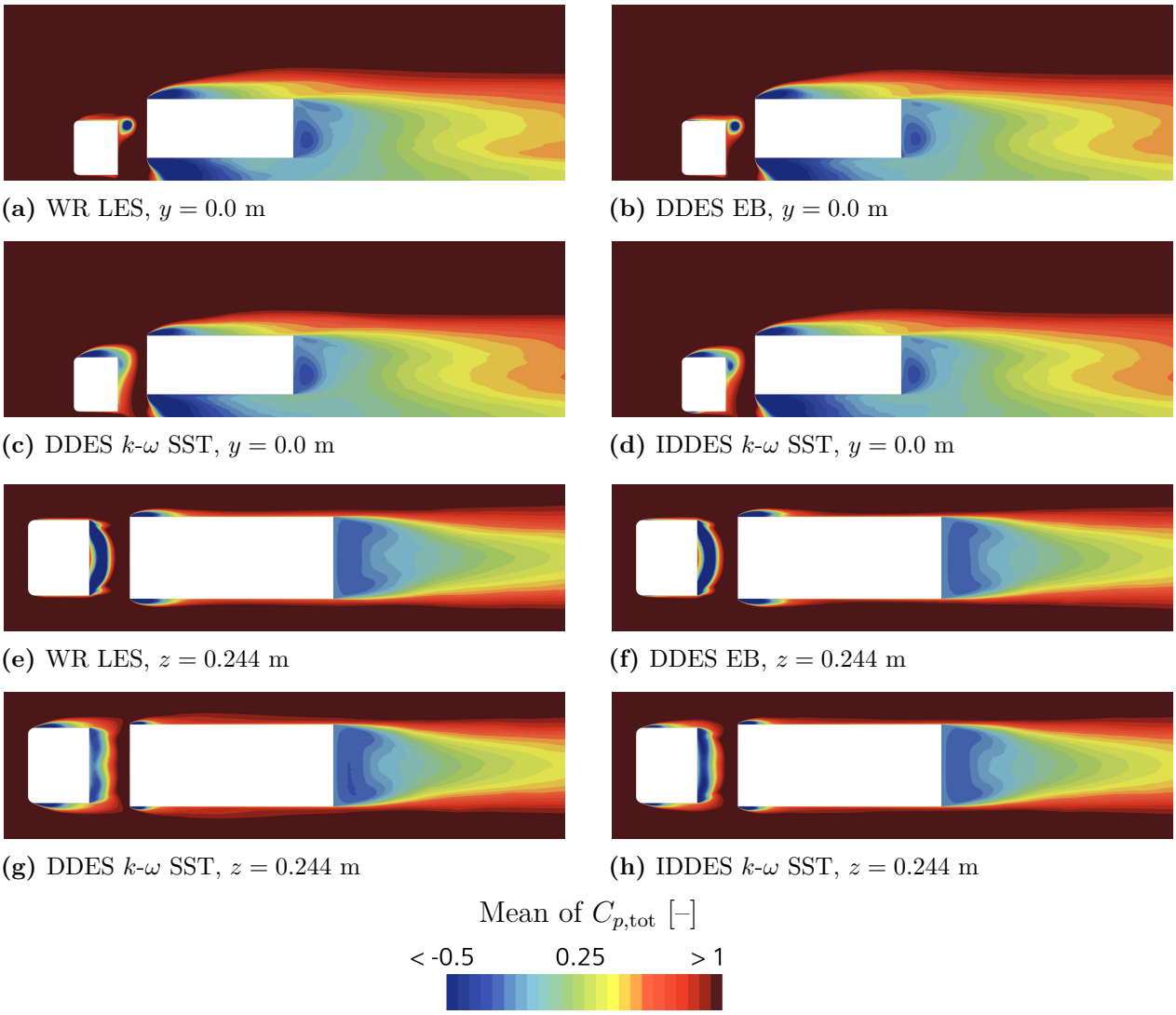

(a) WR LES, $y = 0.0$ m

(b) DDES EB, $y = 0.0$ m

(c) DDES k-ω SST, $y = 0.0$ m

(d) IDDES k-ω SST, $y = 0.0$ m

(e) WR LES, $z = 0.244$ m

(f) DDES EB, $z = 0.244$ m

(g) DDES k-ω SST, $z = 0.244$ m

(h) IDDES k-ω SST, $z = 0.244$ m

Figure 4.26: Averaged total pressure coefficient in the symmetry plane $y = 0.0$ m (top two rows) and the top-view plane $z = 0.244$ m (bottom two rows).

Total-pressure losses associated with separation are illustrated by the $C_{p,\mathrm{tot}}$ distributions in the symmetry plane $y = 0.0$ m. The largest model-to-model differences are linked to the predicted separation mode and occur primarily in the cab region. For the WR LES and DDES EB cases, shown in Figures 4.26a and 4.26b, the strongest losses in the cab region appear to be associated with the previously identified horseshoe vortex. In contrast, for the DDES and IDDES k-ω SST cases in Figures 4.26c and 4.26d, the losses are instead associated with the separated region above and behind the cab.

Further insight is gained from the top-view plane at $z = 0.244$ m in Figures Figures 4.26e–4.26h. The influence of the vortex in the cab–trailer gap is more evident for the WR LES and DDES EB cases in Figures 4.26e and 4.26f, where the loss region appears more concentrated around the vortex core. The greater losses near the trailer sides are also consistent with the higher C_D values predicted for these cases compared with the other models. For the separated-flow cases, DDES and IDDES k-ω SST in Figures 4.26g and 4.26h, the loss region begins earlier over the cab roof and continues into the inter-vehicle gap. These losses appear more diffuse and locally weaker in comparison, and together with the smaller separation along the trailer

sides, this helps explain the lower drag coefficients predicted by these models.

The comparison with experimental pressure measurements provides an additional basis for assessing the hybrid models beyond their agreement with the WR LES reference. On the trailer front face, shown in Figure 4.27, all hybrid models show generally good agreement with the measurements and reproduce similar overall pressure distributions. The DDES EB result in Figure 4.27c shows the closest agreement, as it captures a continuous high-pressure region similar to that observed in the experiment. In contrast, the DDES and IDDES models in Figures 4.27a and 4.27b confine the higher-pressure region more to the upper part of the face, without extending it as far downward along the sides.

On the cab rear face, the agreement with the experimental pressure distribution is poorer for all hybrid models. The DDES and IDDES results in Figures 4.28a and 4.28b fail to reproduce the low-pressure regions observed in the upper corners of the measured field. In contrast, the DDES EB result in Figure 4.28c captures these low-pressure zones, but overpredicts their extent. At the same time, DDES EB reproduces the high-pressure region slightly above the centerline more accurately than the other hybrid models. Taken together, the pressure comparisons suggest that DDES EB provides the most consistently accurate overall prediction among the hybrid models, particularly due to its closer agreement on the trailer front face and its somewhat better representation of the main pressure features on the cab rear face.

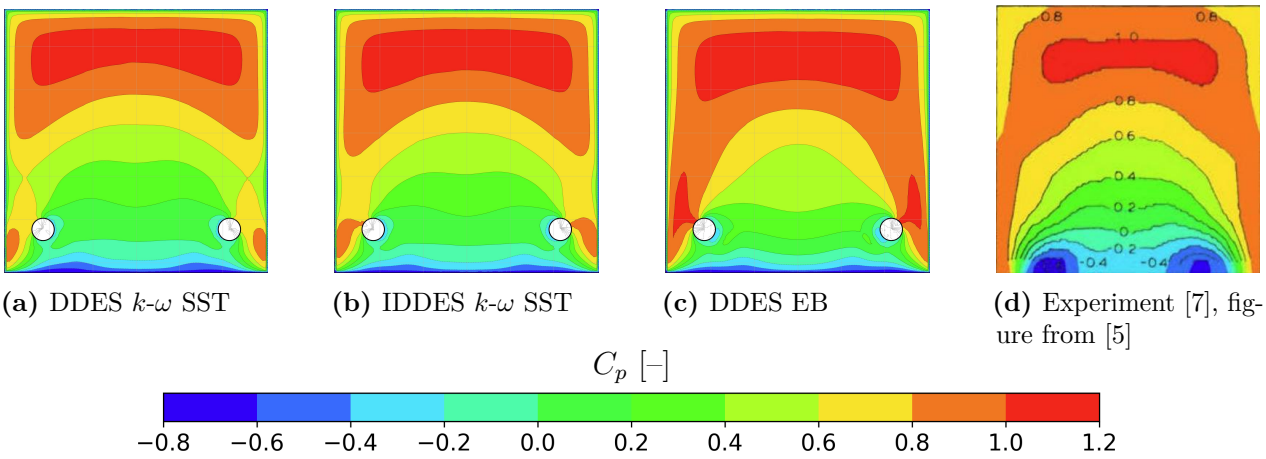

(a) DDES k-ω SST **(b)** IDDES k-ω SST **(c)** DDES EB **(d)** Experiment [7], figure from [5]

Figure 4.27: Pressure coefficient, C_p, on the trailer front face.

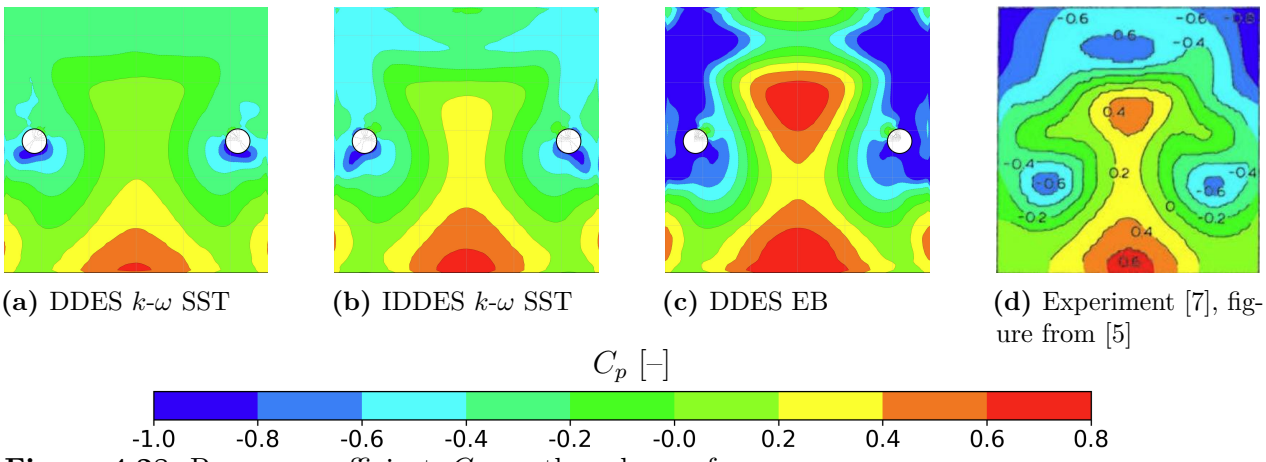

(a) DDES k-ω SST **(b)** IDDES k-ω SST **(c)** DDES EB **(d)** Experiment [7], figure from [5]

Figure 4.28: Pressure coefficient, C_p, on the cab rear face.

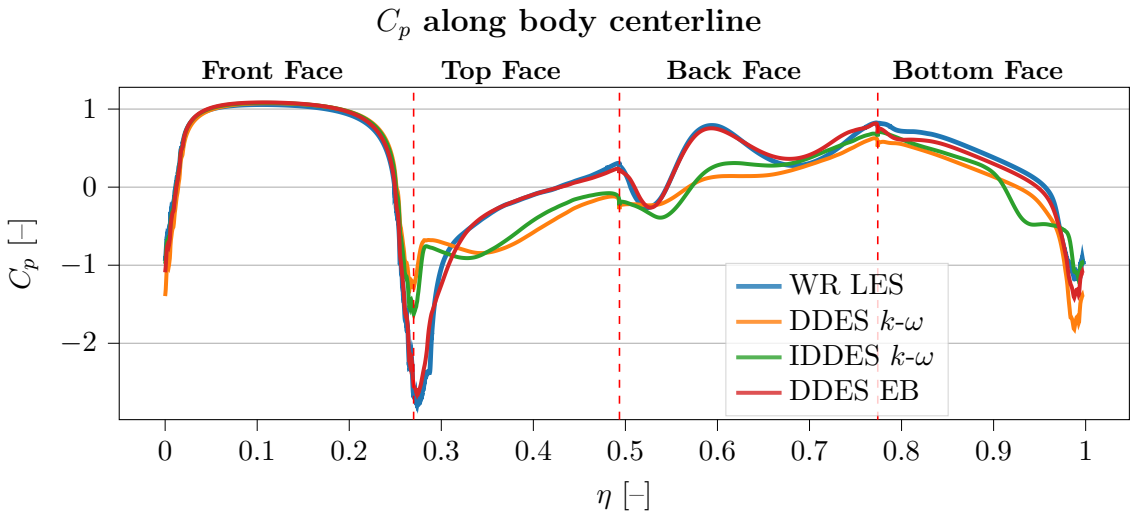

Figure 4.29: Pressure distribution along the centerline of the cab. The centerline starts at the bottom of the front face and wraps clockwise around the cab. The plot is partitioned into the corresponding pressures on each face.

The centerline pressure distribution around the cab in Figure 4.29 confirms the trends already observed in the separation, velocity, and pressure fields. As illustrated in Figure 4.9, the line wraps around the cab from the front face to the roof. The DDES and IDDES models deviate from the WR LES primarily at the transition between the front face and the roof, consistent with the earlier onset of separation in this region. By comparison, the DDES EB model remains closest to the WR LES solution, although its pressure distribution is slightly smoother and still shows some deviations near the bottom face.

To assess the sensitivity of the DDES k-ω SST solution, and to determine whether the observed separation behavior was primarily caused by the mesh or by the Durbin scale limiter, a limited side study was performed. Restoring the Durbin scale limiter to its standard value increased the overall extent of separation, but did not alter the qualitative separation topology: the main separation locations and reattachment behavior remained unchanged. This indicates that, for the present setup, the limiter primarily affects the magnitude of separation rather than the underlying separation mode.

Additional exploratory mesh variations were tested, including mesh coarsening and changes to the prism-layer height and number of prism layers, in order to reduce the risk of premature transition from RANS to LES mode within the boundary layer. None of the tested variations produced attached flow over the cab. This also applied to a DDES k-ω simulation on the LES mesh, which yielded the same mean drag coefficient as the baseline DDES case but with smaller statistical uncertainty, indicating that further grid refinement did not improve the prediction and mainly increased the computational cost. Since these tests were limited in scope and were not the main focus of the study, they should not be interpreted as a complete optimization of the hybrid-model setup. Within the range of settings examined here, the results therefore suggest that the separated-cab mode persists, although further work is required to determine whether alternative hybrid-model settings could recover a more LES-like separation behavior.

4.5.5 SRH Models

Relative to the WR LES reference, all SRH variants predict a separation topology that is closer to the DDES k-ω SST solutions. Rather than recovering the largely attached cab flow of the WR LES, the SRH models reproduce the same general separated-flow mode previously observed for the k-ω-based DDES and IDDES models.

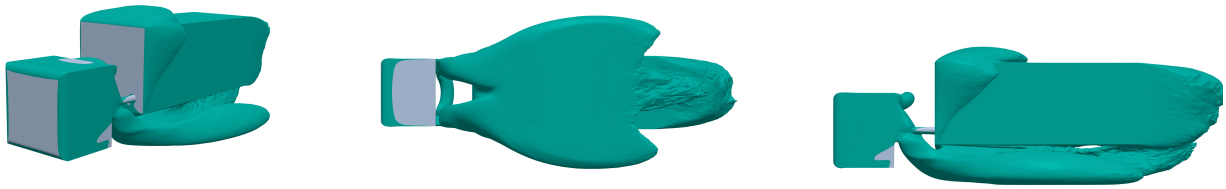

(a) WR LES

(b) DDES k-ω SST

(c) SRH k-ω SST

(d) SRH EB

(e) SRH lag EB

Figure 4.30: Iso-surfaces of separation where $C_{p,\mathrm{tot}} = 0$. Left column: isometric view; center column: bottom view; right column: left-side view.

Differences within the SRH family are modest, as shown in Figure 4.30. The SRH k-ω SST,

SRH EB, and SRH lag EB variants in Figures 4.30c, 4.30d, and 4.30e all produce broadly similar global separation topologies. Compared with the WR LES case in Figure 4.30a, they all overpredict separation on the cab, while the under-trailer wake appears slightly narrower than in the corresponding DDES solution in figure 4.30b. The main internal difference is that the EB-based variants also predict a small separated region on the bottom of the cab, which makes them somewhat closer to the IDDES-type behavior than to the standard DDES k-ω SST solution.

Since the predicted flow fields are similar across the SRH variants, the main distinction between them is their computational cost. In the present configuration, the EB-based SRH variants do not show a clear advantage, as they produce flow fields similar to the DDES k-ω SST solutions while requiring approximately 125% of the DDES computational cost. By contrast, the SRH k-ω SST model provides a similar level of agreement at roughly 25% lower cost, making it the most attractive SRH variant among those tested here.

4.5.6 Transition Modeling

The effect of the γ-Re_θ transition model was investigated for the selected k-ω SST hybrid RANS-LES approaches. Overall, inclusion of the transition model increased cab separation in the DDES, IDDES, and SRH cases. As a result, the predicted flow fields deviated further from the attached cab-flow behavior observed in the WR LES. For the DDES case, this increase in separation is evident from the greater height of the separation bubble in the $C_{p,\text{tot}}$ distribution when the transition model is included. This difference in separation height is illustrated by the horizontal line in Figure 4.31, which highlights that the separated region is larger in the transition-model case. A similar trend was observed for IDDES. Because the transition model increased the computational cost of the simulations, it was not investigated further.

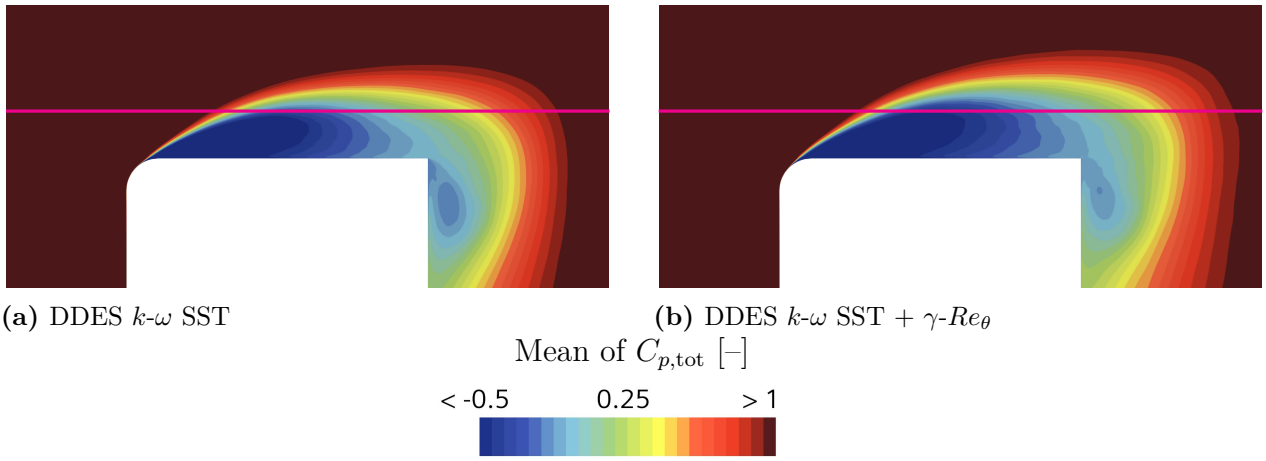

(a) DDES k-ω SST

(b) DDES k-ω SST + γ-Re_θ

Figure 4.31: Averaged total pressure coefficient in the plane $y = 0.0$ m.

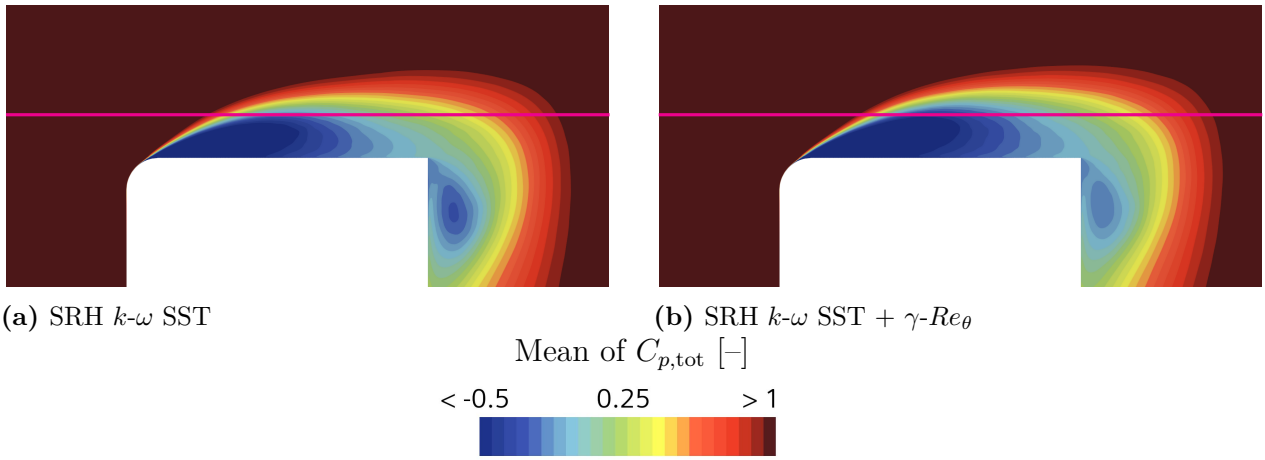

(a) SRH k-ω SST **(b)** SRH k-ω SST + γ-Re_θ

Figure 4.32: Averaged total pressure coefficient in the plane $y = 0.0$ m.

Including the transition model in the SRH k-ω SST simulation produced a similar increase in separation to that observed for the DDES k-ω case. Figure 4.32 shows that the SRH case with the transition model also exhibits increased separation, as indicated by the horizontal line. In this case, however, the resulting flow field becomes more similar to that of the DDES k-ω SST model, which is evident from the under-trailer separation shown in Figure 4.33. The underbody wake structure, in particular, more closely resembles the DDES solution, with a slightly wider wake. This wider wake is consistent with the increase in drag coefficient C_D observed when the γ-Re_θ model is included. Thus, while the transition model is not beneficial for the DDES and IDDES k-ω SST cases, it appears to be more advantageous for the SRH k-ω SST model in the present configuration. The resulting flow field and drag level become similar to those of the DDES k-ω SST model, but at a lower computational cost of approximately 72% of the DDES cost.

(a) SRH k-ω **(b)** SRH k-ω γ-Re_θ **(c)** DDES k-ω SST

Figure 4.33: Iso-surfaces of separation where $C_{p,\mathrm{tot}} = 0$. All columns show bottom view.

4.5.7 RANS Models

Two steady RANS simulations, using the k-ε and k-ω turbulence models, were performed on the standard mesh. These simulations were used to assess how well steady-state solutions reproduce the drag, separation structures, and total-pressure losses predicted by the WR LES. Figure 4.34 shows that both RANS simulations reproduce the attached flow over the cab, as well as the vortical structures in the cab-trailer gap. The vortices extending toward the underside of the trailer are also present and are of similar size.

Further downstream, however, the differences become more pronounced. Compared with the WR LES, both RANS models predict trailer-top separation extending further downstream.

The under-trailer wake is also wider and narrows into sharper trailing tips. Thus, while the steady RANS approaches capture the overall flow topology around the cab, they do not reproduce the downstream separated-flow structures as accurately.

(a) WR LES

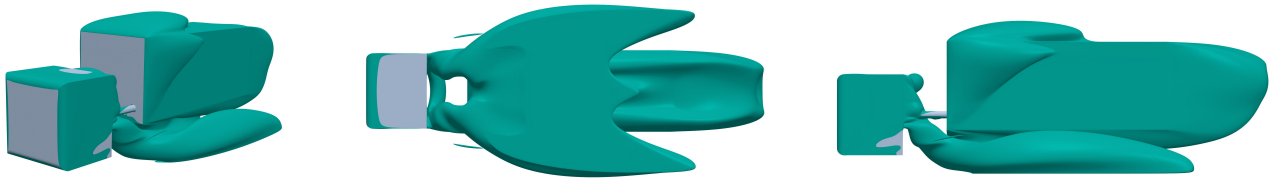

(b) RANS k-ε

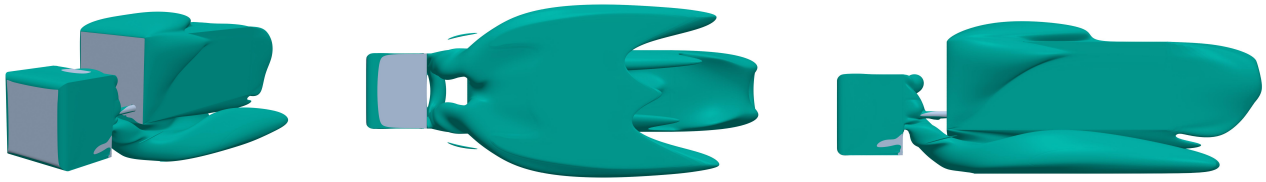

(c) RANS k-ω

Figure 4.34: Iso-surfaces of separation where $C_{p,\mathrm{tot}} = 0$. Left column: isometric view; center column: bottom view; right column: left-side view.

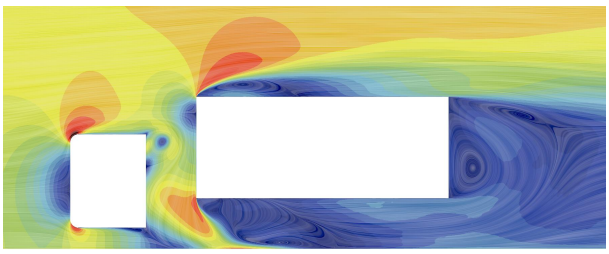

(a) WR LES

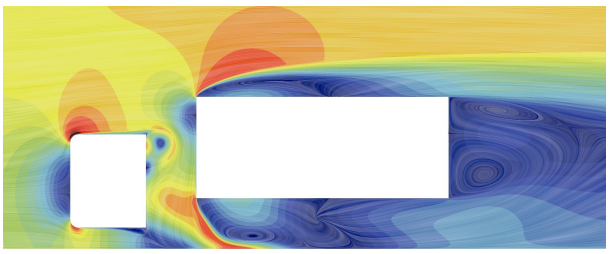

(b) RANS k-ε

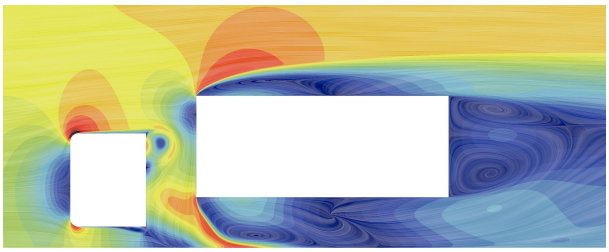

(c) RANS k-ω

Figure 4.35: Average velocity magnitude displayed with line integral convolution in the plane $y = 0.0$ m.

This interpretation is further strengthened by the velocity fields. In Figures 4.35b and 4.35c where the RANS k-ε and k-ω models show a larger separation region above the trailer. The main recirculation features in the trailer wake also differ between the simulations. In the WR LES result in Figure 4.35c, a single larger main recirculation is accompanied by a smaller downstream vortex core, whereas the RANS simulations exhibit a more symmetric dual-vortex structure behind the trailer.

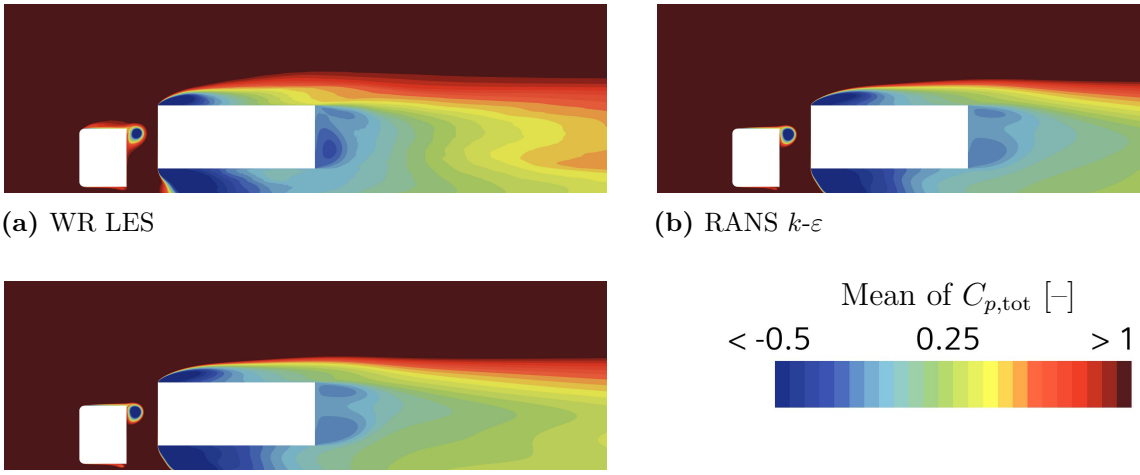

(a) WR LES

(b) RANS k-ε

(c) RANS k-ω

Figure 4.36: Averaged total pressure coefficient in the plane $y = 0.0$ m.

The total-pressure fields in Figures 4.36 and 4.37 provide further evidence of the differences between the RANS and WR LES solutions by highlighting regions associated with total-pressure loss. In the $y = 0.0$ m plane, the k-ε and k-ω results in Figures 4.36b and 4.36c show larger losses in the wake regions above and below the trailer. Although the losses in the near wake appear smaller, the wake extends further downstream in the RANS simulations. In the $z = 0.244$ m plane, Figures 4.37b and 4.37c show that the RANS models predict total-pressure losses in the cab-trailer gap that are similar to those of the LES solution shown in Figure 4.37a. As in the $y = 0.0$ m plane, the main differences stem from increased separation at the trailer front edges and a wider wake extending further downstream.

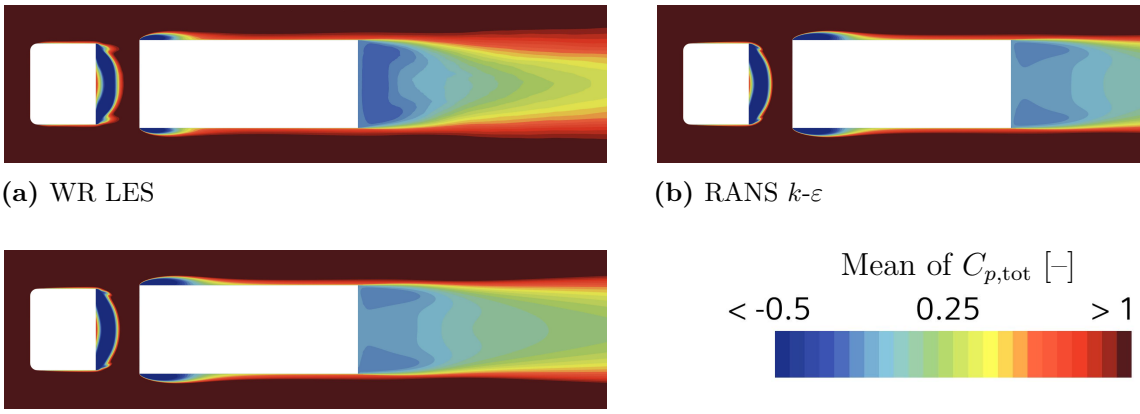

(a) WR LES

(b) RANS k-ε

(c) RANS k-ω

Figure 4.37: Averaged total pressure coefficient in the plane $z = 0.244$ m.

4.6 Summary and Conclusion - Simplified Truck Simulations

Several turbulence models were assessed against a WR LES as the primary high-fidelity reference, with experimental drag and surface-pressure data used for supporting validation. The WR LES showed good agreement with the measured drag coefficient and pressure distributions on both the cab rear face and the trailer front face, confirming its suitability as the reference solution. Among the hybrid approaches, DDES Elliptic Blending k-ε provided the closest overall agreement with WR LES and reproduced the attached-flow separation mode over the cab, as well as a similar drag level. In terms of computational cost, it fell between the WR LES and DDES k-ω SST simulations. WM LES also captured the main separation features and agreed well with the experimental pressure distributions, while being cheaper than DDES k-ω SST. Together with DDES Elliptic Blending k-ε, it emerged as the most promising alternative to WR LES in the present study.

In contrast, DDES k-ω, IDDES k-ω, and SRH k-ω SST predicted extensive cab separation and deviated more from the reference. Including the γ-Re_θ transition model in the k-ω SST-based approaches did not improve the overall agreement with the reference and generally increased the predicted separation at the cab. For the DDES and IDDES cases, it also increased the computational cost. For SRH k-ω SST, however, it produced results closer to the standard DDES k-ω SST case while retaining a lower computational cost. Nevertheless, IDDES k-ω and SRH k-ω SST remain relevant alternatives for full-scale application, as they showed accuracy comparable to the standard DDES k-ω SST setup used at Volvo while requiring lower computational cost. The preferred models for further investigation, together with an overview of which models were cheaper than the DDES k-ω SST model, are presented in Table 4.5. The following chapter extends the analysis to the full-scale configuration.

Table 4.5: Conclusion on scale-resolving turbulence models. Gray rows indicate the reference simulations. Green rows indicate the models selected for production-truck simulations, in addition to DDES k-ω SST. The check mark denotes models that are cheaper than the Volvo standard model, DDES k-ω SST. The SRH k-ω SST $+\gamma$-Re_θ model was not selected because of convergence issues in full-truck simulations.

Model	**Similar to**	**Cheaper than DDES k-ω SST**
WR LES	High–resolution reference	
WM LES	WR LES	
DDES EB k-ε	WR LES	✓
DDES k-ω SST	Volvo standard model	
IDDES k-ω SST	DDES k-ω SST	✓
SRH k-ω SST	DDES k-ω SST	✓
DDES k-ω SST + γ-Re_θ	DDES k-ω SST	
IDDES k-ω SST + γ-Re_θ	DDES k-ω SST	
SRH EB k-ε	DDES k-ω SST	
SRH Lag EB k-ε	DDES k-ω SST	
SRH k-ω SST + γ-Re_θ	DDES k-ω SST	✓

5

Production Truck

This chapter presents the methodology and results for the production truck simulations. The objective is to evaluate the selected turbulence models under full-scale, industry-relevant conditions and to assess their ability to reproduce measured drag levels and pressure distributions. Compared with the simplified truck case, the present configuration includes a much more detailed geometry and a more complex aerodynamic flow field, making it a more demanding test of model robustness and numerical setup. To ensure consistency with Volvo Group's production workflow, the simulations follow standard external-aerodynamics CFD procedures in Siemens Simcenter STAR-CCM+, and the numerical setup is based on Volvo truck best practices. The chapter begins with the wind-tunnel correlation cases for Configuration 1 and then extends the analysis to the selected model comparison and additional vehicle configurations.

5.1 Model Description and Simulation Setup

To assess the turbulence models at an industrially relevant level, a full-scale vehicle model was investigated. Insights from the simplified truck study were used to guide the selection of turbulence models, and five models were chosen for further evaluation on the complete vehicle configuration. The simulation methodology was based on the initial work by Josefsson [42] and was later further developed by the aerodynamics team at Volvo Group.

The simulations included both wind-tunnel configurations, which were used to correlate numerical results with wind-tunnel measurements, and open-road configurations, which were used to evaluate the selected turbulence models and prism-layer mesh strategies. All simulations were performed using a transient approach. To ensure a stable and consistent initialization of the flow field, each transient case was preceded by a steady-state precursor simulation of 2500 iterations. The resulting solution was then used as the initial condition for the transient computation, reducing start-up transients and improving convergence behavior. This procedure was applied consistently across all investigated vehicle variants, which are introduced in the following subsection. Drag-coefficient uncertainty is quantified using the 95% confidence interval defined in section 2.1.2.2.2.

Due to confidentiality restrictions, raw pressure values cannot be disclosed. Therefore, the pressure fields and plots are presented only in scaled form, allowing comparison of the results without revealing absolute values.

5.1.1 Geometry Description

The wind tunnel correlation study was conducted using a production Volvo FH truck from 2017. Four vehicle variants based on the same tractor with a shortened trailer were considered, referred to here as configurations 1–4. The shortened trailer with a length of 9.1 m was used since a full-length trailer cannot be accommodated at yaw within the wind tunnel test section. This production vehicle was selected primarily because an extensive body of wind tunnel data is available for this configuration. The reference configuration used in the experiments is shown in Figure 5.1. Table 5.1 presents the geometrical differences between the configurations. Due to confidentiality restrictions configurations 2–4 can not be displayed.

Table 5.1: Specific modifications for each evaluated vehicle configuration.

Configuration	Variant	Modifications
1	Reference	Baseline geometry
2	Smaller update	Wheelhouse updates
3	Larger update	Extended front
4	Mirrorless	Removed mirrors

Figure 5.1: FH truck with wind tunnel mountings and the shortened trailer.

5.1.2 Experimental Method for Simulation Correlation

The numerical methodology was validated against full-scale wind tunnel measurements performed at the National Research Council (NRC) in Ottawa, Canada [6]. This experimental

database served as the reference for comparison with the CFD results. The NRC wind tunnel has a test section measuring 9.1 m × 9.1 m × 25 m and a 6.1 m diameter turntable. Although the facility is equipped with a ground suction system, it was not activated during the experiments. Figure 5.2 shows the truck at −10° in the tunnel together with the floor, turntable, and the platforms housing the balance used for force measurements.

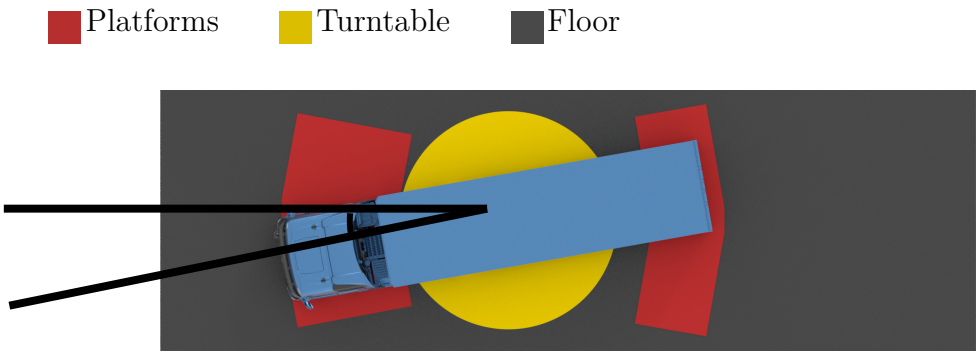

Figure 5.2: Truck model in the NRC wind tunnel at −10° yaw, with the platforms, turntable, floor, and yaw-angle spread indicated.

Since the ground suction system was not used, the incoming boundary layer had to be represented numerically. The boundary layer in the empty tunnel was therefore first compared with measurements, and the near-floor flow was subsequently reproduced using a flat-plate boundary-layer-based inlet condition. Inlet and boundary conditions were tuned until the simulated profile matched the measured tunnel flow.

Tunnel inlet velocity was set to approximately 17 km/h, which yields a test-section velocity of 90 km/h after contraction. This choice was made to reproduce the experimentally observed non-uniform inlet profile entering the test section. The tunnel dimensions were obtained directly from NRC, while the contraction ratio and diffuser angle were taken from Garry et al. and Johansson [50, 51].

Due to the truck inducing a blockage ratio of approximately 13%, pressure losses in the tunnel are non-negligible and must be accounted for in the analysis. This was handled by defining a non-zero reference pressure, P_{ref}, based on the stagnation pressure measured upstream of the vehicle. The reference pressure was computed using Bernoulli's equation as

$$P_{\text{ref}} = P_0 - \frac{\rho v_\infty^2}{2},$$

where P_0 is the stagnation pressure, ρ is the fluid density, and v_∞ is the free-stream velocity.

5.1.3 Turbulence Models

Table 5.2: Turbulence models evaluated in full scale truck aerodynamic simulations

Model Type	**Description**
LES	WALE WM LES
DDES	DDES EB k-ε
DDES	DDES k-ω
DDES	IDDES k-ω
SRH	SRH k-ω

The five turbulence models initially evaluated on the full-scale truck are presented in Table 5.2. WM LES and DDES EB were included based on their strong performance in the simplified truck study. DDES k-ω was selected as the reference model, as it is the standard model used in the current simulation setup. IDDES k-ω and SRH k-ω were chosen because of similar performance to DDES k-ω in the simplified truck study. To ensure a consistent comparison, all models were evaluated on the same computational mesh using the same timestep.

5.1.4 Computational mesh

The computational mesh was created using the Volvo Group standard aerodynamic simulation method with modifications for a wind tunnel configuration. The mesh was constructed with a low y^+ approach with refinements in the regions containing large gradients, resulting in approximately 400 million cells. Figure 5.3 displays the mesh at the centerline.

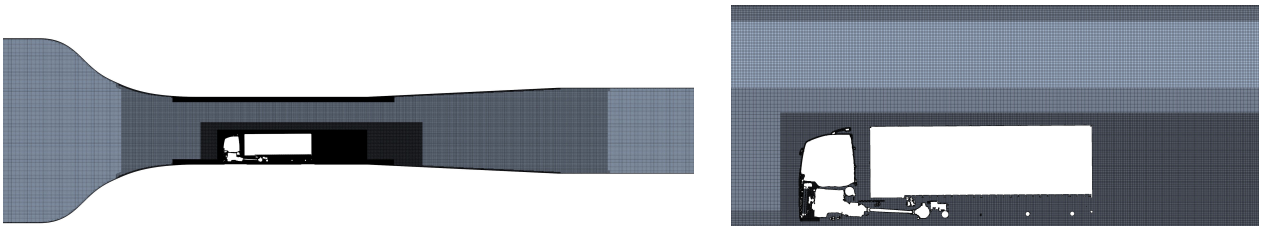

(a) Full mesh at $y = 0.0$ m. **(b)** Focus on mesh around truck at $y = 0.0$ m

Figure 5.3: Computational mesh used for simulations of the fully detailed production truck in a wind tunnel domain.

5.2 Initial Assessment of Turbulence Models

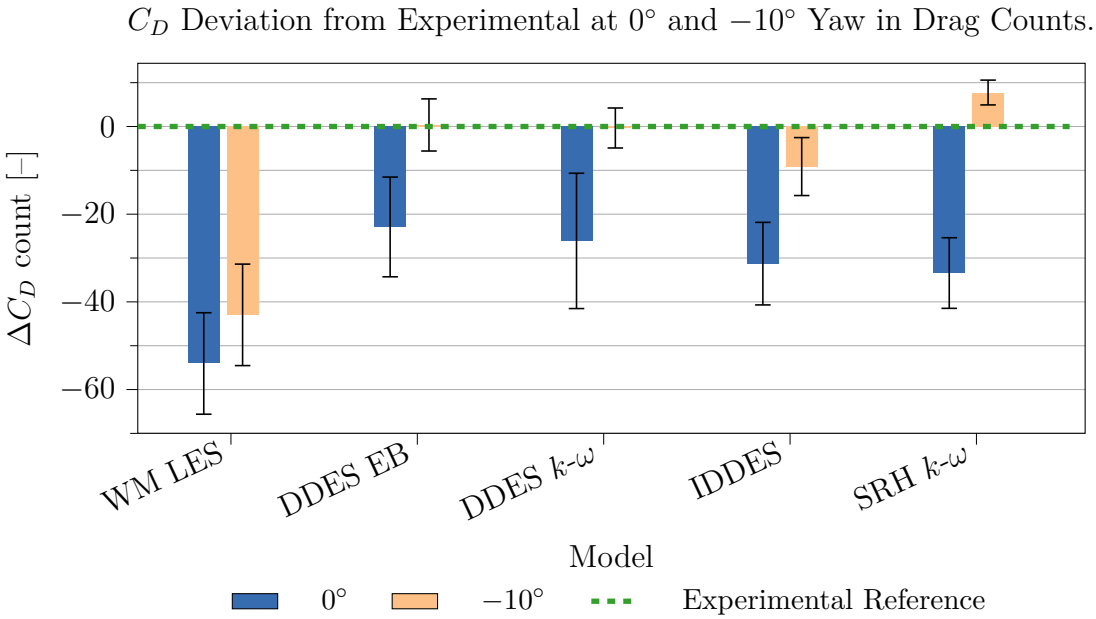

Figure 5.4: Average C_D deviation in drag counts from experiment at 0° (left bar) and −10° (right bar) yaw for all models. Error bars indicate the 95% confidence interval.

All turbulence models are assessed using both global measurements of the drag coefficient C_D, and local measurements of pressure. Drag coefficient agreement is treated as the primary selection criteria, while local trailer and cab pressure distributions are used to evaluate the consistency of flow prediction. The selected turbulence models were evaluated against wind tunnel drag coefficients and pressure-tap measurements from the flow survey [6] at yaw angles of 0° and −10°. Relative error in C_D is summarized in Figure 5.4. Overall, DDES EB, DDES k-ω, and IDDES k-ω show the best agreement with the experimental drag values, whereas WMLES and SRH k-ω SST exhibit larger deviations. The model-specific behavior is discussed in the following subsections.

5.2.1 WM LES

The WM LES results indicate that the present full-truck simulation configuration is not suitable for accurate drag prediction with this model. It shows the largest drag-count deviation from the experiment with underprediction at both yaw angles, indicating that the present mesh and wall treatment are insufficient for accurate force prediction. Although the mesh scaling is comparable to that used in the Allan-model simulations, presented in Chapter 4, the spanwise and streamwise resolution become too coarse with Δx^+ exceeding 1000 in several critical regions. Under these conditions it seems that the wall model is unable to reproduce the near wall velocity accurate enough for reliable drag prediction.

5.2.2 SRH k–ω SST

The SRH k-ω SST model performs better than WM LES, but it remains less accurate than the DDES- and IDDES-based approaches. At 0° yaw, it underpredicts the drag more

strongly, whereas at $-10°$ yaw it overpredicts the drag, leading to an overestimation of the yaw sensitivity of the drag coefficient. Nevertheless, the SRH model may be considered a computationally efficient alternative, although it does not match the better-performing models in either absolute drag prediction or yaw sensitivity.

5.2.3 DDES k–ω SST, IDDES k–ω SST and DDES EB k–ε

Among the evaluated turbulence models, DDES k-ω SST, IDDES k-ω SST, and DDES EB k-ε provide the closest agreement with the experimental drag data and therefore constitute the most promising approaches for the present full-truck configuration. All models slightly underpredict the drag coefficient at $0°$ yaw. Among them, DDES EB gives the closest agreement with the experiment, followed by DDES k-ω and lastly IDDES k-ω. At $-10°$ yaw, both DDES EB and DDES predict the drag coefficient accurately, whereas IDDES still underpredicts C_D. Since these three models give the best drag agreement, the remaining analysis focuses on their ability to reproduce the measured flow and pressure distributions. This is used to determine which model provides the best overall balance between global force prediction and local flow realism.

5.2.3.1 Tunnel-Plane Velocity Fields

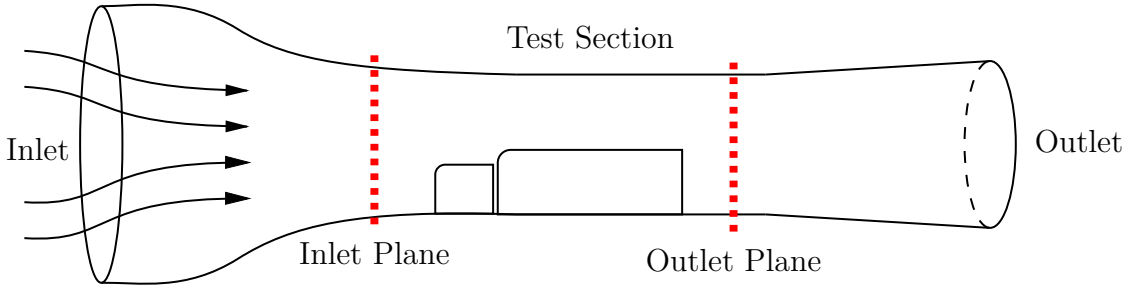

Figure 5.5: Schematic representation of the main section of the NRC wind tunnel in Canada. The positions of inlet and outlet measurement planes are marked by the dashed lines.

The velocity measurements in the inlet and outlet planes, located at the test section inlet and outlet shown in Figure 5.5, show that the three simulations reproduce the overall wind-tunnel flow well, with only small differences between the models. All three models show good agreement with the experimental inlet velocity field. DDES and IDDES, shown in Figures 5.6a and 5.6b, provide the most accurate field-average values, which indicates that the inlet conditions are well calibrated for these two cases. Observations of the DDES EB result in Figure 5.6c show a slightly larger deviation, suggesting a small remaining mismatch in the inlet calibration. This difference is minor but may still influence the absolute pressure levels in the comparison. A fully fair comparison would require the DDES EB inlet conditions to be calibrated to the same level, but this was outside the scope of the present study.

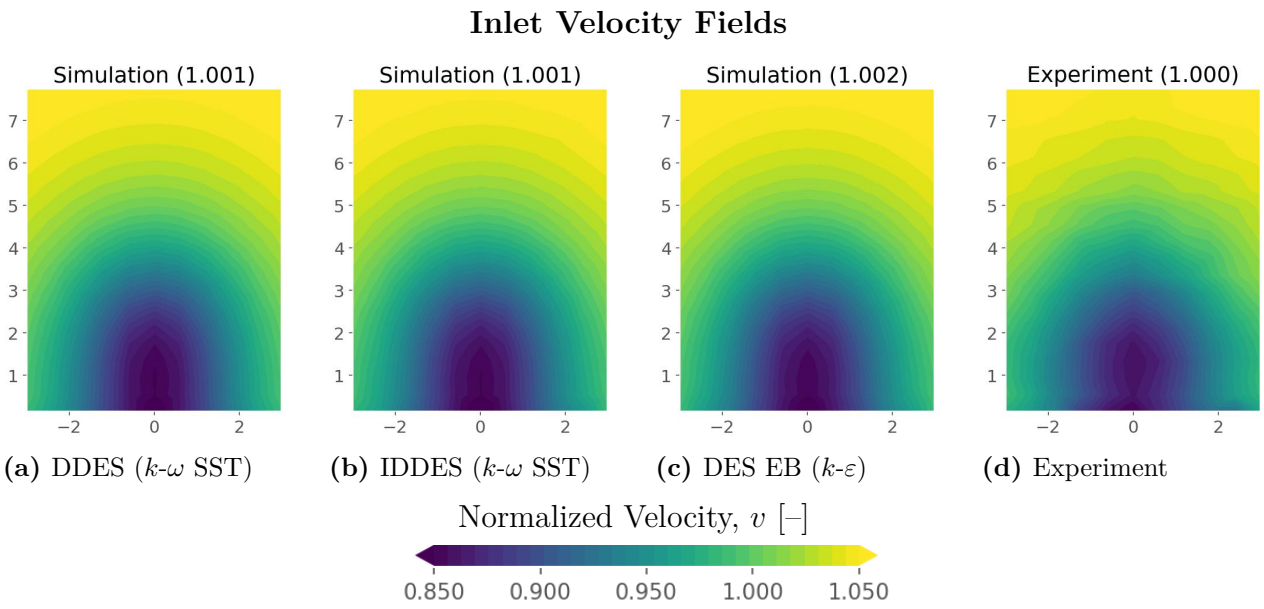

(a) DDES (k-ω SST) **(b)** IDDES (k-ω SST) **(c)** DES EB (k-ε) **(d)** Experiment

Figure 5.6: Normalized velocity magnitude in the wind-tunnel inlet plane. Field average values normalized by experimental values shown above each field.

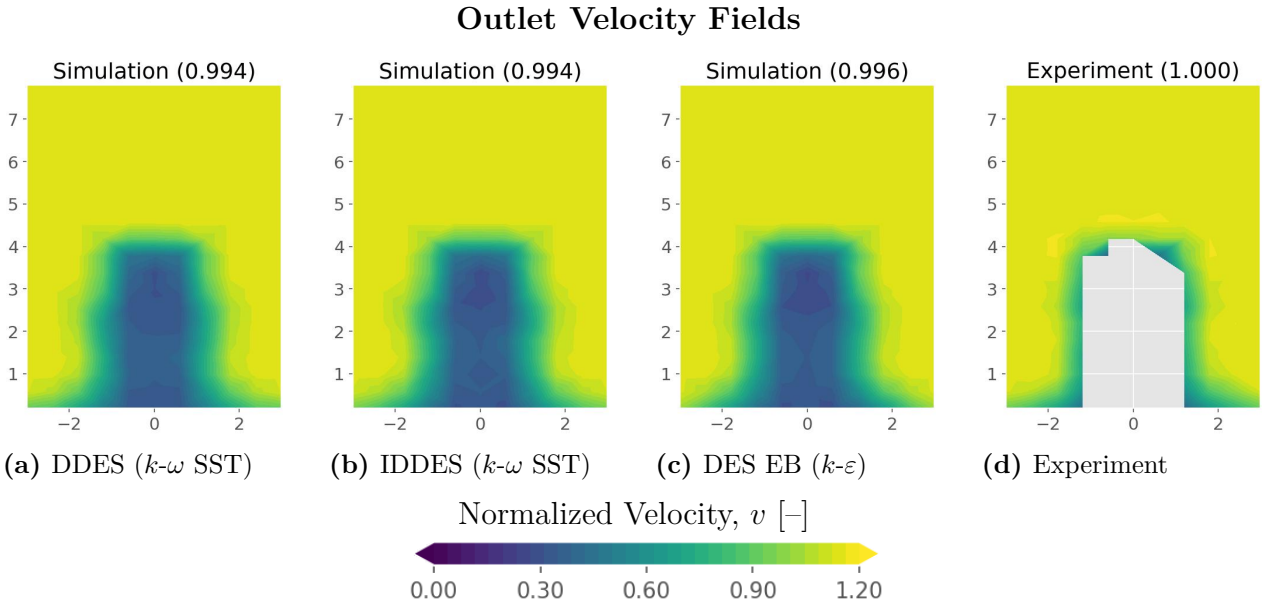

(a) DDES (k-ω SST) **(b)** IDDES (k-ω SST) **(c)** DES EB (k-ε) **(d)** Experiment

Figure 5.7: Normalized velocity magnitude field plots in the wind-tunnel outlet plane. Field averaged values normalized by experimental values shown above each field. Gray regions in the experimental plots indicate invalid measurements due to backflow.

Similarly all models show good agreement with the experimental outlet velocity field. The DDES and IDDES results in Figures 5.7a and 5.7b have field-average deviations of about 0.6%, while the DDES EB result in Figure 5.7c agrees slightly better, with a deviation of about 0.4%. However, this small advantage should be interpreted with some caution, since it may partly reflect the slightly less accurate inlet calibration in the DDES EB case rather than a consistently better prediction of the tunnel flow. Taken together, the inlet and outlet velocity fields indicate that all three models reproduce the tunnel flow reasonably well, although the

slightly less accurate inlet calibration in the DDES EB case should be kept in mind when comparing absolute pressure levels.

5.2.3.2 Tunnel-plane pressure fields

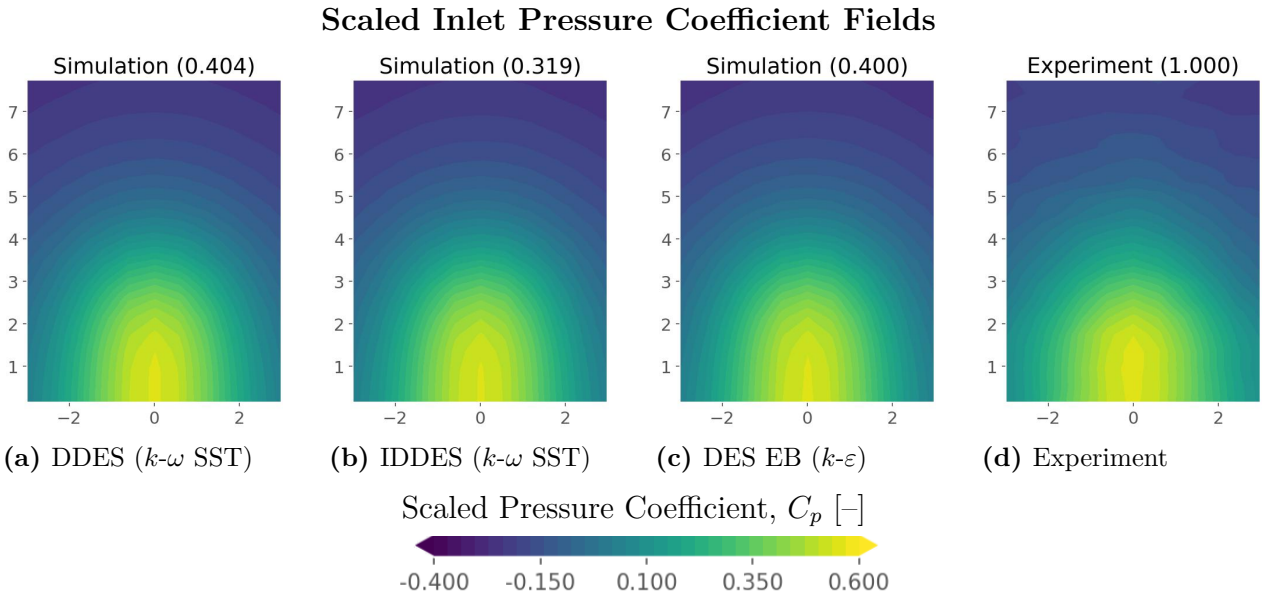

(a) DDES (k-ω SST) **(b)** IDDES (k-ω SST) **(c)** DES EB (k-ε) **(d)** Experiment

Figure 5.8: Pressure coefficient, linearly rescaled to a unit range, in the wind-tunnel inlet plane. Field-averaged values normalized by the experimental average are shown above each field. Note: since the unscaled inlet pressure is near zero, the normalized averages are sensitive to small absolute differences.

Compared with the velocity fields, the inlet and outlet pressure measurements taken in the same planes provide additional insight into the performance of the turbulence models. The inlet pressure fields in Figure 5.8 are broadly similar across all three models and compare well with the experimental field structure. Although the area-averaged normalized coefficient differs noticeably between the simulations and the experiment, the unscaled inlet pressure levels remain close to zero, meaning that small absolute differences are amplified significantly upon normalization. In absolute terms, the largest deviation is obtained with IDDES in Figure 5.8b, but this deviation is limited to under 20 counts relative to the experiment. In terms of the average inlet pressure level, DDES in Figure 5.8a agrees best with the measurements, closely followed by DDES EB in Figure 5.8c.

At the outlet plane in Figure 5.9, the differences between the models become more pronounced, both in the spatial pressure distribution and in the field-average values. The DDES EB simulation in Figure 5.9c provides the best agreement with the experimental field average pressure level, followed by DDES k-ω and IDDES k-ω in figures 5.9a and 5.9b. For all three models, the outlet pressure is overpredicted, which indicates that the simulated pressure losses are smaller than those measured in the wind tunnel experiment. This overprediction is consistent with the overall underprediction of C_D. The experimental pressure field also shows irregularities that are not reproduced in the simulations. These differences are most likely caused by the non-uniform wind-tunnel inlet flow shown in Figure 5.10, which is not included in the simulated inlet conditions. Overall, the tunnel-plane comparisons show that all three candidate models reproduce the main flow features in the wind tunnel well, while the remaining differences are mainly in the absolute pressure levels and local asymmetries not

captured in the simulations.

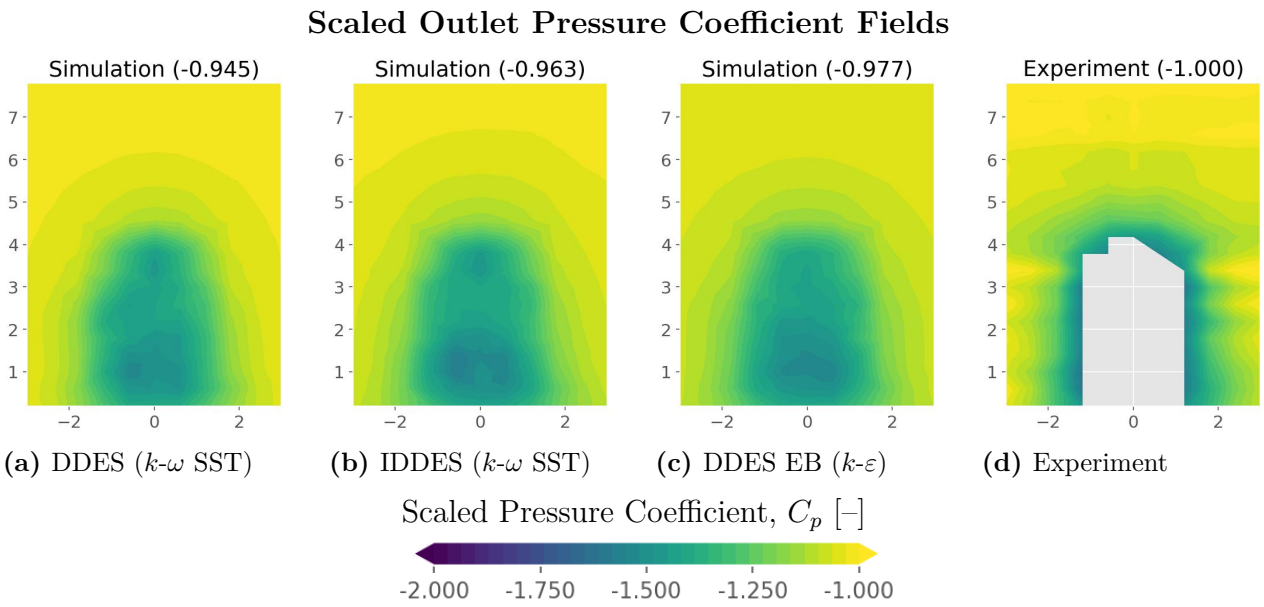

(a) DDES (k-ω SST) **(b)** IDDES (k-ω SST) **(c)** DDES EB (k-ε) **(d)** Experiment

Figure 5.9: Pressure coefficient, linearly rescaled to a unit range, in the wind-tunnel outlet plane. Field averaged values normalized by experimental values shown above each field. Gray regions in the experimental plots indicate invalid measurements due to backflow.

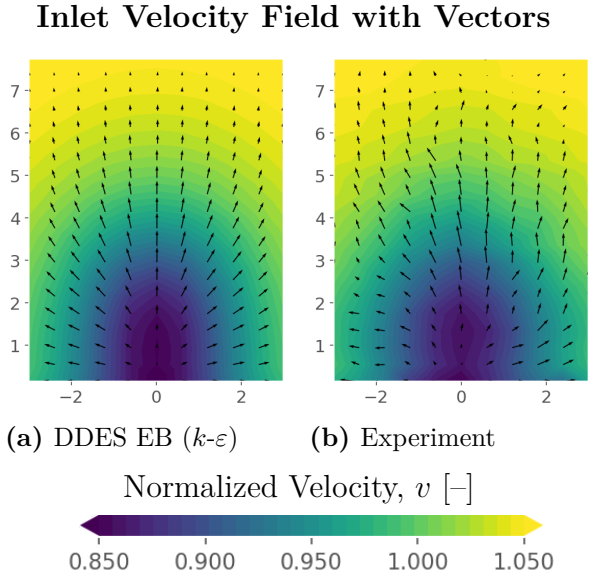

(a) DDES EB (k-ε) **(b)** Experiment

Figure 5.10: Normalized velocity magnitude with vectors in the wind-tunnel inlet plane.

5.2.3.2.1 Results - Cab

Figure 5.11: Pressure tap positions on cab of Configuration 1, marked with numbers. Figure taken with permission from [6].

This section evaluates the ability of the selected turbulence models to reproduce the surface-pressure distribution on the cab. The comparison is based on pressure-tap measurements along the wrap-around tap line and on interpolated pressure-coefficient fields on the left and right sides of the cab at 0° and −10° yaw. Figure 5.11 shows the pressure-tap locations used for the experimental and numerical measurements. The taps are placed on both the left and right sides of the cab, extending from the A-pillars across the doors. Additional taps are located further downstream toward the side deflectors. Combined with the front-side taps, these create a continuous line of measurement points wrapping around the cab from deflector to deflector.

The cab wrap-around pressure line, shown in Figure 5.12, demonstrates that all three models reproduce the overall pressure development reasonably well at both yaw angles. At 0° yaw, the experimental data in Figure 5.12a exhibits a slight asymmetry between the left and right corners, likely caused by residual inlet swirl in the wind tunnel or possibly also by small differences in tap location in regions of steep pressure gradient. Since no inlet swirl is imposed in the simulations, the numerical results remain more symmetric. Among the three models, DDES k-ω gives the best agreement on the left side, whereas both DDES and IDDES k-ω tend to overpredict pressure toward the right side. DDES EB instead underpredicts the pressure more uniformly along the line.

At −10° yaw, shown in Figure 5.12b, the model differences become more pronounced and the pressure minima are more difficult to capture, although all three models still follow the measured trend reasonably well. On the left side, DDES k-ω gives the best agreement, while IDDES k-ω shows the largest underprediction. On the right side, DDES EB agrees best with the measurements, whereas DDES k-ω shows the largest deviation, although the differences remain modest. Overall, the wrap-around line provides only limited separation between the models at 0° yaw, but model differences are clearer at −10° yaw, where DDES k-ω and DDES EB show the strongest local agreement.

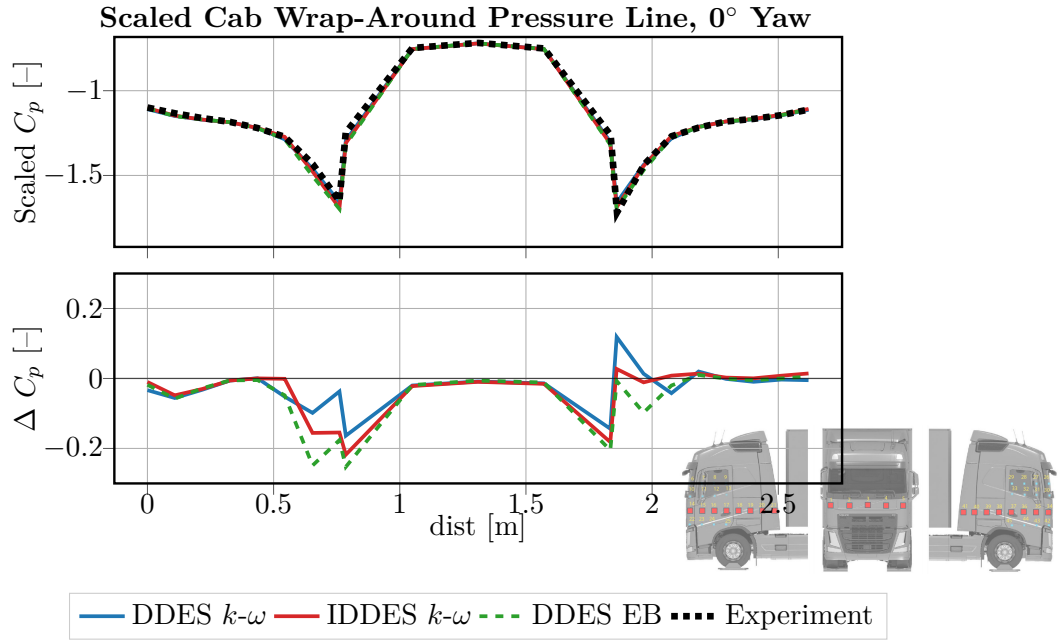

(a) 0° yaw

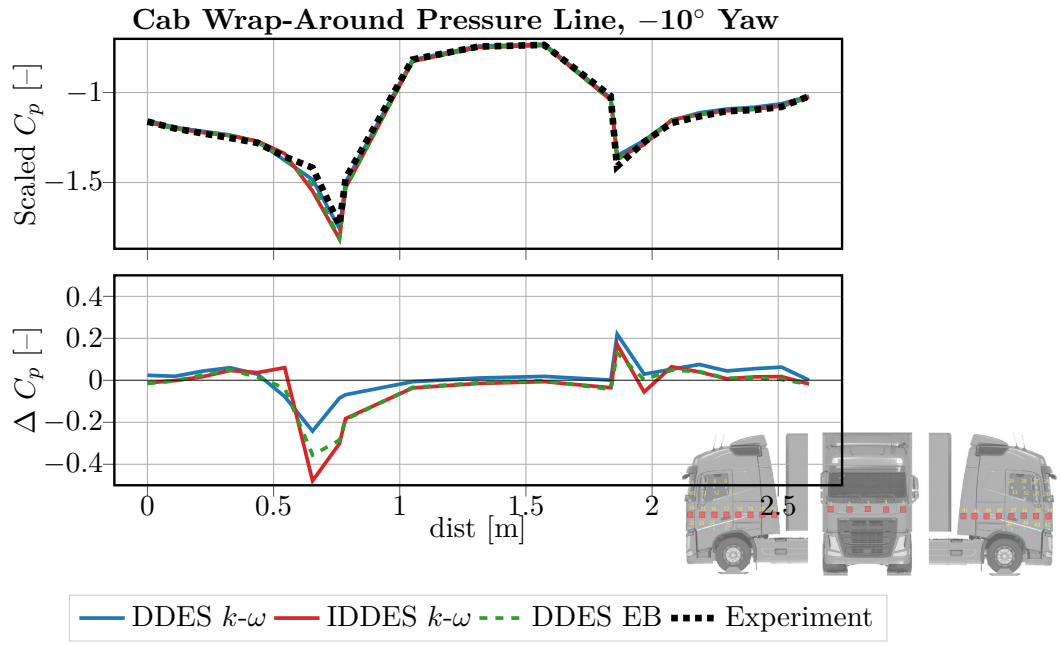

(b) −10° yaw

Figure 5.12: Cab surface pressure distribution along the tap line wrapping from the left side, around the front, to the right side. The top shows the pressure coefficient, linearly rescaled to a unit range, and the bottom plot shows the absolute deviation from experiment.

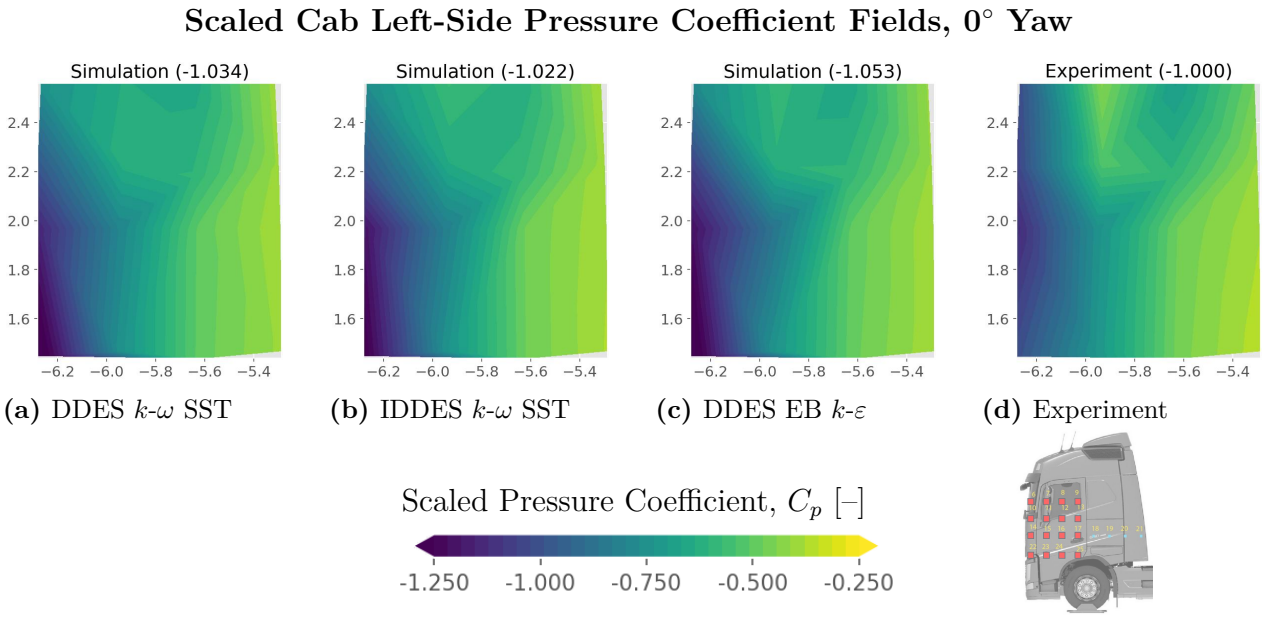

(a) DDES k-ω SST **(b)** IDDES k-ω SST **(c)** DDES EB k-ε **(d)** Experiment

Figure 5.13: Pressure coefficient fields, linearly rescaled to a unit range, from left-side pressure taps at 0° yaw. Normalized field average values are shown above each field.

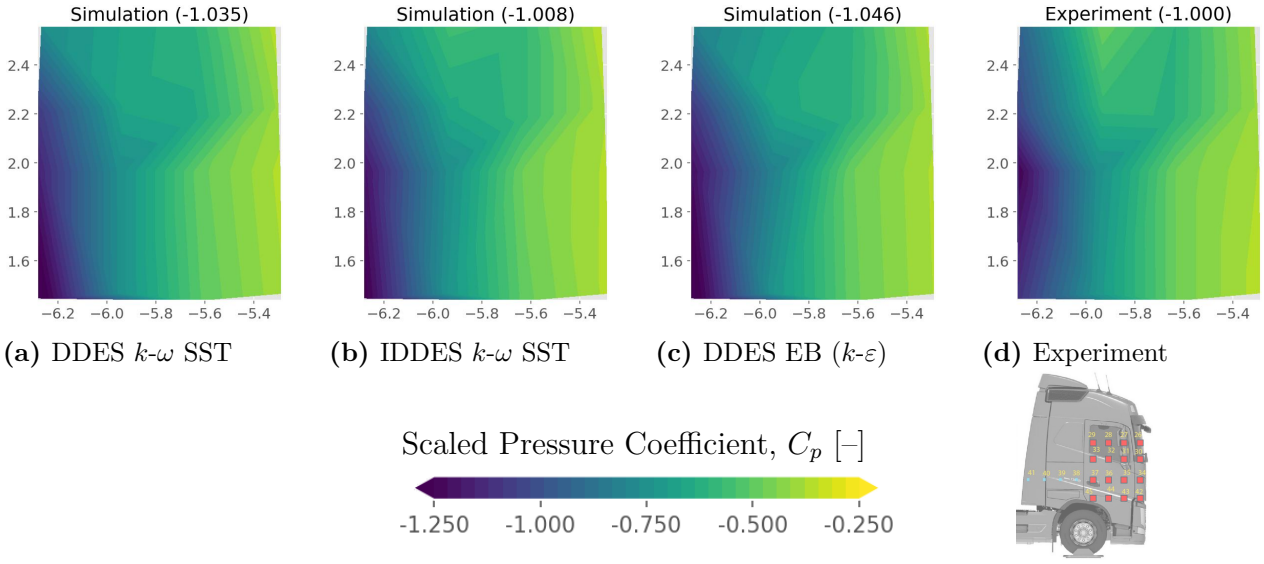

(a) DDES k-ω SST **(b)** IDDES k-ω SST **(c)** DDES EB (k-ε) **(d)** Experiment

Figure 5.14: Pressure coefficient fields, linearly rescaled to a unit range, from right-side pressure taps at 0° yaw. Normalized field average values are shown above each field.

Consistent with the wrap-around line results, the left- and right-side cab pressure fields at 0° yaw, in Figures 5.13 and 5.14, show similar overall behavior across the three models. On both sides, the IDDES k-ω results in Figures 5.13b and 5.14b show the best agreement with the experimental field-average values and also capture the spatial distribution well. For DDES EB in Figures 5.13c and 5.14c the spatial pressure distribution is also well reproduced, but they show the largest deviation in field-average value. The DDES k-ω results in Figures 5.13a and 5.14a lie between these two cases with somewhat weaker spatial agreement than IDDES k-ω and somewhat better field-average values than DDES EB. Overall, the 0° cab-side pressure fields favor IDDES k-ω as the most consistent model.

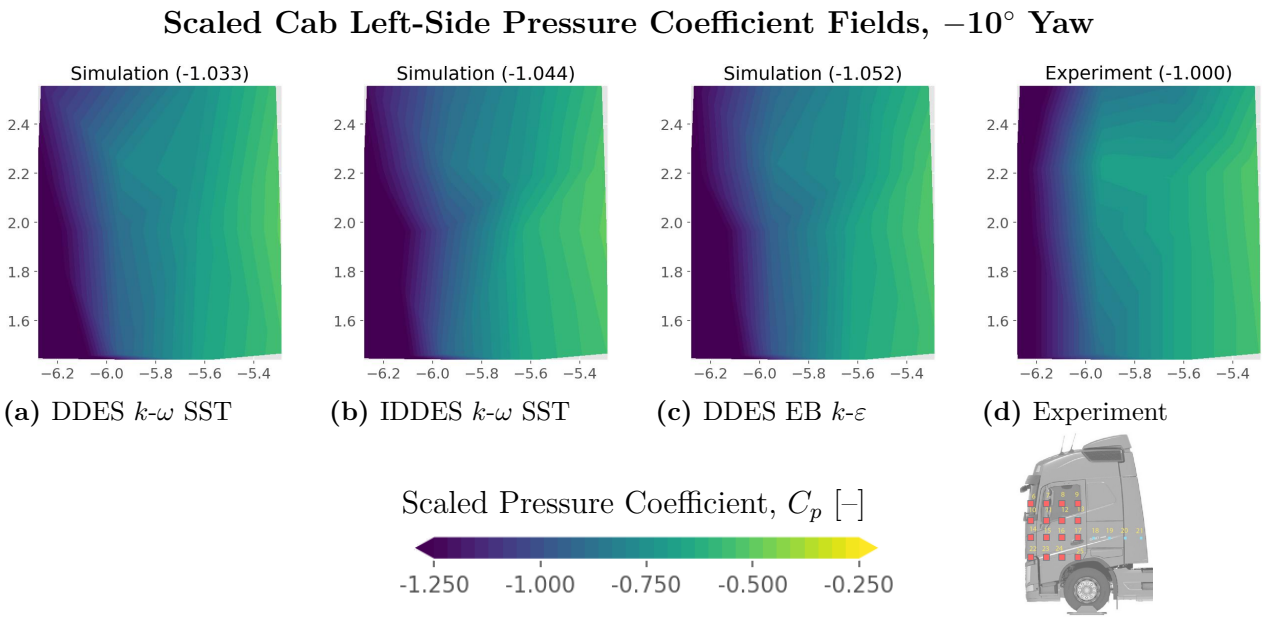

(a) DDES k-ω SST **(b)** IDDES k-ω SST **(c)** DDES EB k-ε **(d)** Experiment

Figure 5.15: Pressure coefficient fields, linearly rescaled to a unit range, from left-side pressure taps at −10° yaw. Normalized field average values are shown above each field.

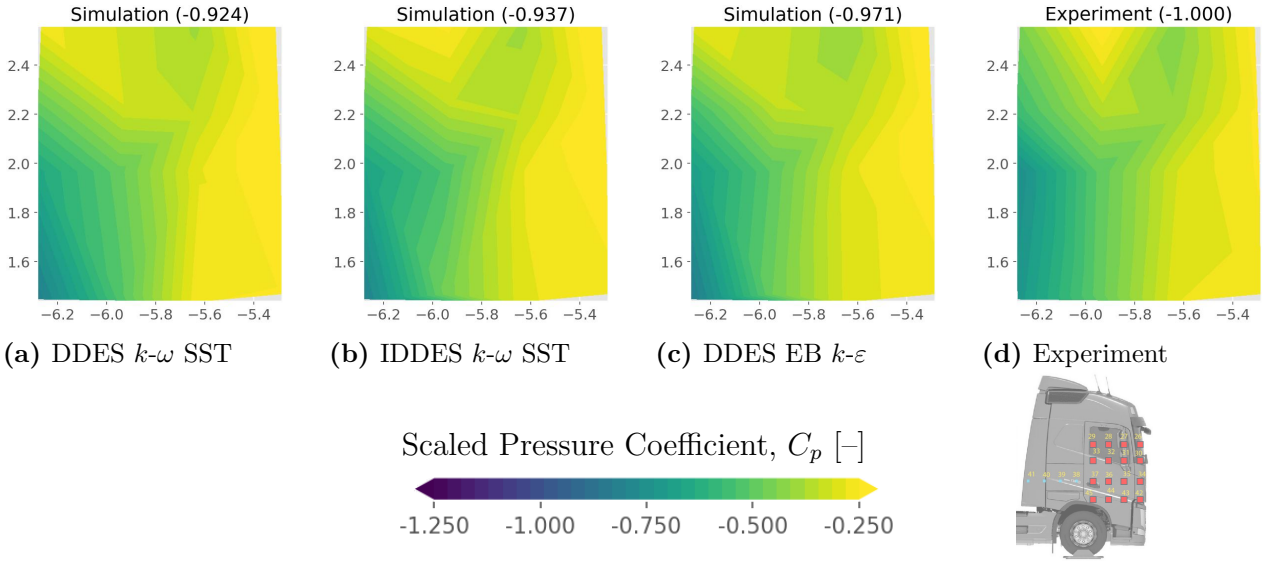

(a) DDES k-ω SST **(b)** IDDES k-ω SST **(c)** DDES EB k-ε **(d)** Experiment

Figure 5.16: Pressure coefficient fields, linearly rescaled to a unit range, from right-side pressure taps at −10° yaw. Normalized field average values are shown above each field.

The left- and right-side cab pressure fields at −10° yaw, shown in Figures 5.15 and 5.16, indicate larger differences between the models than at 0° yaw. On the left side, DDES k-ω in Figure 5.15a gives the most accurate field-average pressure level, while IDDES k-ω in Figure 5.15b provides the best spatial agreement with the measurements. DDES EB reproduces the overall field structure reasonably well, as seen in Figure 5.15c, but shows the largest deviation in field-average value. On the right side, DDES EB in Figure 5.16c gives the best agreement in field-average pressure level, while it performs similarly in terms of spatial pressure distribution to IDDES k-ω in Figure 5.16b. DDES k-ω in Figure 5.16a shows the weakest overall agreement on this side. Taken together, the −10° cab-side pressure fields show that IDDES k-ω and DDES EB perform similarly well.

Overall, the cab pressure measurements show only small differences between the models. In terms of field-average pressure level, IDDES k-ω and DDES k-ω generally agree somewhat better with the measurements than DDES EB, although the differences are modest. In terms of spatial pressure distribution, IDDES k-ω and DDES EB are generally very similar, while DDES k-ω is also close but tends to be slightly less consistent. Taken together, the cab results do not clearly separate between models, although they indicate a small advantage for IDDES k-ω and DDES EB in terms of spatial agreement.

5.2.3.2.2 Results - Trailer

This section evaluates the ability of the selected turbulence models to reproduce the surface-pressure distribution on the trailer. Since the trailer wake and base pressure contribute strongly to the total aerodynamic drag, these pressure distributions are particularly important for the final model assessment. Comparisons are based on pressure-tap measurements along the trailer sides and roof, together with interpolated pressure-coefficient fields on the trailer rear at 0° and −10° yaw. The pressure-tap locations are shown in Figure 5.17, including tap lines along the sides and roof and a measurement grid covering the trailer rear surface.

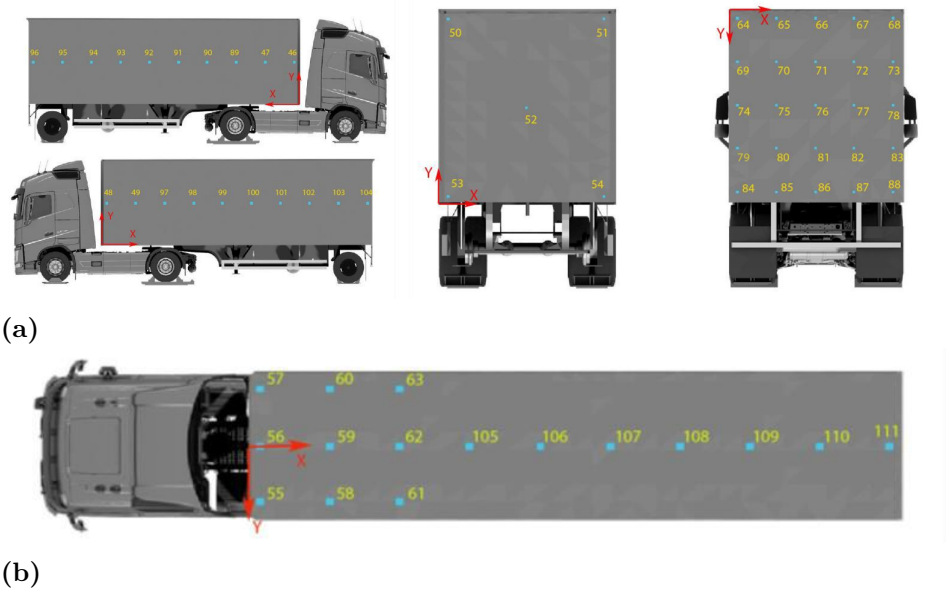

Figure 5.17: Pressure tap locations on trailer. Figure taken with permission from [6].

Pressure measurements along the left and right sides of the trailer at 0° yaw, shown in Figure 5.18, show good agreement with the experimental data for all three models. Underprediction near the front and rear of the trailer is observed in all cases. On both sides, DDES EB provides the closest overall agreement, with less underprediction along most of the trailer length. DDES k-ω performs similarly, although with slightly larger deviations, while IDDES k-ω shows the weakest overall agreement on both sides.

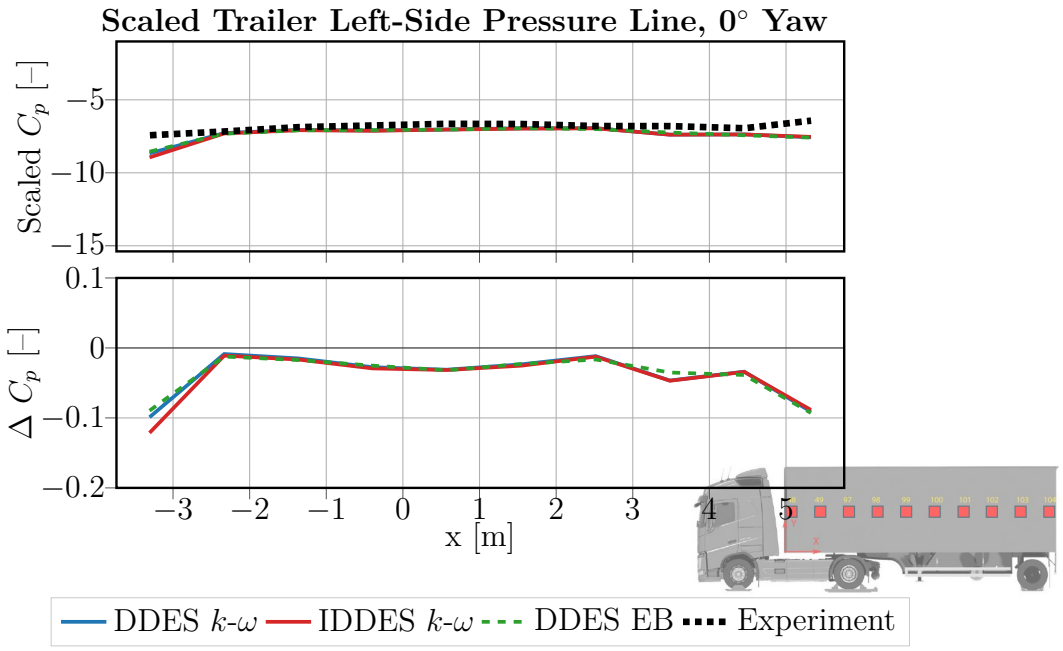

(a) Left side, 0° yaw

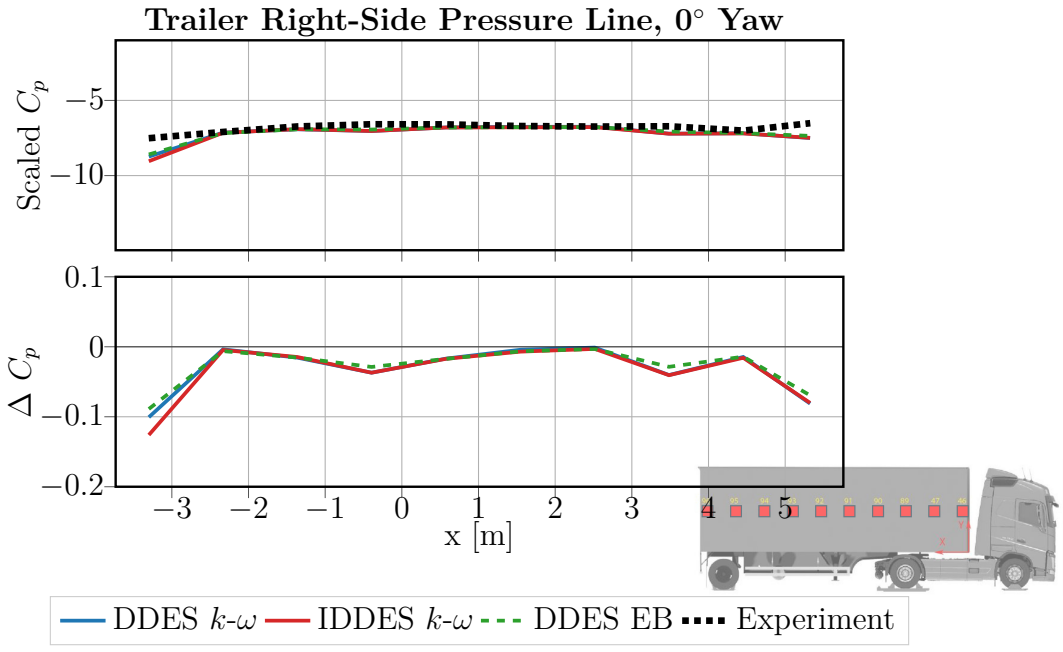

(b) Right side, 0° yaw

Figure 5.18: Trailer-side pressure distributions along the pressure-tap lines at 0° yaw. The top shows the pressure coefficient, linearly rescaled to a unit range, and the bottom plot shows the absolute deviation from experiment.

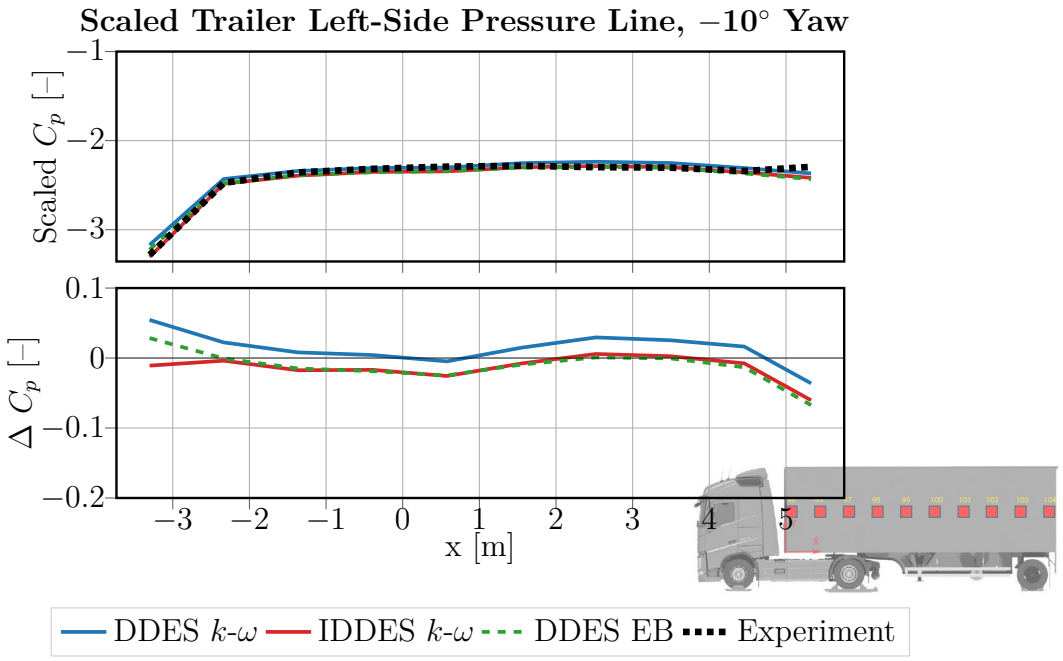

(a) Left side, −10° yaw

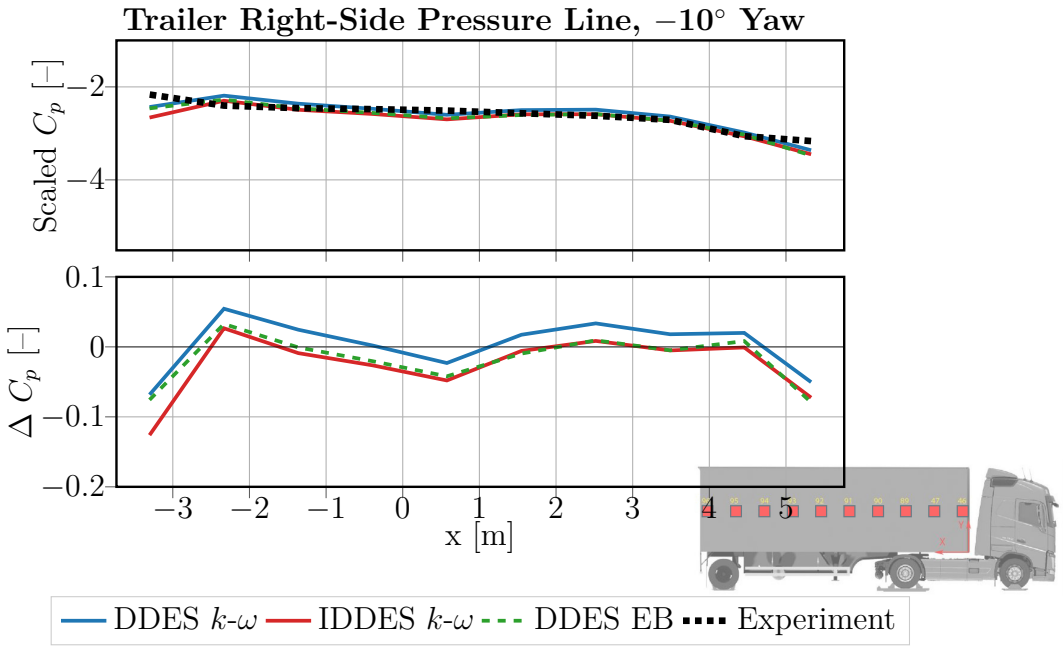

(b) Right side, −10° yaw

Figure 5.19: Trailer-side pressure distributions along the pressure-tap lines at −10° yaw. The top shows the pressure coefficient, linearly rescaled to a unit range, and the bottom plot shows the absolute deviation from experiment.

At $-10°$ yaw, the differences between the models become more pronounced. On the left side, shown in Figure 5.19a, all three models capture the overall pressure trend, but with clear differences in pressure level. IDDES k-ω provides the best overall agreement across most of the trailer, largely because it predicts the front pressure more accurately than DDES EB. DDES EB follows a similar trend, but slightly overpredicts the pressure near the front and underpredicts it near the rear. DDES k-ω is shifted toward higher pressure levels, which leads to overprediction along most of the trailer length and gives the weakest agreement on this side.

On the right side, shown in Figure 5.19b, all three models again show the same general behavior, with underprediction near both the front and rear of the trailer. As on the left side, DDES k-ω is shifted toward higher pressure levels than the other models, which reduces the local underprediction but leads to overprediction over much of the trailer length. DDES EB provides the closest overall agreement with the measurements on this side. Taken together, the trailer-side pressure lines at $-10°$ yaw favor IDDES k-ω on the left side and DDES EB on the right, while DDES k-ω is less consistent overall.

The trailer-roof pressure distributions, shown in Figure 5.20, are difficult to reproduce accurately for all three models. At both yaw angles, the simulations overpredict the pressure near the front of the trailer, followed by alternating regions of underprediction and overprediction, and finally by overprediction toward the rear. The deviations are larger at $-10°$ yaw in Figure 5.20b than at $0°$ yaw in Figure 5.20a, although the overall behavior is similar. $-10°$ yaw shows the clearest distinction between the models, where DDES k-ω is shifted toward higher pressure levels than IDDES k-ω and DDES EB.

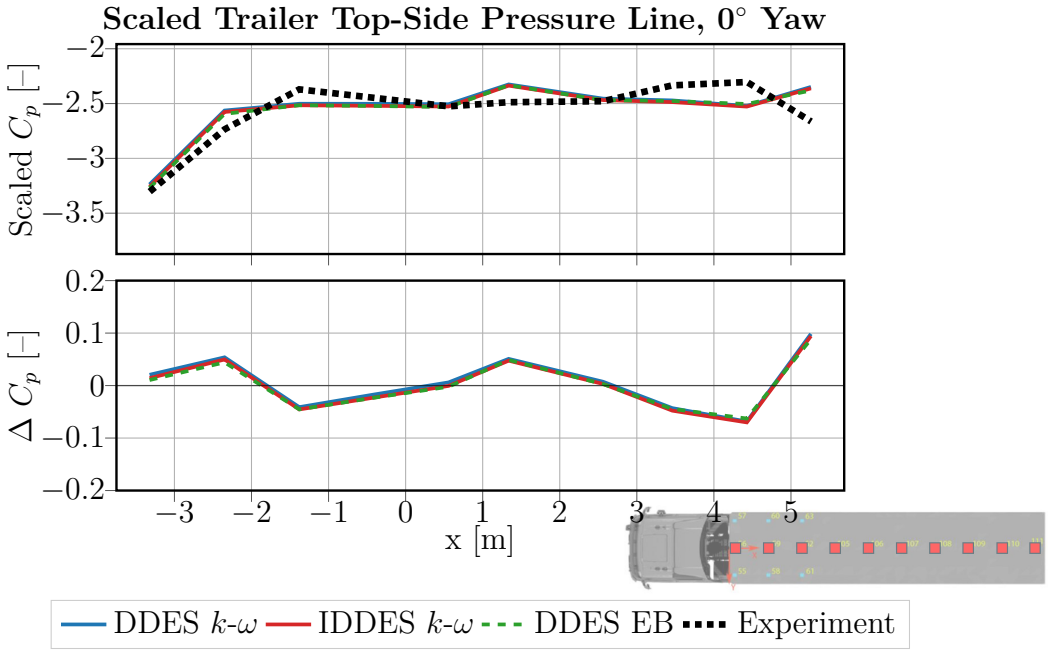

(a) 0° yaw

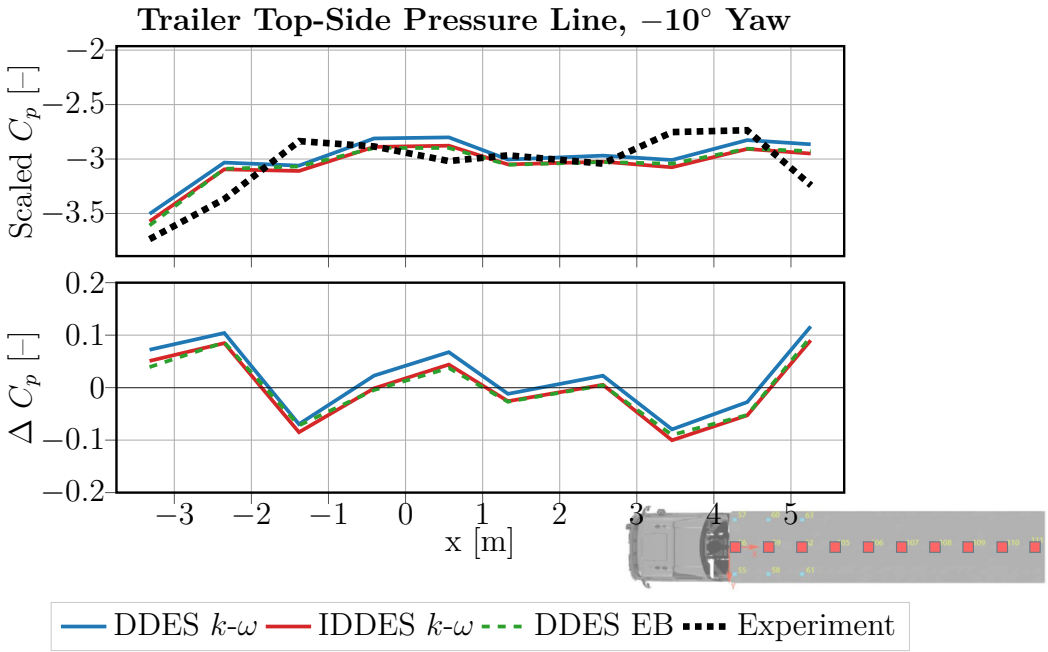

(b) −10° yaw

Figure 5.20: Trailer pressure distribution along the top pressure-tap line. Simulation results are compared to experimental measurements. The top shows the pressure coefficient, linearly rescaled to a unit range, and the bottom plot shows the absolute deviation from experiment.

The trailer rear pressure field reflects the flow development over the full vehicle and is therefore an important indicator of the resulting base-wake structure. At 0° yaw, DDES, shown in Figure 5.21a, slightly overpredicts the field-averaged pressure. Near the lower rear edge, the low-pressure region reaches a lower minimum pressure than in the experiment and shows a steeper gradient with a smaller vertical extent. A slight shift toward the right side is also present, although this is less pronounced in the experimental field. For IDDES, shown in Figure 5.21b, the field-averaged value is closer to the experiment, with a slight underprediction. The pressure gradient is less steep, and the low-pressure region extends further upward, giving better overall agreement with the measured field structure. Among the three models, DDES EB, shown in Figure 5.21c, provides the best overall agreement. A field-averaged value similar to IDDES is accompanied by a low-pressure region that extends to a height closer to the experimental result, and the overall pressure-field structure is reproduced more accurately than in the other simulations.

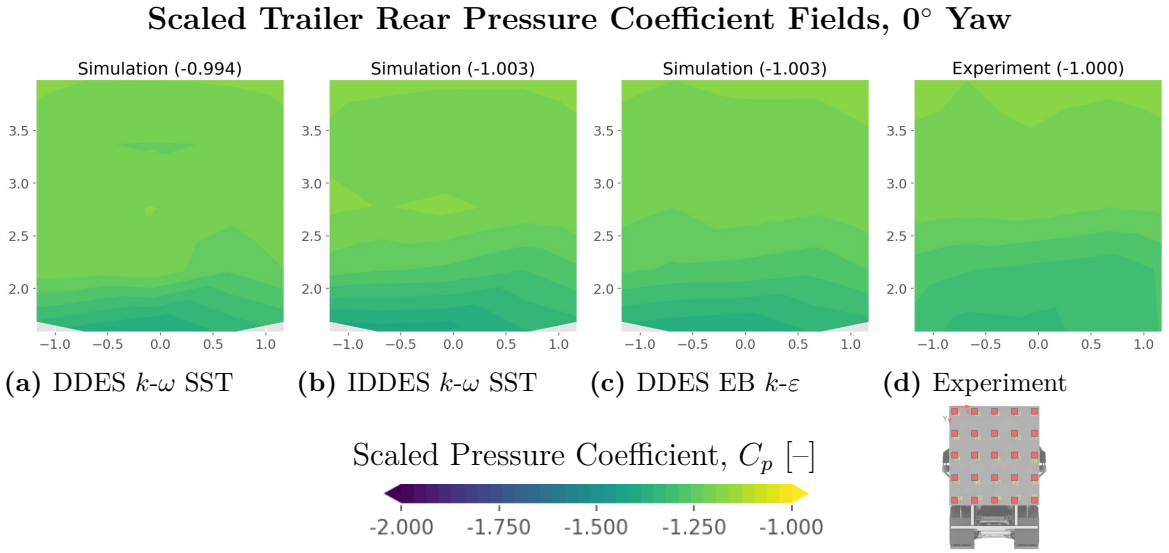

(a) DDES k-ω SST **(b)** IDDES k-ω SST **(c)** DDES EB k-ε **(d)** Experiment

Figure 5.21: Pressure coefficient fields, linearly rescaled to a unit range, from rear pressure-taps at 0°. Field averaged values normalized by experimental values shown above each field.

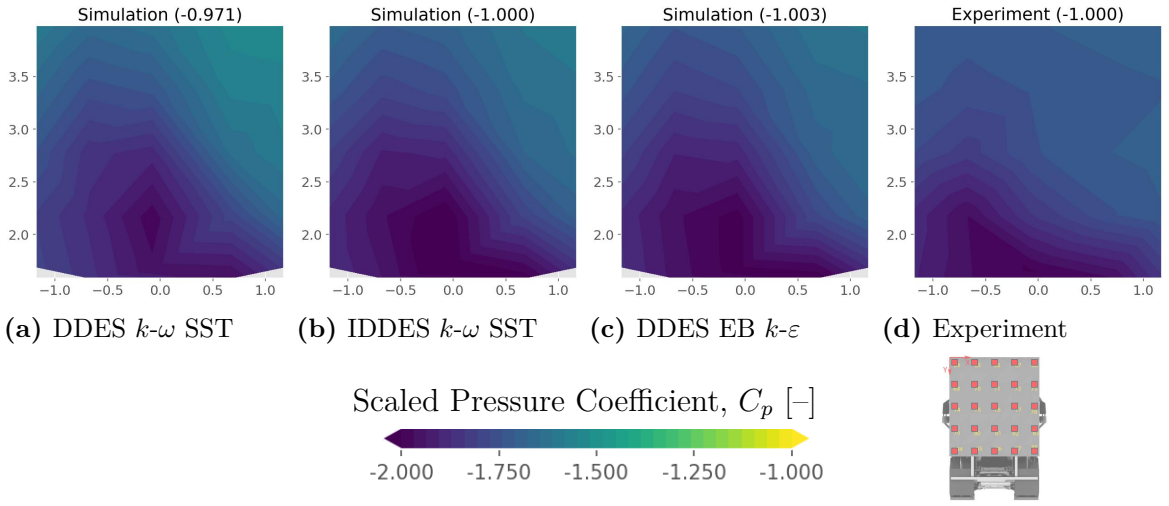

(a) DDES k-ω SST **(b)** IDDES k-ω SST **(c)** DDES EB k-ε **(d)** Experiment

Figure 5.22: Pressure coefficient fields, linearly rescaled to a unit range, from rear pressure-taps at −10°. Field averaged values normalized by experimental values shown above each field.

At $-10°$ yaw, the experimental trailer rear pressure field shows a low-pressure region in the lower-left corner that extends upward and toward the right. DDES, shown in Figure 5.22a, again overpredicts the field-average pressure, and its low-pressure region is more centered than in the experiment. IDDES, shown in Figure 5.22b, predicts the field-average pressure accurately and improves the spatial agreement relative to DDES, with the low-pressure region shifted further to the left and lower pressure in the upper-right corner. DDES EB, shown in Figure 5.22c, slightly underpredicts the field-average pressure and produces a pressure distribution that is very similar to that of IDDES, resulting in good overall agreement with the measurements. Since the trailer-base wake contributes strongly to the total drag, these results are particularly important and show that both IDDES k-ω and DDES EB capture the dominant rear-wake features well, whereas DDES k-ω is less accurate.

Overall, similar to the cab, the trailer pressure measurements distinguish the models only to a limited extent. For the field-average pressure levels, IDDES k-ω and DDES EB are generally closer to the measurements than DDES k-ω, although the differences depend on the left, right, and rear surfaces. The same trend is seen in the spatial pressure fields, where IDDES k-ω and DDES EB show the closest agreement, while DDES k-ω is slightly less consistent. Taken together, the trailer results suggest a modest advantage for IDDES k-ω and DDES EB, especially in the rear wake region that is most relevant for drag.

5.3 Yaw-sweep analysis

To further assess drag prediction, the study was extended to a full yaw sweep. Due to computational costs, only two models could be included: DDES EB, selected for its best overall balance between drag prediction and agreement with the experimental pressure fields, and DDES k-ω is retained as the reference model currently used in aerodynamic simulations at Volvo Group. The yaw sweep was performed across all four geometric truck configurations presented in section 5.1.1, covering five yaw angles and totaling 40 simulations. Table 5.3 presents the C_D errors in drag counts relative to the experimental values for all yaw angles, alongside the yaw-weighted average (YWA) C_D error defined in Equation (2.8). The YWA deviations from experiment with confidence intervals are shown in Figure 5.23.

Table 5.3: ΔC_D error relative to experiment in drag counts.

Turb. Model	Config	0.0°	−2.5°	−5.0°	−7.5°	−10.0°	YWA
DDES k-ω	1	−26	−21	−15	−9	0	−18
	2	−20	−22	−15	−5	−5	−17
	3	−26	−24	−18	−20	−26	−23
	4	−18	−20	−23	−19	−18	−20
DDES EB	1	−23	−18	−8	−2	0	−13
	2	−16	−15	−12	−8	−4	−13
	3	−17	−21	−21	−22	−23	−20
	4	−23	−13	−18	−14	−27	−17

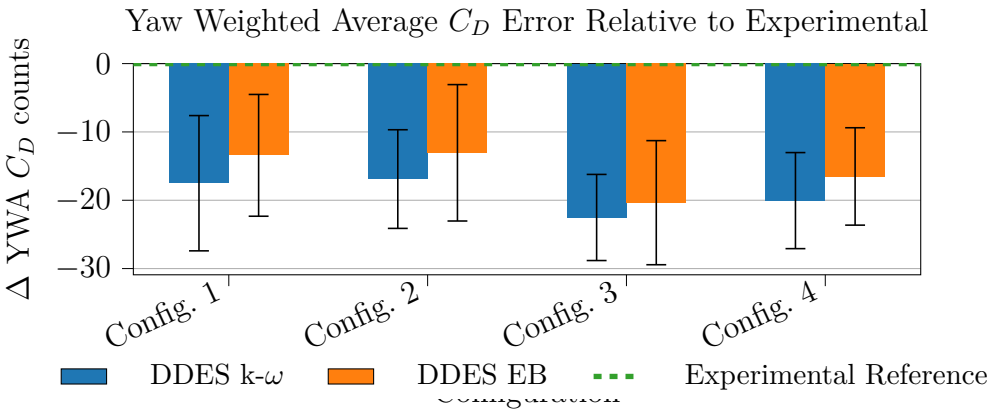

Figure 5.23: Difference in YWA C_D in drag counts relative to the experimental value for all configurations. Error bars display the yaw-weighted confidence interval.

The deviation in drag coefficient relative to the experimental values varies with truck configuration. For Configurations 1 and 2, shown in the upper part of Figure 5.24, the deviation generally decreases with increasing yaw angle, suggesting that both turbulence models capture the aerodynamic response more accurately at higher yaw angles. This trend is likely attributable to a reduced influence of asymmetric inlet flow conditions at larger yaw angles. Between the two cases, DDES EB is closer to the experimental values for most yaw angles, with the exceptions of $-10°$ for Configuration 1 and $-7.5°$ for Configuration 2. The lower YWA values obtained with DDES EB, 5 counts for Configuration 1 and 4 counts for Configuration 2, further support its stronger predictive performance, as seen in Figure 5.23. This trend is consistent with the findings for the simplified truck model in Chapter 4, where DDES EB also demonstrated the best overall agreement with experiments among the hybrid RANS-LES models.

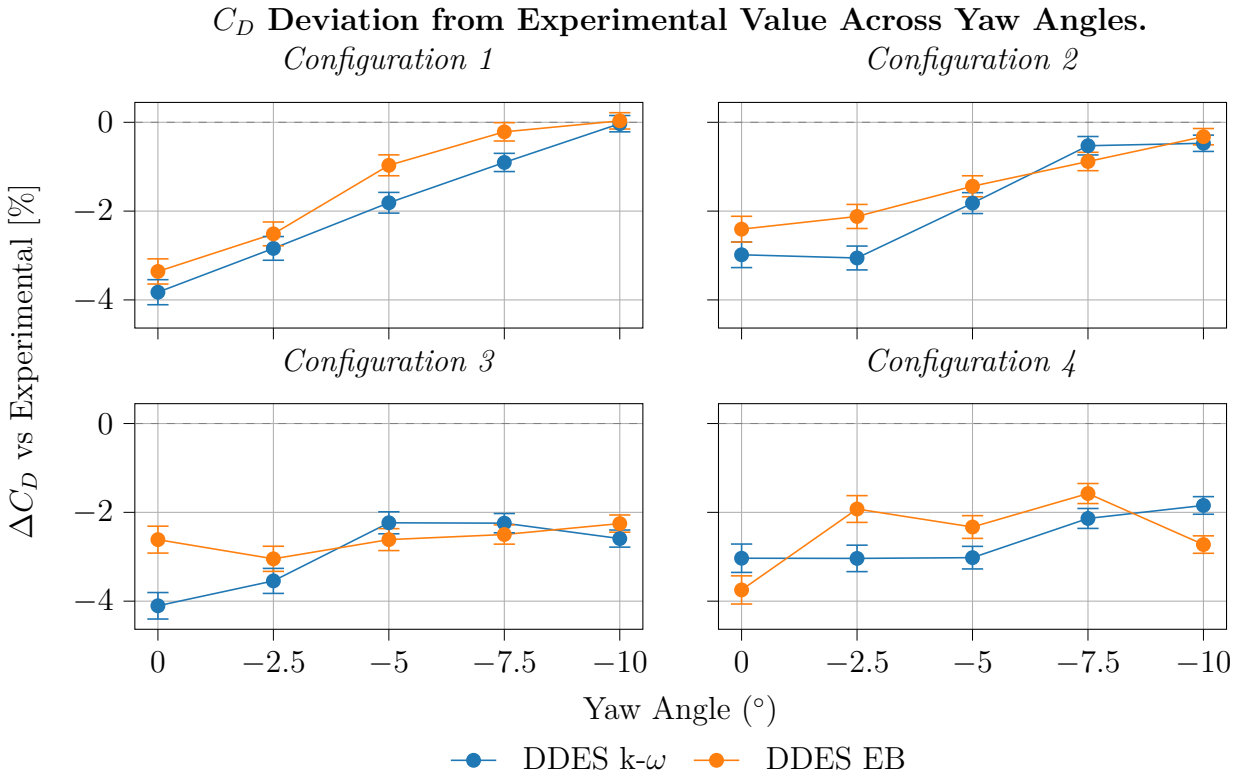

Figure 5.24: Comparison of the turbulence models across different yaw angles in percentages relative to experimental values. Error bars display the 95% confidence interval.

For Configurations 3 and 4, shown in the lower part of Figure 5.24, the deviations are distributed more uniformly across the yaw range. In these cases, the error appears less sensitive to yaw angle and more dependent on configuration-specific flow features. This suggests that persistent geometric effects have a stronger influence on the flow field than the yaw variation itself. Although DDES EB remains closer to the experimental values for several data points, its advantage is not systematic. The relative performance of DDES k-ω and DDES EB varies with yaw angle, indicating that neither model can be identified as consistently superior for these two configurations.

Uncertainty levels, represented by the confidence intervals in Figure 5.24, provide additional insight into model behavior. In some cases, DDES k-ω exhibits narrower confidence intervals than DDES EB, which may indicate lower solution variability or more stable convergence. A possible explanation is that the simulation setup was originally developed around DDES k-ω, which may favor its convergence behavior, though this cannot be confirmed from the present results alone. Other factors, such as highly disturbed flow conditions and the high wind-tunnel blockage ratio, may also contribute to both the error magnitude and the spread of the predictions. Despite a systematic underprediction in absolute drag, both models reproduce the overall yaw trend well, with drag increasing approximately linearly with yaw angle beyond $-2.5°$.

5.3.1 Prediction of Drag Changes Between Configurations

To assess the ability of the turbulence models to predict the aerodynamic impact of geometric modifications, the change in drag coefficient, C_D, between the different configurations is

examined. The comparison is based on the YWA value in order to reduce the influence of discrepancies between individual yaw angles. Model performance is evaluated using two types of comparisons. First, accumulated changes in C_D are evaluated relative to the baseline configuration, Configuration 1, through the comparisons 1–2, 1–3, and 1–4. Second, step-wise differences are considered, where Configuration 1 is compared with Configuration 2, Configuration 2 with Configuration 3, and Configuration 3 with Configuration 4.

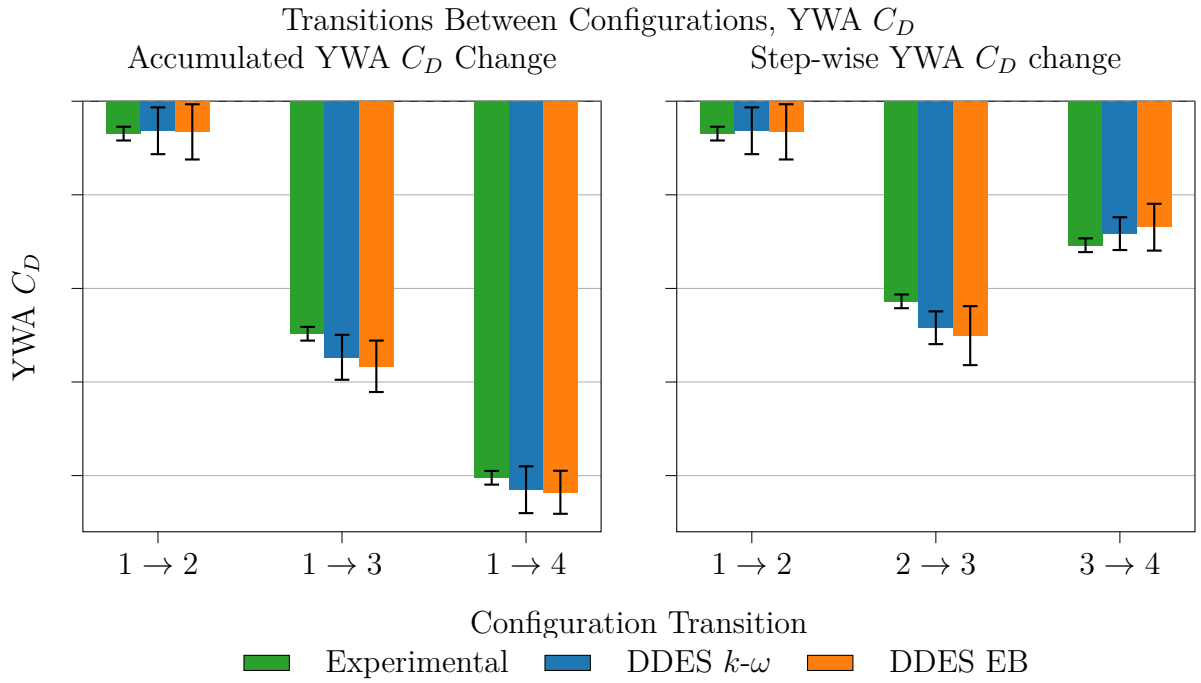

Figure 5.25: Yaw-weighted averaged relative difference in drag coefficient between configurations (accumulated and step-wise). Error bars show the weighted confidence interval; Y-axis values are omitted for confidentiality.

Figure 5.25 presents the predicted changes in drag coefficient between configurations, evaluated both as accumulated and consecutive (stepwise) differences. DDES k-ω generally predicts these drag differences more accurately than DDES EB, both for the stepwise and accumulated changes. Thus, while DDES EB provides improved agreement in terms of absolute drag levels, it shows larger deviations in the prediction of relative changes between configurations. This behavior may be attributed to a more consistent drag underprediction observed for DDES k-ω, which leads to more uniform differences between configurations and yaw angles. In contrast, DDES EB exhibits greater variability, with locally improved or degraded agreement, resulting in larger discrepancies in the predicted drag deltas.

It should also be noted that most of the observed differences are not statistically significant, since they fall within the estimated confidence intervals of the simulations. Consequently, no definitive conclusion can be drawn regarding the relative performance of the two models in predicting drag differences. Nevertheless, the lower accuracy of DDES EB in predicting relative drag changes weakens the case for it being a superior model overall.

5.4 Numerical Sensitivity Analysis

This section examines the sensitivity of the full-scale truck simulations to key numerical settings, including timestep size, number of inner iterations, and selected mesh effects. The aim is to assess how these parameters influence convergence and local flow predictions, and to clarify which observed differences are due to numerics rather than turbulence-model behavior.

5.4.1 Prism-Layer Sensitivity

To investigate the influence of increased prism-layer resolution and wall-distance coverage, a dedicated study was carried out using a recent full-scale truck model in an open-road simulation. Assessment of the boundary-layer velocity profile was carried out using probes placed in the near-wall region. This allowed sampling of the velocity at each cell center and documented the boundary-layer resolution. Measurements were recorded in regions where the flow was fully or partially attached. The boundary-layer thickness was defined as the wall-normal location at which the velocity reaches 99% of the near-freestream value, $v = 0.99\, v_{\mathrm{max,freestream}}$. To better resolve the steep near-wall gradients and improve boundary-layer resolution, prism layers were applied throughout the boundary layer.

An inherent constraint of the meshing approach is the prism-layer spacing as it follows a geometric progression. In practice, this means that when increasing the amount of prism layers the total height must also be slightly increased to retain a smooth transition between the prism layers and the trimmed volume. In regions with partially detached flow or very thick boundary layers, such as along the trailer, fully covering the boundary layer with prism cells is not feasible. In these areas, the focus is therefore placed on resolving the steep initial velocity gradient close to the wall.

The prism-layer study focuses on four main regions: the front corners of the cab, the A-pillars, the remainder of the cab, and the trailer. An initial simulation was performed using the DDES k-ω SST model with prism-layer settings given in Table 5.4. The last-layer thickness is reported to monitor the relationship between the original last-layer height and the volume mesh size. If the number of layers or the layer height is reduced below the values in Table 5.4, the transition quality generally becomes poorer.

Table 5.4: Prism-layer controls by surface region.

Region	Total Height	Number of Layers (-)	Last-Layer Thickness
Front corner	x	10	0.39x
Cab	y	10	0.44y
Trailer	z	10	0.44z
A-pillar	w	10	0.33w

The velocity profiles at the A-pillars are not presented due to confidentiality. Figure 5.26 shows the resolution in the front-corner region. In this area, most of the boundary layer is covered by the total prism-layer thickness. The main objective in this region is therefore to increase

the resolution while maintaining approximately the same total prism-layer height.

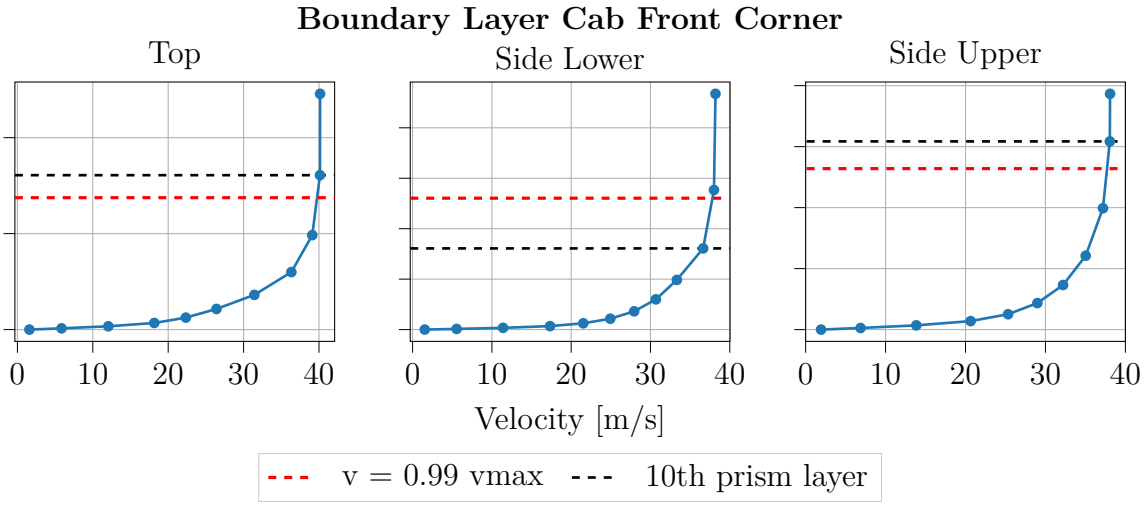

Figure 5.26: Near-wall velocity profiles in the front-corner region, plotted at cell-center positions as a function of wall distance. The red dashed line indicates the boundary-layer thickness, and the black dashed line shows the cell-center position of the outermost prism-layer cell.

Figure 5.27 shows the boundary layer in the cab region. Here, the boundary-layer thickness increases to approximately 50 mm, and the current prism-layer thickness is insufficient to cover the full layer. Increasing the prism-layer thickness to fully match the boundary-layer thickness would be computationally too expensive. However, given the relatively fine resolution already present outside the boundary layer, a modest increase in prism-layer height and layer count should improve the near-wall resolution.

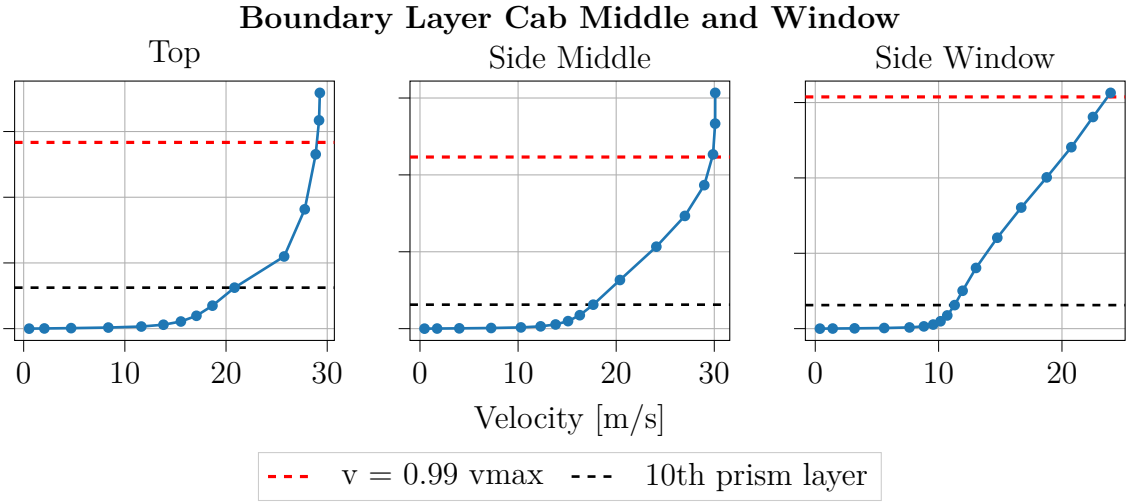

Figure 5.27: Near-wall velocity profiles in the cab region, plotted at cell-center positions as a function of wall distance. The red dashed line indicates the boundary-layer thickness, and the black dashed line shows the cell-center position of the outermost prism-layer cell.

The boundary layer on the trailer is thicker, as shown in Figure 5.28, where it exceeds 400 mm on the sides. Covering the entire thickness with prism layers is not feasible. Instead, a moderate

increase in prism-layer thickness can be applied to better capture the initial near-wall velocity gradient.

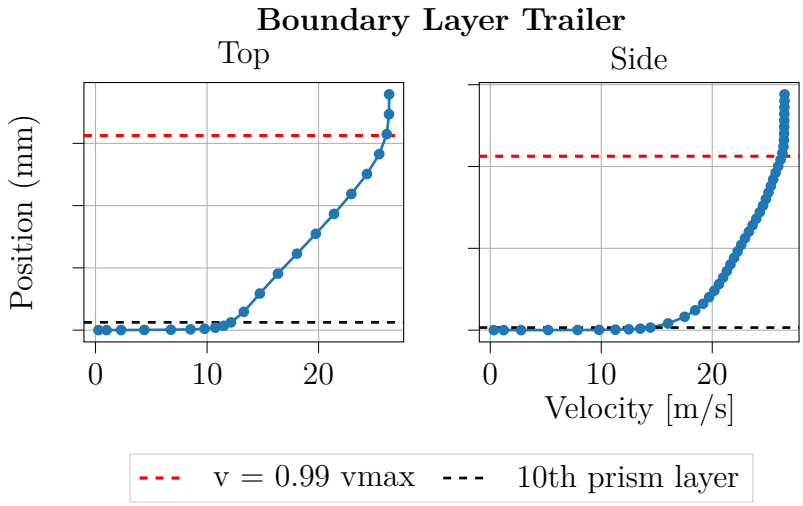

Figure 5.28: Near-wall velocity profiles in the trailer region, plotted at cell-center positions as a function of wall distance. The red dashed line indicates the boundary-layer thickness, and the black dashed line shows the cell-center position of the outermost prism-layer cell.

5.4.1.1 Results - Prism-Layer Sensitivity

The prism-layer settings and the corresponding last-layer height for each region is summarized in Table 5.5. Three prism-layer counts were considered: 10, 15, and 20 layers. The 10-layer case was used as the base mesh for comparison.

At the front corners, where increasing resolution was the main objective, the total prism-layer height was increased only enough to maintain approximately the same last-layer height. A similar approach, increasing the resolution while keeping the last-layer height nearly constant, was applied to the A-pillar. For the cab, where the objective was both to increase the resolution and to increase the prism-layer height the total height was doubled. For the trailer region, where the main objective was to increase the wall-distance coverage, the total height was increased first by 3 and then to 4 times the original height.

Table 5.5: Prism-layer controls by surface region and number of layers. Exact values omitted due to confidentiality.

Region	Relative Layer Heights	10 layers	15 layers	20 layers
Front corner	Total height	x	1.5x	2x
	Last-layer height	0.39x	0.41x	0.42x
Cab	Total height	y	2y	2y
	Last-layer height	0.44y	0.66y	0.49y
Trailer	Total height	z	3z	4z
	Last-layer height	0.44z	1.05z	1.10z
A-pillar	Total height	w	1.5w	2w
	Last-layer height	0.33w	0.34w	0.35w

Boundary-layer velocity profiles from the front-corner region are shown in Figure 5.29. At all three measurement locations, it is evident that increasing the resolution and prism-layer height has only a minor effect on the boundary-layer structure.

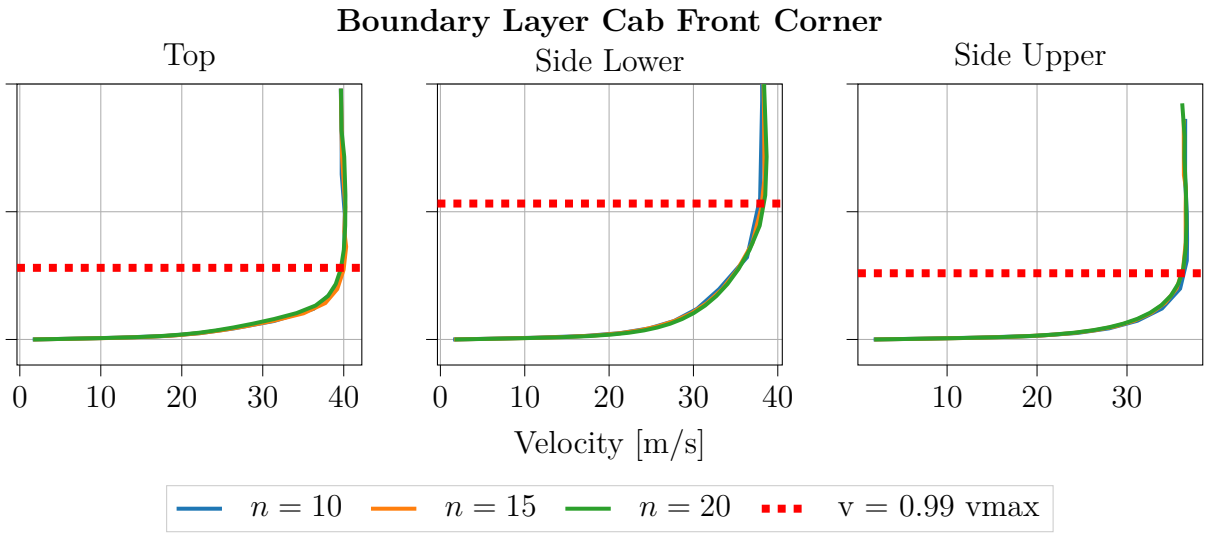

Figure 5.29: Near wall velocity profile in the front corner region for different prism-layer configurations. The number of prism layers is denoted by n.

The boundary-layer development on the cab in Figure 5.30 shows a sensitivity to prism-layer modifications similar to that observed at the front corners. At the top of the cab and on the side at mid-height, only minor changes are observed in the velocity profiles. However, at the side window the profile changes noticeably when the number of prism layers is increased to 20. Analysis of the flow fields, not shown here due to confidentiality, indicates that these differences originate from changes in the flow behavior around the A-pillar and the transition between the wiper panel and the A-pillar. These are regions of complex flow, and the results suggest that local refinement in these areas has the strongest influence on the flow.

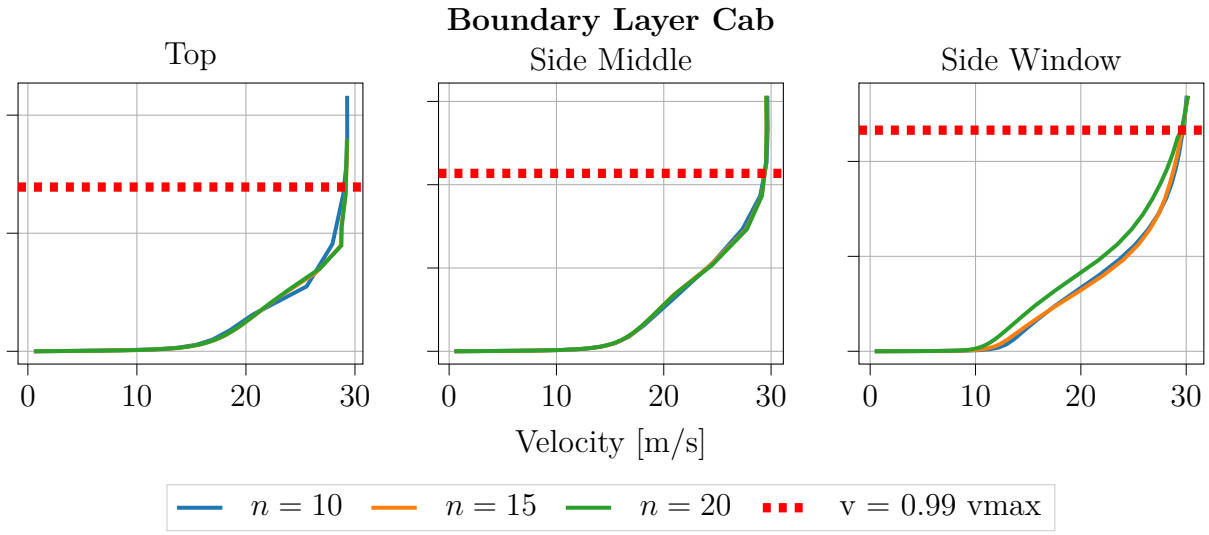

Figure 5.30: Near wall velocity profile in the cab region for different prism-layer configurations. The number of prism layers is denoted by n.

At the trailer, increasing the prism-layer height appears to influence the evolution of the velocity profile along the trailer side, as shown in Figure 5.31. However, this effect appears to be caused indirectly by changes in the upstream flow around the cab, particularly near the A-pillar, rather than by the prism-layer modification on the trailer itself.

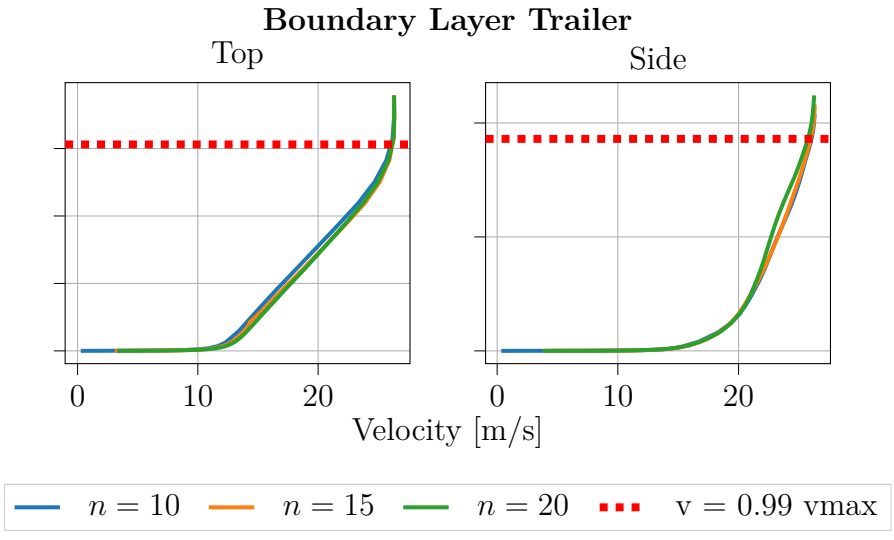

Figure 5.31: Near wall velocity profile in the trailer region for different prism layer configurations. The number of prism layers is denoted by n.

The difference in drag coefficient, C_D, relative to the base configuration with 10 prism layers is presented in Table 5.6 for yaw angles of 1° and −1°, together with their average. Simulations were performed using both the DDES k-ω and DDES EB turbulence models. For the DDES k-ω model, the drag coefficient increases at −1° and decreases at 1° yaw. Both the increase and decrease in yaw is associated with changed separation behavior in the A-pillar region.

The DDES EB model appears to be less sensitive to changes in prism-layer settings, as

reflected by the smaller changes in drag coefficient between the configurations. Although the yaw averaged drag decreases slightly from 10 to 15 layers, the separation pattern still indicates increased separation at the A-pillar. When increasing from 15 to 20 layers, the separation increases further, especially in the transition between the A-pillar and the wiper panel.

Table 5.6: ΔC_D in drag counts relative to the 10 prism layers baseline.

		Difference in Drag Counts		
Turbulence Model	**Prismlayers**	Yaw $-1°$	Yaw $1°$	Yaw average
DDES k-ω	10	—	—	—
	15	3.9	-1.4	1.3
	20	8.1	-1.0	3.6
DDES EB	10	—	—	—
	15	-2.0	1.0	-0.5
	20	1.8	1.8	1.8

5.4.2 Transient Solver Sensitivity

In order to reduce potential errors caused by inappropriate solver settings, the effects of time-stepping and the number of inner iterations were investigated. Improper time-stepping may result in excessive numerical diffusion or loss of temporal resolution, while too few inner iterations may lead to under-converged solutions within each time step. Both cases can result in non-physical behavior of the simulation.

5.4.2.1 Time-Stepping

The influence of time stepping was investigated for Configuration 1. Suitable time-step sizes were estimated based on an initial RANS simulation, in which the CFL number was evaluated for several candidate time steps. The preliminary assessment showed that halving the time step produced noticeable reductions in CFL number in some near-wall cells. Reducing the time step to one quarter of the original value led to a substantial decrease in CFL number in a majority of the cells near key regions like the mirrors and A-pillars. A further reduction by a factor of ten would likely eliminate any remaining time-step-related effects but such a choice was considered too computationally expensive.

For the investigation of time-stepping effects, the following turbulence models were evaluated using the finest feasible time step, corresponding to a reduction by a factor of four:

- DDES k-ω
- DDES EB
- WM LES

CFL Range	DDES k-ω (%)	DDES EB (%)	WM LES (%)
$0 \leq \text{CFL} < 1$	53.04	54.11	50.50
$1 \leq \text{CFL} < 5$	34.93	33.69	36.23
$5 \leq \text{CFL} < 20$	8.26	8.44	8.99
$\text{CFL} \geq 20$	3.77	3.76	4.27

Table 5.7: Cell count and percentage share by CFL bin for regular timestep ($\Delta t = \Delta t_0$).

CFL Range	DDES k-ω (%)	DDES EB (%)	WM LES (%)
$0 \leq \text{CFL} < 1$	85.88	85.78	84.66
$1 \leq \text{CFL} < 5$	10.44	10.50	11.03
$5 \leq \text{CFL} < 20$	3.33	3.36	3.86
$\text{CFL} \geq 20$	0.35	0.36	0.44

Table 5.8: Cell count and percentage share by CFL bin for reduced timestep ($\Delta t = \frac{\Delta t_0}{4}$).

Tables 5.8 and 5.7 show the fraction of cells within different CFL bins for the standard time step and for a time step that is one quarter of that size. Through comparing the two tables it is evident that reducing the timestep significantly decreases the proportion of cells experiencing high CFL numbers. In particular, the fraction of cells with $\text{CFL} \geq 1$ is substantially reduced, indicating a better temporal resolution and improved adherence to the CFL condition.

Lower CFL numbers are generally associated with improved numerical stability and potentially lower numerical dissipation. In the present study, the reduced time step leads to greater confidence in the time-averaged drag coefficient, indicating improved numerical stability. However, this increase in solution robustness does not correspond to a clear improvement in agreement with the experimental drag coefficient.

Figure 5.32 compares the drag-count deviation from experiments for the baseline timestep Δt_0 and the reduced timestep $\Delta t_0/4$. Overall, no systematic reduction in absolute error is observed when the time step is decreased. In most cases, the differences between the two settings remain within the confidence interval of the drag coefficient. For the DDES k-ω and DDES EB simulations, reducing the time step produces only minor changes in the time-averaged drag coefficient. In contrast, decreasing the time step in the WM LES does not reduce the deviation from the experimental drag. This suggests that altering the time step cannot compensate for the lack of near-wall refinement, and that spatial resolution remains the limiting factor.

Although some variation in drag-coefficient error is observed between cases, the results obtained with the two time steps remain comparable in magnitude. This indicates that, for the present setup, integral quantities such as drag are only weakly sensitive to the chosen time step. Since the baseline time step is consistent with Volvo standard practice for aerodynamic simulations, a coarser temporal resolution was not considered further, as it would be unlikely to improve accuracy. Conversely, the finer time step is not justified, given its fourfold increase in computational cost.

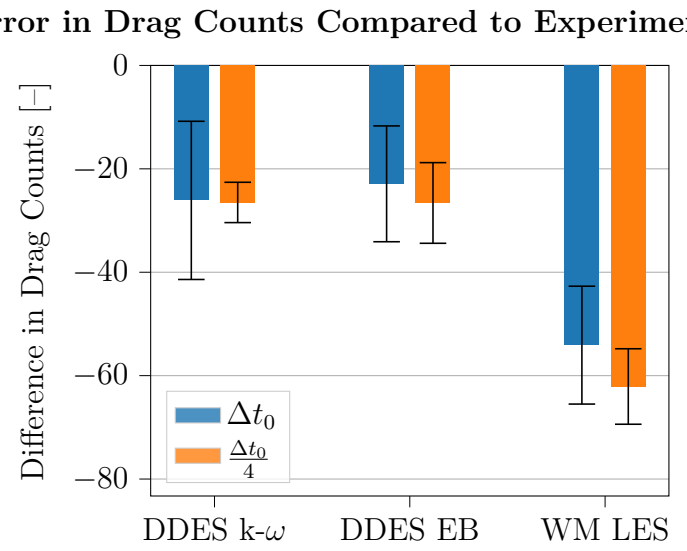

Figure 5.32: Error in drag counts compared to experimental data for the baseline timestep, Δt_0, and the reduced timestep, $\Delta t_0/4$.

5.4.2.2 Inner Iterations

The influence of the number of inner iterations was investigated by varying the number of iterations per time step from 3 to 20 for the DDES EB model. For each setting, 100 time steps were simulated to assess the effect on solver convergence under wind tunnel conditions for Configuration 1. The analysis provides an indication of how the number of inner iterations influences the convergence behavior within each timestep.

It should be noted that this analysis was performed exclusively for the DDES EB model. The simulation was not restarted for each case in the sweep; instead, the calculation was continued while the number of inner iterations was progressively increased. Consequently, the observed response may be influenced by transient development in the flow field, and the results should therefore be interpreted as representative trends rather than fully independent case comparisons.

The timestep sequences were selected based on exhibiting high variance in the monitored quantities, as these intervals are the most challenging to resolve and therefore most sensitive to the number of inner iterations. Only results corresponding to 20 inner iterations are presented, as they provide a reference for assessing the performance at lower iteration counts.

To examine the effect in more detail, the results are first presented for the trailer wake and subsequently for the mirror wake. In both regions, probe locations were selected to capture differences between near-wake and farther downstream flow conditions.

Figure 5.33: Schematic of the six pressure probe positions x_1–x_6 in the trailer wake relative to the trailer rear face, at distances 0.1 m, 0.8 m, 3.1 m, 4.6 m, 5.6 m, and 6.1 m, respectively. All probes are placed on the $y = 0$ plane, forming a straight line in the streamwise direction.

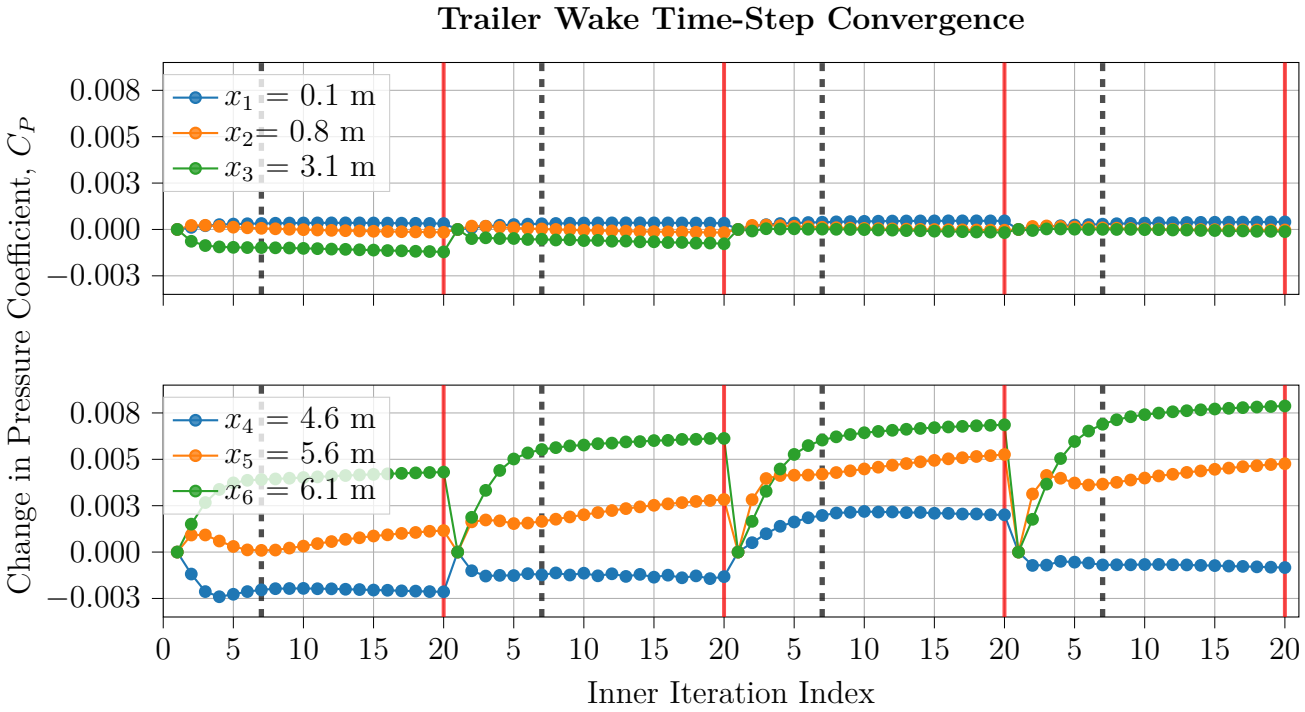

Figure 5.34: Change in pressure coefficient C_p over four timesteps of 20 inner iterations each in the trailer wake. The x-coordinates are relative to the trailer rear face. Probe positions as shown in Figure 5.33. The 7th iteration is marked by a vertical dashed line.

The probe locations in the trailer wake are shown in Figure 5.33. Points x_1–x_3 are located closest to the trailer, whereas points x_4–x_6 are positioned farther downstream. The corresponding results for the 20 inner-iteration timesteps are presented in Figure 5.34. In the trailer wake, the near-field probes x_1–x_3 exhibit smaller timestep-to-timestep variations and faster convergence than x_4–x_6. The initial steep change in pressure coefficient is largely captured within the first 6–8 iterations, indicating diminishing returns from additional iterations beyond this range.

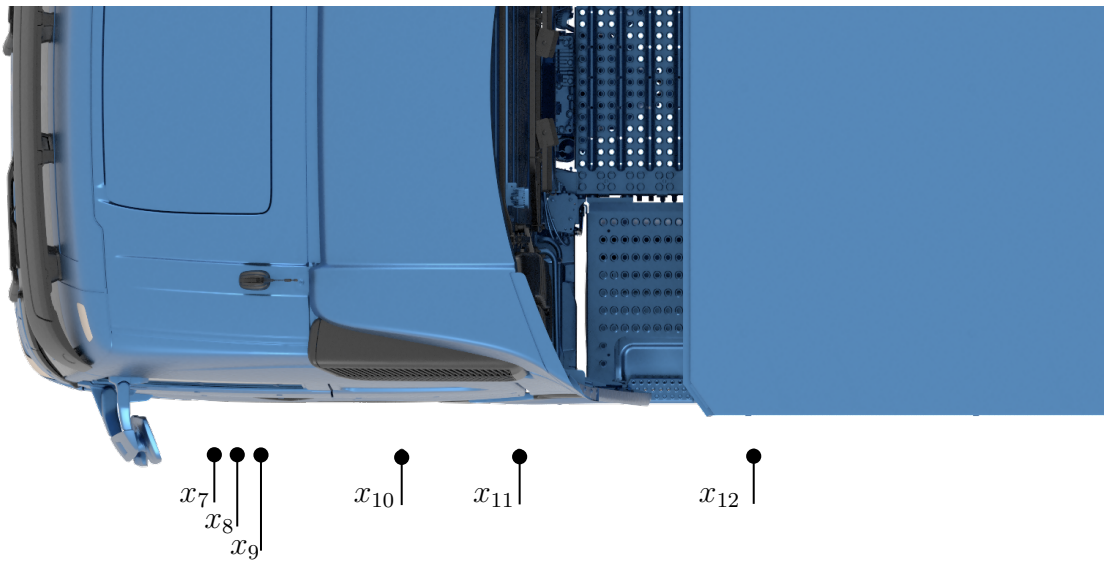

Figure 5.35: Schematic of the six pressure probe positions x_7–x_{12} in the mirror wake relative to the mirror reference plane, at distances 0.3 m, 0.4 m, 0.5 m, 1.1 m, 1.6 m, and 2.6 m, respectively. All probes lie on the same spanwise (z) coordinate, forming a straight line in the streamwise direction.

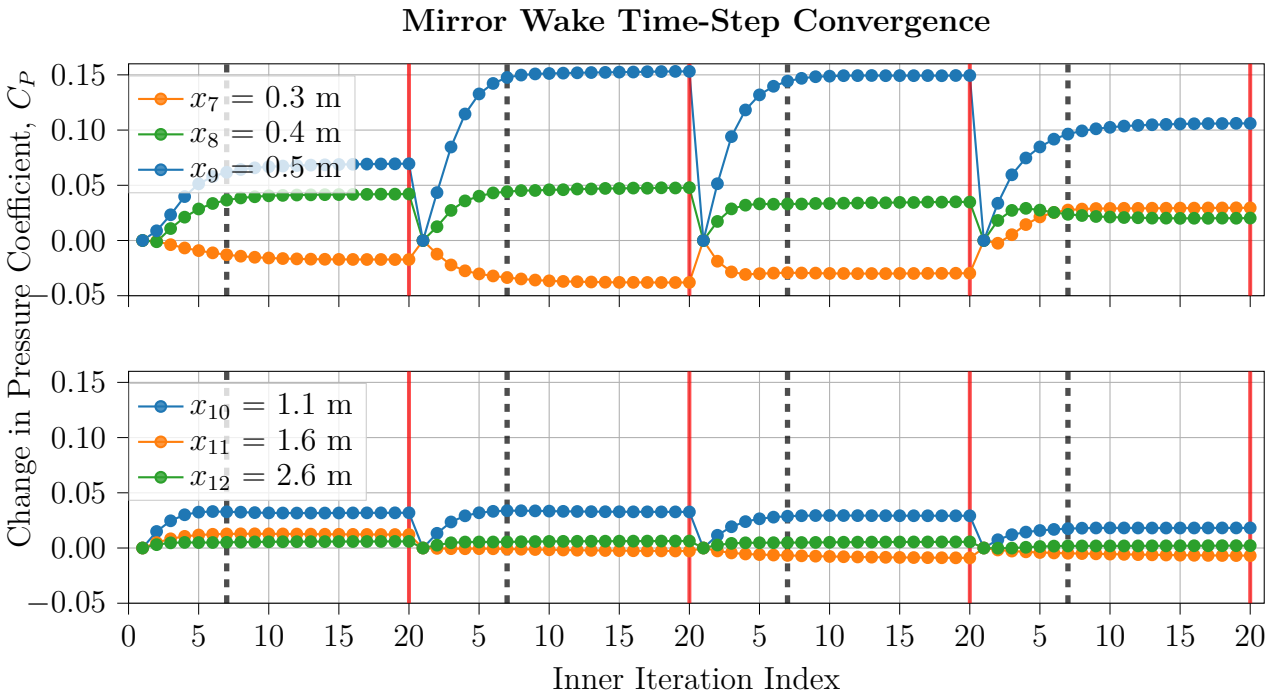

Figure 5.36: Change in pressure coefficient C_p over four timesteps of 20 inner iterations each in the mirror wake. The x-coordinates are relative to the mirror reference plane. Probe positions as shown in Figure 5.35. The 7th iteration is marked by a vertical dashed line.

The probe locations in the mirror wake are shown in Figure 5.35. As in the trailer wake, points x_7–x_9 represent the near-field region, while points x_10–x_12 are located farther downstream. The corresponding results for the 20 inner-iteration timesteps are shown in Figure 5.36. In contrast to the trailer wake, the probes closest to the mirror exhibit the largest fluctuations

and the slowest convergence. Here as well, 6–8 inner iterations appear sufficient to approach convergence, while downstream locations show smaller fluctuations and converge within approximately five iterations.

Overall, the trailer and mirror wakes exhibit distinct but consistent convergence characteristics. The trailer wake converges more rapidly in the near field, whereas the mirror wake shows the strongest sensitivity close to the mirror. In both regions, 6–8 inner iterations provide a reasonable balance between convergence quality and computational cost, with further increases yielding only marginal improvement. To visualize this the 7th iteration in each timestep is marked by a dashed line in Figures 5.36 and 5.34. The results should be interpreted as indicative trends rather than fully independent comparisons due to the continuous nature of the sweep.

5.5 Summary and Conclusion - Full-Scale Truck Simulations

Simulations of a full-scale truck under wind-tunnel conditions were used to evaluate the selected turbulence models. WM LES and SRH k-ω SST showed the weakest drag predictions at $0°$ and $-10°$ yaw and were therefore excluded from further consideration. Of the remaining models, DDES k-ω SST, IDDES k-ω SST, and DDES EB k-ε produced similar pressure distributions. However, DDES EB k-ε yielded the most accurate drag predictions along with good agreement with the trailer pressure field, and was therefore selected for the extended yaw sweep.

A yaw sweep covering four vehicle configurations and five yaw angles showed that both models reproduce the overall drag trend well. DDES EB k-ε matched the experimental absolute drag levels more closely for most yaw angles and obtained the lower YWA error for configurations 1 and 2, though the advantage was less clear for configurations 3 and 4. For ΔC_D, DDES k-ω predicted configuration-to-configuration changes slightly better, although the difference was small and mostly within the estimated uncertainty bounds. This indicates that the preferred model depends on whether the objective is accurate absolute drag prediction or reliable prediction of relative drag changes.

The numerical sensitivity studies showed that reducing the baseline time step to one-quarter of its original value had only minor effects on the solution, while 6–8 inner iterations were sufficient to approach the asymptotic timestep-converged solution. A prism-layer study showed that increasing prism-layer resolution had a minor effect on the boundary-layer structure in most regions, with the main influence localized to the A-pillar and the regions immediately downstream. Taken together, these results support the chosen numerical setup as a reasonable compromise between accuracy, robustness, and computational cost.

6

Conclusion

This thesis investigated the performance of different turbulence and near-wall modeling approaches for aerodynamic simulations of commercial vehicles, with emphasis on the balance between predictive accuracy and computational cost. More than 70 simulations were performed across the two geometries, requiring approximately 11 million CPU hours. This reflects both the scope of the study and the high computational demands associated with scale-resolving simulations of heavy-duty vehicle aerodynamics. The study addresses the need for reliable numerical methods that can support aerodynamic development in an industrial context, where improved drag prediction can reduce both emissions and operating costs. A systematic comparison was therefore carried out using a simplified truck geometry and a detailed production truck, including wall-resolved LES, wall-modeled LES, hybrid RANS–LES methods, and selected RANS formulations.

For the simplified Allan truck case a high-fidelity LES simulation was performed. The simulation predicted a drag coefficient in good agreement with the experimental data reported by [7] and reproduced similar pressure distributions and flow-field features. The LES simulation, together with the experimental data, served as a high-resolution reference for evaluating the hybrid RANS-LES models. Among the tested models, the DDES Elliptic Blending k-ε model and the wall-modeled LES performed best in both drag prediction and separation behavior.

The remaining hybrid models, including the DDES and IDDES k-ω SST models, the standard and Lag Elliptic Blending SRH models, and the SRH k-ω SST model, did not reproduce the separation behavior observed in the LES simulation. Instead, they predicted excessive separation at the cab leading edge. Adding the γ-Re_θ transition model to the k-ω SST models did not improve the results overall and in some cases increased separation. The exception was for the SRH k-ω SST model, which showed results closer to the standard DDES k-ω SST case at a lower computational cost.

An initial evaluation was then carried out for five of the most promising turbulence models on a full-scale production truck under wind-tunnel conditions. The predicted drag coefficients at 0° and -10° yaw were compared with the experimental data reported by [6]. The wall-modeled LES and SRH k-ω SST models deviated more from measured drag coefficients than other models. Both IDDES k-ω SST and DDES Elliptic Blending showed good agreement with the pressure measurements, indicating that they captured the main flow features well. IDDES k-ω SST appeared favorable in the field-averaged pressure comparison, particularly on the cab, whereas DDES Elliptic Blending performed better on the trailer and provided more accurate drag predictions. For this reason, DDES Elliptic Blending was selected for further comparison

of absolute drag performance. DDES k-ω SST was retained because it is the standard model used in aerodynamic simulations at Volvo.

Following this selection, a full asymmetric yaw sweep was performed from $0°$ to $-10°$ for four truck geometry configurations using the DDES k-ω SST and DDES Elliptic Blending k-ε models. In terms of absolute prediction, the DDES Elliptic Blending model agreed better with the experimental values for most individual yaw angles and for the yaw-weighted average. The DDES k-ω SST model, however, predicted the drag coefficient differences between the geometric configurations more accurately.

Sensitivity studies of time step and inner iterations indicated that the current Volvo simulation setup uses a sufficient number of inner iterations and provides acceptable temporal resolution. Convergence within each time step was close to its asymptotic level after 6 to 8 inner iterations, and reducing the time step by a factor of four lowered the simulation uncertainty but produced only minor changes in the drag coefficient. Variation of prism-layer height and cell density showed that most of the cab and trailer flow was unaffected, while the observed changes appear to originate mainly from the influence of the prism layers on the flow around the A-pillar. The DDES Elliptic Blending model was also less sensitive to these mesh variations than the DDES k-ω SST model.

Overall, the study did not identify a single turbulence-model setup that was clearly superior for all evaluation criteria. Instead, the results indicate that model suitability depends on the intended engineering objective. DDES Elliptic Blending was generally the most suitable choice when accurate absolute drag prediction was prioritized, whereas DDES k-ω SST showed somewhat better performance in predicting relative drag changes between geometry configurations. The numerical sensitivity studies further indicate that the current Volvo simulation setup provides a reasonable balance between predictive accuracy, robustness, and computational cost.

6.1 Future Work

To further investigate how the accuracy of aerodynamic simulations can be improved, several extensions of the present work can be considered. A key next step is a broader grid-convergence study for each turbulence model, with particular focus on DDES Elliptic Blending and DDES k-ω SST. This should include a more detailed analysis of how near-wall resolution influences separation behavior, the predicted flow field, and global drag coefficient. Particular attention should be given to the A-pillar region, where the prism-layer sensitivity study indicated that local mesh changes may influence the separation behavior and the downstream development of the flow over both the cab and trailer.

Although the IDDES k-ω SST simulations underpredicted drag and were therefore excluded from the main comparison, the model showed relatively consistent pressure-field results. Extending the yaw-sweep analysis to include this model could provide insight into whether this consistency leads to improved prediction of drag differences between geometry configurations, in a manner similar to DDES k-ω SST, which showed greater consistency than DDES Elliptic Blending k-ε, despite the latter exhibiting higher absolute accuracy.

Another important direction is to assess additional turbulence model formulations, particularly models with improved shielding behavior or a more robust transition between RANS and

LES regions. Some of these models are not available in the present STAR-CCM+ setup, and investigating them outside this environment would be interesting, although this would be more difficult since the current workflow is built around STAR-CCM+ and the associated Volvo simulation procedures. Since the results showed that model ranking depends on the flow quantity being evaluated, future studies should also consider a broader set of validation metrics, including more detailed wake measurements, additional surface-pressure data, and velocity-field measurements in selected regions of interest.

More comparisons between DDES EB and DDES k-ω under open-road conditions would also be valuable, both to reduce the influence of wind-tunnel wall effects and to better replicate production-like simulation conditions. In the same context, it would be worthwhile to tune the wind-tunnel setup for DDES EB in order to enable a fairer comparison between the two models. A symmetric yaw sweep would likewise provide a broader basis for assessing model performance and help determine whether the observed trends remain consistent for both positive and negative yaw angles.

The methodology developed in this thesis could also be extended to other vehicle geometries and operating conditions, including different trailer configurations, additional yaw angles, and other aerodynamic devices. Such studies would help determine how general the present conclusions are and support the development of more robust CFD best practices for aerodynamic optimization of commercial vehicles in an industrial context.

References

[1] *Lorries, buses and coaches - Climate Action - European Commission*. [Online]. Available: https://climate.ec.europa.eu/eu-action/transport-decarbonisation/road-transport/lorries-buses-and-coaches_en.

[2] T. Schuetz, *Aerodynamics of road vehicles*. Society of Automotive Engineers, 2016, ISBN: 9780768082531.

[3] K. Varma, "The business case for autonomous deliveries : does it exist ? : an economic assessment of the use of autonomous vehicle technology for last mile deliveries," Ph.D. dissertation, Université Gustave Eiffel, Paris, 2022. [Online]. Available: https://theses.hal.science/tel-03853065v1.

[4] N. Ashton, A. West, S. Lardeau, and A. Revell, "Assessment of RANS and DES methods for realistic automotive models," *Computers and Fluids*, vol. 128, pp. 1–15, Apr. 2016, ISSN: 00457930. DOI: 10.1016/j.compfluid.2016.01.008.

[5] P. Ekman, *Important Factors for Accurate Scale-Resolving Simulations of Automotive Aerodynamics*. Linköping University Electronic Press, 2020, ISBN: 9789179298630.

[6] A. Niklasson, "Detailed analysis of the 2021 NRC wind tunnel flow survey and its implications on the external aerodynamics simulations methodology. ER-683384," Volvo Group, Gothenburg, Tech. Rep., 2022.

[7] J. W. Allan, "Aerodynamic drag and pressure measurements on a simplified tractor-trailer model," *Journal of Wind Engineering and Industrial Aerodynamics*, vol. 9, no. 1-2, pp. 125–136, Nov. 1981, ISSN: 0167-6105. DOI: 10.1016/0167-6105(81)90083-0. [Online]. Available: https://www.sciencedirect.com/science/article/pii/0167610581900830.

[8] H. Martini, B. Bergqvist, L. Hjelm, and L. Löfdahl, "Aerodynamic Effects of Roof Deflector and Cab Side Extenders for Truck-Trailer Combinations," *SAE Technical Papers*, Sep. 2011, ISSN: 0148-7191. DOI: 10.4271/2011-01-2284. [Online]. Available: https://saemobilus.sae.org/papers/aerodynamic-effects-roof-deflector-cab-side-extenders-truck-trailer-combinations-2011-01-2284.

[9] R. Wood, "Reynolds Number Impact on Commercial Vehicle Aerodynamics and Performance," *SAE International Journal of Commercial Vehicles*, vol. 8, pp. 590–667, Jan. 2015. DOI: 10.4271/2015-01-2859.

[10] *Pressure Drag - an overview | ScienceDirect Topics*. [Online]. Available: https://www.sciencedirect.com/topics/engineering/pressure-drag.

[11] H. Heisler, "Vehicle body aerodynamics," *Advanced Vehicle Technology*, pp. 584–634, 2002. DOI: 10.1016/b978-075065131-8/50015-4.

[12] C. Mockett, T. Knacke, and F. Thiele, "Detection of initial transient and estimation of statistical error in time-resolved turbulent flow data," in *Proceedings of the 8th International Symposium on Engineering Turbulence Modelling and Measurements*

(ETMM8), Marseille, France: European Research Collaboration on Flow Turbulence and Combustion (ERCOFTAC), Jun. 2010, pp. 9–11.

[13] R. Nichols, *Turbulence Models and Their Application to Complex Flows*. Jan. 2010.

[14] L. Davidson, *Fluid mechanics, turbulent flow and turbulence modeling*. 2025.

[15] A. J. Banko and D. J. K. Eaton, "A frame-invariant definition of the Q-criterion," 2019.

[16] K. A. Kovács and E. Balla, "Quantitative comparison of vortex identification methods in three-dimensional fluid flow around bluff bodies," *International Journal of Heat and Fluid Flow*, vol. 113, p. 109 773, Jun. 2025, ISSN: 0142-727X. DOI: 10.1016/J.IJHEATFLUIDFLOW.2025.109773. [Online]. Available: https://www.sciencedirect.com/science/article/pii/S0142727X25000311#sec5.

[17] H. K. Versteeg and W. Malalasekera, *An Introduction to Computational Fluid Dynamics: The Finite Volume Method*, 2nd. Pearson Education, 2007, ISBN: 0-582-21884-5.

[18] Siemens Digital Industries Software, *Simcenter STAR-CCM+ documentation*, 2025. [Online]. Available: https://docs.sw.siemens.com/documentation/external/PL20200805113346338/en-US/userManual/userguide/html/index.html#page/connect%2Fsplash.html.

[19] F. R. Menter, "Two-equation eddy-viscosity turbulence models for engineering applications," *AIAA Journal*, vol. 32, no. 8, pp. 1598–1605, 1994. DOI: 10.2514/3.12149.

[20] F. R. Menter, R. B. Langtry, S. R. Likki, Y. B. Suzen, P. G. Huang, and S. Völker, "A correlation-based transition model using local variables - Part I: Model formulation," *Journal of Turbomachinery*, vol. 128, no. 3, pp. 413–422, 2006, ISSN: 0889504X. DOI: 10.1115/1.2184352.

[21] U. Piomelli and E. Balaras, "Wall-Layer Models for Large-Eddy Simulations," *Annual Review of Fluid Mechanics*, vol. 34, pp. 349–374, 2002.

[22] P. R. Spalart, W. H. Jou, M. Strelets, and S. R. Allmaras, "Comments on the Feasibility of LES for Wings, and on a Hybrid RANS/LES Approach," in *Advances in DNS/LES*, C. Liu and Z. Liu, Eds., Columbus, OH: Greyden Press, 1997.

[23] F. R. Menter and M. Kuntz, "Adaptation of Eddy-Viscosity Turbulence Models to Unsteady Separated Flows Behind Vehicles," in *The Aerodynamics of Heavy Vehicles: Trucks, Buses, and Trains*, ser. Lecture Notes in Applied and Computational Mechanics, R. McCallen, F. Browand, and J. Ross, Eds., vol. 19, Springer Verlag, 2004, pp. 339–352.

[24] M. L. Shur, P. R. Spalart, M. K. Strelets, and A. K. Travin, "A hybrid RANS-LES approach with delayed-DES and wall-modelled LES capabilities," *International Journal of Heat and Fluid Flow*, vol. 29, no. 6, pp. 1638–1649, Dec. 2008, ISSN: 0142727X. DOI: 10.1016/j.ijheatfluidflow.2008.07.001.

[25] V. Duffal, B. De Laage De Meux, R. Manceau, · . Beno ̂ıt, B. De Laage De Meux, and R. Manceau, "Development and Validation of a new formulation of Hybrid Temporal Large Eddy Simulation," *Turbulence and Combustion*, vol. 108, p. 42, 2022. DOI: 10.1007/s10494-021-00264-z{\"{i}}. [Online]. Available: https://inria.hal.science/hal-03206747v1.

[26] H. Reichardt, "Vollständige Darstellung der turbulenten Geschwindigkeitsverteilung in glatten Leitungen," *Zeitschrift für Angewandte Mathematik und Mechanik*, vol. 31, no. 7, pp. 208–219, 1951.

[27] E. Ljungskog, S. Sebben, and A. Broniewicz, "Inclusion of the physical wind tunnel in vehicle CFD simulations for improved prediction quality," *Journal of Wind Engineering and Industrial Aerodynamics*, vol. 197, p. 104 055, Feb. 2020, ISSN: 0167-6105. DOI: 10.1016/J.JWEIA.2019.104055. [Online]. Available: https://www.sciencedirect.com/science/article/pii/S0167610519306555#bib18.

[28] A. Altinisik, E. Kutukceken, and H. Umur, "Experimental and numerical aerodynamic analysis of a passenger car: Influence of the blockage ratio on drag coefficient," *Journal of Fluids Engineering, Transactions of the ASME*, vol. 137, no. 8, Aug. 2015, ISSN: 1528901X. DOI: 10.1115/1.4030183/374123. [Online]. Available: https://dx.doi.org/10.1115/1.4030183.

[29] S. R. Ahmed, G. Ramm, and G. Faltin, "Some Salient Features of the Time-Averaged Ground Vehicle Wake," Tech. Rep., 1984, pp. 473–503. [Online]. Available: https://about.jstor.org/terms.

[30] S. Krajnović and L. Davidson, "Flow around a simplified car, part 1: Large eddy simulation," in *Journal of Fluids Engineering, Transactions of the ASME*, vol. 127, Sep. 2005, pp. 907–918. DOI: 10.1115/1.1989371.

[31] H. Lienhart and S. Becker, "Flow and Turbulence Structure In the Wake of a Simplified Car Model," Tech. Rep., 2003, pp. 785–796. [Online]. Available: https://about.jstor.org/terms.

[32] F. R. Menter, A. Hüppe, D. Flad, A. V. Garbaruk, A. A. Matyushenko, and A. S. Stabnikov, "Large Eddy Simulations for the Ahmed Car at 25° Slant Angle at Different Reynolds Numbers," *Flow, Turbulence and Combustion*, vol. 112, no. 1, pp. 321–343, Jan. 2024, ISSN: 15731987. DOI: 10.1007/s10494-023-00472-9.

[33] S. Krajnović, "What can LES do in vehicle aerodynamics?" *Lecture Notes in Applied and Computational Mechanics*, vol. 79, pp. 311–326, 2016, ISSN: 16137736. DOI: 10.1007/978-3-319-20122-1_20. [Online]. Available: https://link.springer.com/chapter/10.1007/978-3-319-20122-1_20.

[34] U. Piomelli and J. R. Chasnov, "Large-Eddy Simulations: Theory and Applications," pp. 269–336, 1996. DOI: 10.1007/978-94-015-8666-5_7. [Online]. Available: https://link.springer.com/chapter/10.1007/978-94-015-8666-5_7.

[35] D. K. Kolmogorov, F. R. Menter, and A. V. Garbaruk, "On mesh requirements for Large Eddy Simulation with Wall Functions," in *Journal of Physics: Conference Series*, vol. 2103, IOP Publishing Ltd, Dec. 2021. DOI: 10.1088/1742-6596/2103/1/012212.

[36] D. K. Kolmogorov, A. Hüppe, F. R. Menter, and A. V. Garbaruk, "Large Eddy Simulation with wall functions of Ahmed body," in *Journal of Physics: Conference Series*, vol. 2103, IOP Publishing Ltd, Dec. 2021. DOI: 10.1088/1742-6596/2103/1/012213.

[37] E. Guilmineau, G. B. Deng, A. Leroyer, P. Queutey, M. Visonneau, and J. Wackers, "Assessment of hybrid RANS-LES formulations for flow simulation around the Ahmed body," *Computers and Fluids*, vol. 176, pp. 302–319, Nov. 2018, ISSN: 00457930. DOI: 10.1016/j.compfluid.2017.01.005.

[38] N. Ashton and A. Revell, "Key factors in the use of DDES for the flow around a simplified car," *International Journal of Heat and Fluid Flow*, vol. 54, pp. 236–249, 2015, ISSN: 0142727X. DOI: 10.1016/j.ijheatfluidflow.2015.06.002.

[39] A. I. Heft, T. Indinger, and N. A. Adams, "Introduction of a New Realistic Generic Car Model for Aerodynamic Investigations," *SAE Technical Papers*, Apr. 2012, ISSN: 26883627. DOI: 10.4271/2012-01-0168. [Online]. Available: https://saemobilus.sae.org/papers/introduction-a-new-realistic-generic-car-model-aerodynamic-investigations-2012-01-0168.

[40] F. R. Menter, "Stress-blended eddy simulation (SBES)—A new paradigm in hybrid RANS-LES modeling," *Notes on Numerical Fluid Mechanics and Multidisciplinary Design*, vol. 137, pp. 27–37, 2018, ISSN: 16122909. DOI: 10.1007/978-3-319-70031-1_3. [Online]. Available: https://link.springer.com/chapter/10.1007/978-3-319-70031-1_3.

[41] J. Östh and S. Krajnović, "The flow around a simplified tractor-trailer model studied by large eddy simulation," *Journal of Wind Engineering and Industrial Aerodynamics*, vol. 102, pp. 36–47, 2012, ISSN: 01676105. DOI: 10.1016/j.jweia.2011.12.007.

[42] E. Josefsson, "Examination of robustness and accuracy of CFD simulations for external aerodynamics of commercial vehicles," Tech. Rep.

[43] J. Hodara and M. J. Smith, "Hybrid reynolds-averaged navier-stokes/large-eddy simulation closure for separated transitional flows," *AIAA Journal*, vol. 55, no. 6, pp. 1948–1958, 2017, ISSN: 00011452. DOI: 10.2514/1.J055475.

[44] M. D. Mays, S. Laizet, and S. Lardeau, "Performance of Various Turbulence Models for Simulating Sub-critical High-Reynolds Number Flows over a Smooth Cylinder," in *AIAA Aviation and Aeronautics Forum and Exposition, AIAA AVIATION Forum 2021*, American Institute of Aeronautics and Astronautics Inc, AIAA, 2021, ISBN: 9781624106101. DOI: 10.2514/6.2021-2762.

[45] G. Chen et al., "Aerodynamic performance and flow dynamics of High-Speed train under crosswind: Effect of turbulence model," *Physics of Fluids*, vol. 37, no. 11, Nov. 2025, ISSN: 10897666. DOI: 10.1063/5.0291907.

[46] R. Courant, K. Friedrichs, and H. Lewy, "On the Partial Difference Equations of Mathematical Physics," Institute of Mathematical Sciences, New York University, New York, New York, Tech. Rep., 1956.

[47] P. Ekman, T. Larsson, T. Virdung, and M. Karlsson, "Accuracy and speed for scale-resolving simulations of the DrivAer reference model," in *SAE Technical Papers*, vol. 2019-April, SAE International, Apr. 2019. DOI: 10.4271/2019-01-0639.

[48] M. Aultman, Z. Wang, and L. Duan, "Effect of time-step size on flow around generic car models," *Journal of Wind Engineering and Industrial Aerodynamics*, vol. 219, Dec. 2021, ISSN: 01676105. DOI: 10.1016/j.jweia.2021.104764.

[49] P. Ekman, R. Gårdhagen, T. Virdung, and M. Karlsson, "Aerodynamic Drag Reduction - from Conceptual Design on a Simplified Generic Model to Full-Scale Road Tests," *SAE Technical Papers*, vol. 2015-April, no. April, Apr. 2015, ISSN: 0148-7191. DOI: 10.4271/2015-01-1543. [Online]. Available: https://saemobilus.sae.org/papers/aerodynamic-drag-reduction-conceptual-design-a-simplified-generic-model-full-scale-road-tests-2015-01-1543.

[50] K. P. Garry, K. R. Cooper, A. Fediw, S. B. Wallis, and D. J. Wilsden, "The Effect on Aerodynamic Drag of the Longitudinal Position of a Road Vehicle Model in a Wind Tunnel Test Section," *SAE Technical Papers*, Mar. 1994, ISSN: 26883627. DOI: 10.4271/940414. [Online]. Available: https://saemobilus.sae.org/papers/effect-aerodynamic-drag-longitudinal-position-a-road-vehicle-model-a-wind-tunnel-test-section-940414.

[51] S. Johansson, "Improving Accuracy and Efficiency of Aerodynamic Simulations for Heavy Vehicles," Tech. Rep.

DEPARTMENT OF MECHANICS AND MARITIME SCIENCES
CHALMERS UNIVERSITY OF TECHNOLOGY
Gothenburg, Sweden 2026
www.chalmers.se

CHALMERS
UNIVERSITY OF TECHNOLOGY